



## **University of Bradford eThesis**

This thesis is hosted in [Bradford Scholars](#) – The University of Bradford Open Access repository. Visit the repository for full metadata or to contact the repository team



© University of Bradford. This work is licenced for reuse under a [Creative Commons Licence](#).

**NOVEL MEDICAL IMAGING TECHNOLOGIES  
FOR PROCESSING EPITHELIUM AND  
ENDOTHELIUM LAYERS IN CORNEAL  
CONFOCAL IMAGES**

**Developing Automated Segmentation and Quantification Algorithms  
for Processing Sub-basal Epithelium Nerves and Endothelial Cells for  
Early Diagnosis of Diabetic Neuropathy in Corneal Confocal  
Microscope Images**

***Shumoos Taha Hammadi HAMMADI***

**Submitted for the Degree of Doctor of Philosophy from the  
University of Bradford**

**School of Electrical Engineering and Computer  
Science**

**University of Bradford**

**© 2018**

# ABSTRACT

*Shumoos Taha Hammadi HAMMADI*

*Novel Medical Imaging Technologies for Processing Epithelium and Endothelium Layers in Corneal Confocal Images*

Developing Automated Segmentation and Quantification Algorithms for Processing Sub-basal Epithelium Nerves and Endothelial Cells for Early Diagnosis of Diabetic Neuropathy in Corneal Confocal Microscope Images

**Keywords:** Medical Imaging, Diabetic Peripheral Neuropathy, Corneal Confocal Microscopy, Corneal Sub-Basal Epithelium, Automatic Nerve Segmentation, Anisotropic Diffusion Filtering, Corneal Endothelial Cells, Automatic Cell Segmentation, Fast Fourier Transform, Watershed Transformation

Diabetic Peripheral Neuropathy (DPN) is one of the most common types of diabetes that can affect the cornea. An accurate analysis of the corneal epithelium nerve structures and the corneal endothelial cell can assist early diagnosis of this disease and other corneal diseases, which can lead to visual impairment and then to blindness. In this thesis, fully-automated segmentation and quantification algorithms for processing and analysing sub-basal epithelium nerves and endothelial cells are proposed for early diagnosis of diabetic neuropathy in Corneal Confocal Microscopy (CCM) images. Firstly, a fully automatic nerve segmentation system for corneal confocal microscope images is proposed. The performance of the proposed system is evaluated against manually traced images with an execution time of the prototype is 13 seconds. Secondly, an automatic corneal nerve registration system is proposed. The main aim of this system is to produce a new informative corneal image that contains structural and functional information. Thirdly, an automated real-time system, termed the Corneal Endothelium Analysis System (CEAS) is developed and applied for the segmentation of endothelial cells in images of human cornea obtained by In Vivo CCM. The performance of the proposed CEAS system was tested against manually traced images with an execution time of only 6 seconds per image.

Finally, the results obtained from all the proposed approaches have been evaluated and validated by an expert advisory board from two institutes, they are the Division of Medicine, Weill Cornell Medicine-Qatar, Doha, Qatar and the Manchester Royal Eye Hospital, Centre for Endocrinology and Diabetes, UK.

# Acknowledgements

Firstly, all praises to Allah, the most gracious and the most merciful, for the strengths, good health and blessing he gave me in completing this thesis.

I have probably met more interesting people that I have in my entire life before that. It is impossible to thank everyone in particular, as another dissertation of the same size would be required. Thank you all - you know who you are!

I would like to express my sincere gratitude to my advisors Prof. Rami Qahwaji and Dr. Stan Ipson for the continuous support of my PhD study and related research, for his patience, motivation, and immense knowledge. Their guidance helped me in all the time of research and writing of this thesis. I could not have imagined having better advisors and mentor for my PhD study.

I would like to show my gratitude to all members involved in this project, professors and medical doctors, who provided me an inspiring working environment and significant support over the course of this project. Prof. A. M. Morgado (University of Coimbra, Portugal) for kindly providing the CCM images with the manually traced ground-truth images for the first dataset of epithelium layer and Prof. Rayaz A. Malik ( Division of Medicine, Weill Cornell Medical College in Qatar, Doha, Qatar) and Centre for Endocrinology and Diabetes, Institute of Human Development, University of Manchester and the Manchester Royal Infirmary, Central Manchester Hospital Foundation Trust, Manchester, U.K.), for kindly providing the CCM images for the second dataset of epithelium layer and the dataset of endothelium layer. In addition to his clinical supervision and evaluation to all the results obtained during this PhD. Thesis.

I would like to thank my friends and colleagues for accepting nothing less than excellence from me. I like to thank them for their encouragement, support and discussions. I must express my very profound gratitude to my parents for their prayers, endless love and encouragement and to my brothers and sister for supporting me spiritually throughout writing this thesis and my life in general.

Last but not the least; I would like to thank my beloved husband (Alaa S. Al-Waisy) for providing me with unfailing support and continuous encouragement throughout my years of study and through the process of researching and writing this thesis. My sweetheart sons (Fahad and Taim) I feel like I have to thank you already. Not just for the sleepless nights, when trying to finish my PhD and looking after you has caused havoc, but for the great time we are going to have together and your smiles, which gave me a special power. This accomplishment would not have been possible without all of them.

**Shumoos T. Al-Fahdawi**

© 2018

## **Dedication**

This work is humbly dedicated to all my valuable  
treasures in my life:

To my parents, brothers and sisters,

To my beloved husband, Alaa S. Al-Waisy

And

To my little sons, Fahad and Taim

**Shumoos T. Al-Fahdawi**

© 2018

## List of Publications

### Journal Papers:

- Shumoos Al-Fahdawi, Rami Qahwaji, Alaa S. Al-Waisy, Stanley Ipson, Rayaz A. Malik, Arun Brahma, and Xin Chen, “A fully automatic nerve segmentation and morphometric parameter quantification system for early diagnosis of diabetic neuropathy in corneal images,” *Comput. Methods Programs Biomed.*, vol. 135, pp. 151–166, 2016.
- Shumoos Al-Fahdawi, Rami Qahwaji, Alaa S. Al-Waisy, Stanley Ipson, Maryam Ferdousi, Rayaz A. Malik, and Arun Brahma, “A Fully Automated Cell Segmentation and Morphometric Parameter System for Quantifying Corneal Endothelial Cell Morphology,” *Comput. Methods Programs Biomed.*, vol. 160, pp. 11–23, 2018.
- Alaa S. Al-Waisy, Rami Qahwaji, Stanley Ipson, Shumoos Al-Fahdawi, "A multimodal deep learning framework using local feature representations for face recognition", *Machine Vision and Applications-Springer.*, vol. 29, no. 1, pp. 35–54, 2017.
- Alaa S. Al-Waisy, Rami Qahwaji, Stanley Ipson, Shumoos Al-Fahdawi, "A Multi-biometric Iris Recognition System Based on a Deep Learning Approach" , *Pattern Analysis and Applications-Springer.*, pp. 1–20, 2017.
- Adnan Khan, Naveed Akhtar, Saadat Kamran, Georgios Ponirakis, Hamad Al-Muhanadi, Ioannis N. Petropoulos, Paula Bourke, Shumoos Al-Fahdawi, Rami Qahwaji, Ashfaq Shuaib and Rayaz A. Malik, Corneal Confocal Microscopy detects alterations in Corneal Endothelial Cell Morphology in Patients Admitted with Acute Ischemic Stroke, *In progress*, 2018.

### Conference Papers:

- Shumoos Al-Fahdawi, Rami Qahwaji, Alaa S. Al-Waisy, and Stanley Ipson, “An automatic corneal subbasal nerve registration system using FFT and phase correlation techniques for an accurate DPN diagnosis,” *2015 IEEE International Conference on Computer and Information Technology; Ubiquitous Computing and Communications; Dependable, Autonomic and Secure*

*Computing; Pervasive Intelligence and Computing*, pp. 1035–1041, 2015.

- Alaa S. Al-Waisy, Rami Qahwaji, Stanley Ipson, Shumoos Al-Fahdawi, "A Fast and Accurate Iris Localization Technique for Healthcare Security System", *2015 IEEE International Conference on Computer and Information Technology; Ubiquitous Computing and Communications; Dependable, Autonomic and Secure Computing; Pervasive Intelligence and Computing*, pp. 1028-1034, 2015.
- Alaa S. Al-Waisy, Rami Qahwaji, Stanley Ipson, Shumoos Al-Fahdawi, "A Robust Face Recognition System Based on Curvelet and Fractal Dimension Transforms", *2015 IEEE International Conference on Computer and Information Technology; Ubiquitous Computing and Communications; Dependable, Autonomic and Secure Computing; Pervasive Intelligence and Computing*, pp. 548-555, 2015.
- Alaa S. Al-Waisy, Rami Qahwaji, Stanley Ipson, Shumoos Al-Fahdawi, "Multimodal Biometric System for Personal Identification Based on Deep Learning Approaches", *2017 Seventh International Conference on Emerging Security Technologies (EST)*, pp.163-168, 2017.

#### **Demos & Presentations:**

- Shumoos Al-Fahdawi, Rami Qahwaji, Alaa S. Al-Waisy, Stanley Ipson, Rayaz A. Malik, Arun Brahma, "A Fully Automated Cell Segmentation and Morphometric Parameter System for Quantifying Corneal Endothelial Cell Morphology", *Digital Health Enterprise Zone Academic Launch Event, DHEZ Academic, Phoenix, University of Bradford*, Sep. 29, 2017.
- Shumoos Al-Fahdawi, Rami Qahwaji, Alaa S. Al-Waisy, Stanley Ipson, Rayaz A. Malik, Arun Brahma, Xin Chen, "Automated Diagnosis of Diabetic Neuropathy from Corneal Images", *The Digital Health and Wellbeing Festival at the Digital Exchange, University of Bradford*, Wed. 29-Thu. 30 June, 2016.
- Alaa S. Al-Waisy, Rami Qahwaji, Stanley Ipson, Shumoos Al-Fahdawi, "A Multi-biometric Iris Recognition System Based on a Deep Learning Approach", *University of Bradford*, 12 Oct. 2017.

## Posters:

- Shumoos Al-Fahdawi, Rami Qahwaji, Alaa S. Al-Waisy, Stanley Ipson, Rayaz A. Malik, Arun Brahma, "Automated Diagnosis of Diabetic Neuropathy from Corneal Images" , *Digital Health Enterprise Zone Academic Launch Event, DHEZ Academic, Phoenix, University of Bradford, Sep. 29, 2017.*
- Shumoos Al-Fahdawi, Rami Qahwaji, Alaa S. Al-Waisy, Stanley Ipson, Rayaz A. Malik, Arun Brahma, Xin Chen "A Fully Automatic Nerve Segmentation and Morphometric Parameter Quantification System for Early Diagnosis of Diabetic Neuropathy in Corneal Images", Accepted for presentation at the 1st Annual Innovative Postgraduate Research Conference (1<sup>st</sup> AIERC), University of Bradford, July 17, 2017.
- Alaa S. Al-Waisy, Rami Qahwaji, Stanley Ipson, Shumoos Al-Fahdawi. "A Multimodal Deep Learning Framework Using Local Feature Representations for Face Recognition", Accepted for presentation at the 1st Annual Innovative Postgraduate Research Conference (1<sup>st</sup> AIERC), University of Bradford, July 17, 2017.
- Rami Qahwaji, Shumoos Al-Fahdawi, Alaa Al-Waisy, Rayaz A. Malik, Maryam Ferdousi, and Arun Brahma, "Novel Imaging Technologies for the Quantification of Nerve Structures from Corneal Confocal Images ", The transformative potential of data and image analysis for eye care, The Royal Society, London, 6-9 Carlton House Terrace, April, 23-24, 2018.



# Table of Contents

<b>Abstract</b> .....	<b>i</b>
<b>Acknowledgements</b> .....	<b>ii</b>
<b>Dedication</b> .....	<b>iii</b>
<b>List of Publications</b> .....	<b>iv</b>
<b>Table of Contents</b> .....	<b>vii</b>
<b>List of Figures</b> .....	<b>ix</b>
<b>List of Tables</b> .....	<b>xiii</b>
<b>List of Abbreviations</b> .....	<b>xiv</b>
<b>1. Chapter One: Introduction</b> .....	<b>1</b>
1.1 Basic Optic Anatomy and Physiology. ....	1
1.2 The Normal Cornea Structure.....	4
1.3 Diabetes Effects on Ocular Health.....	6
1.4 Corneal Imaging Techniques.....	10
1.4.1 In Vivo Confocal Microscopy (IVCM).....	10
1.4.2 Ocular Coherence Tomography (OCT). ....	12
1.5 Problem Definition. ....	13
1.6 Aims and Objectives.....	15
1.7 Contributions. ....	18
1.8 Outline. ....	20
<b>2. Chapter Two: Literature Review</b> .....	<b>23</b>
2.1 Introduction. ....	23
2.2 Corneal Sub-Basal Epithelium Nerve Analysis.....	23
2.3 Corneal Nerve Registration Techniques.....	27
2.4 Corneal Endothelium Cells Analysis.....	28
2.5 Current Challenges and Knowledge Gaps. ....	32
2.6 Summary.....	33
<b>3. Chapter Three: Cornea Sub-Basal Epithelium Analysis</b> .....	<b>35</b>
3.1 Introduction. ....	35
3.2 The Proposed Methodology. ....	38
3.2.1 Data Used. ....	39
3.2.2 Pre-processing Stage. ....	40
3.2.2.1 Diffusion Filtering .....	41
3.2.2.2 Hybrid Diffusion With Continuous Switch (HDGS) .....	43
3.2.2.3 Diffusion Schemes .....	44
3.2.3 Morphological Operations Stage.....	46
3.2.4 Edge Detection Stage .....	50
3.2.5 Morphometric Parameters Quantification Stage.....	53
3.2.5.1 Nerve Length.....	53

3.2.5.2 Nerve Density .....	54
3.2.5.3 Tortuosity Coefficient .....	54
3.2.5.4 Nerve Thickness .....	55
3.3 Experimental Results.....	56
3.4 Summary .....	68
<b>4. Chapter Four: Corneal Epithelium Registration System .....</b>	<b>69</b>
4.1 Introduction .....	69
4.2 The Proposed Methodology .....	72
4.3 Corneal Nerve Registration System .....	74
4.3.1 Image Registration .....	75
4.3.2 Image Segmentation .....	77
4.3.3 Corneal Image Map .....	79
4.4 Experimental Results.....	81
4.5 Summary .....	84
<b>5. Chapter Five: Cornea Endothelium Analysis .....</b>	<b>85</b>
5.1 Introduction.....	85
5.2 The Proposed Methodology .....	88
5.2.1 Data Used .....	89
5.2.2 Pre-processing step .....	90
5.2.3 Cell Contour Detection Step .....	92
5.2.4 Morphometric Parameters Quantification Stage .....	94
5.3 Experimental Results .....	98
5.4 Summary.....	113
<b>6. Chapter Six: Conclusions and Future Work .....</b>	<b>115</b>
6.1 Conclusions.....	115
6.2 Future Work.....	122
<b>References .....</b>	<b>125</b>
<b>Appendices.....</b>	<b>134</b>
<b>Appendix A: Canny Edge Detection.....</b>	<b>134</b>
<b>Appendix B: Cornea Sub-Basal Epithelium System-GUI.....</b>	<b>136</b>
<b>Appendix C: Cornea Endothelium Analysis System (CEAS)-GUI</b> <b>.....</b>	<b>139</b>

## List of Figures

Fig. 1.1: Anatomical structure of human eye (Acharya et al. 2008).....	2
Fig. 1.2: The anatomy of the human eye and the cornea (a) Section of the frontal part of the human eye, (b) Six layers from the anterior to the posterior cornea, (c) In Vivo corneal confocal microscopy image of the corneal epithelium and endothelium layers. Adopted from (Navaratnam et al. 2015).....	5
Fig. 1.3: In Vivo confocal microscopy (IVCM) images (Heidelberg Retina Tomograph – Rostock Cornea Module (HRT-RCM), (400x400) $\mu\text{m}$ ) (a) Superficial epithelial cells, (b) Basal epithelial cells, (c) Sub-basal nerves with Bowman layer, (d) Anterior Stroma with hyper reflective keratocyte nuclei, (e) Stromal nerve, (f) Endothelium (Reinhard & Larkin 2013).....	11
Fig. 1.4: Spectral Domain anterior segment Ocular Coherence Tomography (SD-OCT) images: (a) Normal cornea and (b) Avellino corneal dystrophy (Reinhard & Larkin 2013).....	13
Fig. 1.5: Representative examples of CCM images with different types of noise and artifacts: (a) Corneal tissue deformation, (b) Illumination artifacts and blood vessel, (c) Blurring effect due to saccadic eye movement, (d) Unwanted structures, (e) Stromal cells, (f) Depth differences and unwanted bright structures, (g) and (h) Illumination artifacts (Otel 2012). .....	15
Fig. 1.6: Chapters' organization and the dependence among dissertation chapters.....	22
Fig. 3.1: Overview of the automatic proposed corneal nerve segmentation and quantification system. ....	38
Fig. 3.2: Images from the dataset used. The first two images from the top side are from healthy control subjects, while the last two images are from diabetic patients.....	40
Fig. 3.3: Notations for (a) The standard discretization scheme and (b) The non-negative discretization scheme.....	44
Fig. 3.4: Corneal nerve segmentation system outputs: (a) Original corneal image, (b) Coherence filter output, (c) Gaussian filter output, (d) Morphological operations stage output, (e) Segmented image from the edge detection stage, (f) Automatically traced corneal sub-basal nerves, (g) Manually traced corneal sub-basal nerves.. ....	49
Fig. 3.5: The main implemented approaches in the edge detection stage. ....	52

Fig. 3.6: Nerves' connection procedure: (a) Two segmented images with disconnected nerves circled in red, (b) The binary circular structure element (white circles) drawn at the endpoints, and (c) Output image with connected nerves. ....	52
Fig. 3.7: The thickness algorithm output: (a) Labelling of corneal nerves 1, 2 and 3 in green, blue and red, respectively, (b) Image map for the corneal nerves with their average thickness values indicated.. ....	56
Fig. 3.8: (a) A segmented image, (b) The binary form of ground-truth image, (c) The SSIM index map.. ....	58
Fig. 3.9: Descriptive statistics of the segmentation system performance of the Control group of the first database, where a higher value of SSIM and PRI is better and a lower value of Vol and GCE is better. ....	61
Fig. 3.10: Descriptive statistics of the segmentation system performance of the patient group of the first database, where a higher value of SSIM and PRI is better and a lower value of Vol and GCE is better.. ....	61
Fig. 3.11: The output of the single scale dual-model detector: The images in the top row are the original images, while the bottom row is their response (Dabbah et al. 2011).. ....	63
Fig. 3.12: A readable text file format showing clinical features extracted from the first database. ....	64
Fig. 3.13: Representative box-plots with (median, inter-quartile range, outliers, and extreme cases of each parameter) illustrating the extracted clinical features from the first database: (a) Average Nerve Tortuosity, (b) Average Nerve thickness, and (c) Average Nerve Length, (d) Average Nerve Density.. ....	66
Fig. 3.14: Representative box-plots with (median, inter-quartile range, outliers, and extreme cases of each parameter) illustrating the extracted clinical features from the second database: (a) Average Nerve Tortuosity, (b) Average Nerve Thickness (c) Average Nerve Length, and (d) Average Nerve Density. ....	67
Fig. 4.1: The main steps of the proposed corneal sub-basal nerve registration system to generate a colour coded corneal nerve image map.. ....	75
Fig. 4.2: Overview of the automatic Fourier and phase correlation based image registration algorithm.. ....	77
Fig. 4.3: Applying the image registration algorithm on three sequenced CCM images where the last column represents the output.. ....	78
Fig. 4.4: Corneal nerve segmentation system outputs: (Top) row is the original corneal images and (Bottom) row is binary segmented images. ....	79

Fig. 4.5: The colour coded corneal nerve image map of the nerve tortuosity: top row represents the control group, while bottom row represents the patients group..... 80

Fig. 4.6: Representative box-plots with (median, inter-quartile range, outliers, and extreme cases of each parameter) illustrating the extracted clinical features from the controls and patients group: (a) ANT (b) ANTh, (c) ANL and, (d) AND..... 83

Fig. 5.1: An illustration of the process for the automated corneal cell segmentation and quantification system (CEAS)..... 89

Fig. 5.2: Examples of original corneal endothelial cell images with different types of noise and artifacts: (a) Darker areas in the peripheral regions, (b) Non-uniform illumination with blurring effect due to saccadic eye movement, and (c) Darker areas with unwanted bright objects..... 90

Fig. 5.3: Corneal cell segmentation system outputs: (a) Original corneal image, (b) Applying FFT-Band-pass filtering, (c) Binarized image, (d) Applying watershed approach, (e) Applying Voronoi tessellation, (f) Labeling of endothelial cells (g) Final endothelial cells segmentation result, and (h) Automatically traced endothelial cells boundaries.. ..... 93

Fig. 5.4: A readable text file format showing morphological features associated with the health state of corneal endothelium. .... 96

Fig. 5.5: (a) Original corneal endothelial image and (b) Endothelial cell segmentation results with red color indicating the cells that have been ignored. .... 97

Fig. 5.6: (a) Final endothelial cells segmentation result and (b) Using the color of a cell to indicate its number of neighbors using the color code given on the right. The most common color is orange corresponding to six neighbors..... 97

Fig. 5.7: GIMP program outputs: (a) Original image, (b) A representative example of manually traced cells contours, (c) Generated binary image used as a ground-truth manual segmentation inside the ROI..... 101

Fig. 5.8: Descriptive statistics of the CEAS segmentation system performance on *Database\_1*, where a higher value of PRI and SSIM is better and a lower value of GMSD, Vol MSE, NAE and GCE `are better.. ..... 102

Fig. 5.9: A comparison example of an image taken from the *Database\_1*: (a) Original image, (b) A manually traced cell contours, (c) The output of the proposed CEAS system, and (d) The output of the BestFit system... ..... 102

Fig. 5.10: Correlation plots for each pair of manual and automatic morphometric parameters from *Database\_1*, showing significant correlations. The solid lines are the linear regression lines: (a) Cell density, (b) Cell area, (c) Cell perimeter, (d) Polymegathism, and (e) Pleomorphism... .. 107

Fig. 5.11: Bland-Altman plots showing difference versus average for each pair of manual and automatic estimations of: (a) Cell density, (b) Cell area, (c) Cell perimeter, (d) Polymegathism, and (e) Pleomorphism from *Database\_1*. Solid lines (mean differences), dashed lines (95% limits of agreement).... .. 108

Fig. 5.12: Comparison between manual and automated segmentation outputs: (a) Original image, (b) Manually traced cells, (c) Automatically segmented cells..... 109

Fig. 5.13: An illustration of the semi-automatic corneal endothelium system used in the HRT Rostock Cornea Module (Heidelberg Engineering GmbH; Heidelberg; Germany) for cell density estimation..... 110

Fig. 5.14: (a) Original image, (b) Manually over picked cells as shown in the red circle, (c) Automatically segmented cells..... 111

Fig. 5.15: Correlation plot of automated and manual cell densities with a significant correlation on *Database\_2*..... 112

Fig. 5.16: Bland-Altman plot showing mean difference and limits of agreement between manual and automated cell densities on *Database\_2*..... 113

Fig. 6.1: An initial evaluation of the proposed nerve segmentation algorithm using retinal ICG images: (a) Original retinal image and (b) Automatically traced retinal nerves..... 124

## List of Tables

Table 3.1: Summary of the descriptive clinical features of manually and automatically traced nerves extracted from the first database.....	65
Table 4.1: The descriptive summary of the clinical features before and after applying the proposed corneal sub-basal nerve registration system. .....	84
Table 5.1: Performance comparison made between the manual and automated estimations of five morphometric parameters in 40 corneal images of <i>Database_1</i> . The differences between the manual and automatic estimates are listed and also as a percentage.....	105
Table 5.2: Performance comparison between the manual and automated cell density estimates using <i>Database_2</i> ..	112

## List of Abbreviations

<b>Symbol</b>	<b>Definition</b>
ACM	Active Contour Model
ANL	Average Nerve Length
ANT	Average Nerve Tortuosity
AS-OCT	Anterior Segment Optical Coherence Tomography
BCS	Boundary Contour System
CCM	Corneal Confocal Microscopy
CEAS	Corneal Endothelium Analysis System
CED	Coherence-Enhancing Diffusion
CV	Coefficient of Variation
DFT	Discrete Fourier Transform
DPN	Diabetic Peripheral Neuropathy
ECD	Endothelial Cell Density
EED	Edge-Enhancing Diffusion
FFT	Fast Fourier Transform
GCE	Global Consistency Error
GMSD	Gradient Magnitude Similarity Deviation
GP	Genetic Programming
GUI	Graphical User Interface
HC	Hexagonality Coefficient
HDCS	Hybrid Diffusion filter with a Continuous Switch
HRT	Heidelberg Retina Tomograph
IFFT	Inverse Fast Fourier Transform
IVCM	In Vivo Confocal Microscopy



LQM	Local Quality Map
MCA	Mean Cell Area
MCD	Mean Cell Density
MCP	Mean Cell Perimeter
MSE	Mean Square Error
NAE	Normalized Absolute Error
NN	Neural Networks
OCT	Ocular Coherence Tomography
Pleomorphism	Percentage of Hexagonality Coefficient
POC	Phase-Only Correlation
Polymegathism	Coefficient of Variation in cell size
PRI	Probabilistic Rand Index
RF	Random Forest
ROI	Region of Interest
SIFT	Scale Invariant Feature Transform
S-PSO	Snake model and the Particle Swarm Optimization
SSCM	Slit-Scanning Confocal Microscope
SSIM	Structural SIMilarity Index
SURF	Speeded-Up Robust Features
SVM	Support Vector Machine
SVM	Support Vector Machine
TPS	Thin-Plate Spline
TSCM	Tandem Scanning Confocal Microscope
Vol	Variation of Information

# Chapter 1

## Introduction

The eyes are certainly the most sensitive organs that we possess and possibly the most surprising thing. The eyes allow us to view the world and distinguish objects through the optical window and besides that, the eyes are responsible for four-fifths of the whole of the information that the brain receives, which is probably the reason of why we depend on our eyesight more than any other sense.

The eye is small with size about 24-25 mm in sagittal diameter and is a complicated organ. In addition, the system in which the eye functions is extremely complex.

### 1.1 Basic Optic Anatomy and Physiology

Human eye comprises fundamentally of six regions: the cornea, sclera, aqueous humor, iris, lens and vitreous humor. Other optic domains include the retina and choroid. The retina is the part that is light sensitive and where light energy is converted to neural signals. The choroid is an extremely vascularized structure in the eye that accounts for 85% of the total optic blood flow. The eye has a form quite close to a spherical shape. A human eye usually has a radius of 12 mm and length of the pupillary axis, which is measured by the distance between the cornea and the posterior part of the eye of between 23 and 25 mm. The anatomical structure of the human eye is shown in Figure 1.1. The following components are major components of the human eyes (Acharya, Ng and Suri, 2008):

### a) Cornea

The cornea is the transparent outer facing layer of the eye which is exposed to the environment. It has a water content of 78% and an elliptical shape on average 12mm in the horizontal axis and 11 mm in the vertical axis (Mapstone, 1970). The corneal thickness is not uniform and is about 530 microns in the central region. The main functions of the cornea are to refract and transmit light. The cornea is avascular, which means that it lacks blood vessels inside it. The cornea needs an oxygen supply which is obtained from the atmosphere by absorption through the tear film.

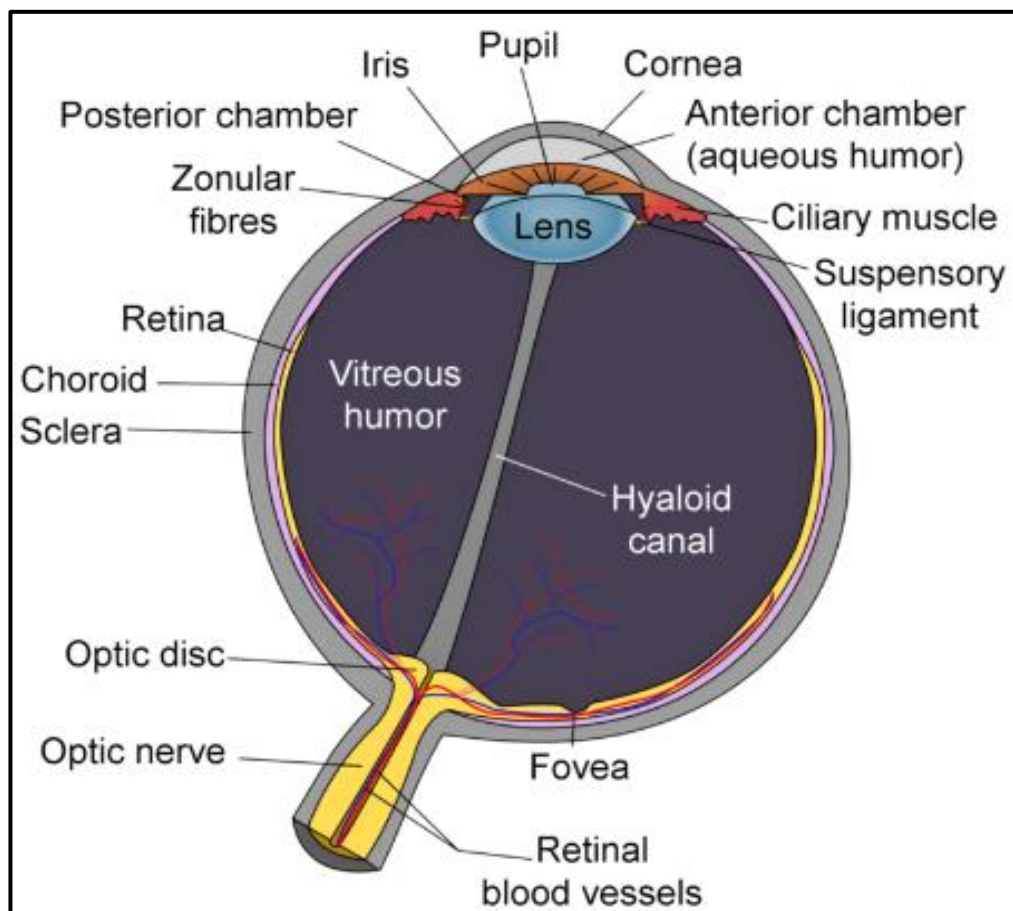


**Figure 1.1:** Anatomical structure of human eye (Acharya, Ng and Suri, 2008).

**b) The Aqueous Humor**

The anterior chamber between the cornea and pupil contains the fluid aqueous humor. The aqueous fluid is made up mainly of water which supplies nutrients to the lens and avascular cornea. The aqueous flow has hydrodynamic properties which generate an intraocular pressure (IOP) which reaches 15 mmHg for normal human eyes (Acharya, Ng and Suri, 2008).

**c) The Iris**

The iris consists of pigmented fibrovascular tissues known as the stroma. The main function of the iris is to control the pupil size and adjust the amount of light entering the eye. It is also responsible for determining eye colour. The pupil diameter size depends on the lighting conditions. Relative to the iris, the eye structure is divided into anterior and posterior regions (Acharya, Ng and Suri, 2008). The region at the front of the iris is the anterior region, while the region at the back of the iris is the posterior region.

**d) The Lens**

The lens structure is biconvex with a central thickness of between 3.5 and 5 mm which is dependent on age. The main lens function is to focus the light that comes into the eye onto the retina. The lens is avascular and consists of 65% water and 35% protein (Hill, R. M., 1965). The content of water inside the lens increases with age.

**e) The Vitreous Humor**

The vitreous humor comprises the largest volume of the human eye and fills up the space between the retina and the lens with a pure aqueous

solution that consists of 98.5% to 99.7% water (Acharya, Ng and Suri, 2008). The eye takes its spherical structure from the vitreous humor. The vitreous works as a storage region for metabolites of the lens and retina.

#### **f) The Sclera**

The sclera is the white outer layer of the eye normally referred to as the white of the eye and wraps around five-sixths of the posterior eyeball. The sclera thickness is non-uniform. A few blood vessels passing through it provide the blood for the sclera. The choroid and retinal layers are beneath the sclera (Mapstone, 1968).

## **1.2 The Normal Cornea Structure**

Human cornea is a transparent layer which covers the front surface of the eye. The Cornea transmits and helps focus light onto the retina. The lens and the cornea are the refracting components of the eye. As shown in Figure 1.2, the cornea is formed of five layers, covering crucial internal structures of the human eye, including the iris, pupil, lens, and anterior chamber. The epithelium of (50  $\mu\text{m}$ ) thick is the outermost layer, then Bowman's membrane (12  $\mu\text{m}$ ), the stroma (480–500  $\mu\text{m}$ ), Descemet's membrane (8–10  $\mu\text{m}$ ), and finally the endothelium (5  $\mu\text{m}$ ), innermost (Nishida, 2005). Few years ago, another layer was detected in the cornea, called Dua's layer, as described in (Dua *et al.*, 2013). Each layer of the cornea has an important function. The epithelium is the outer layer and its primary function is to prevent the crossing of foreign materials, such as bacteria, dust and water into the eye and to other layers of the cornea. The epithelium surface is so smooth that it easily absorbs oxygen and nourishment from tears and distributes them to the rest of the cornea (Acharya, Ng and Suri, 2008).

The epithelium contains many tiny nerve endings, which make the cornea highly sensitive to pain when scratched or rubbed. A transparent sheet of tissue below the epithelium is known as Bowman's layer. This layer is strong and composed of protein fibres called collagen. In injured state, Bowman's layer may create a scar. If these scars are big enough and centrally located, vision loss may occur. Under the Bowman layer is the stroma layer, which makes up about 90% of the thickness of the cornea. It is mostly 78% water and 16% collagen and does not contain blood vessels. Beneath the stroma layer is Descemet's membrane, this layer is a thin but strong sheet of tissue, which works as a protective barrier against injuries and infection (Acharya, Ng and Suri, 2008).

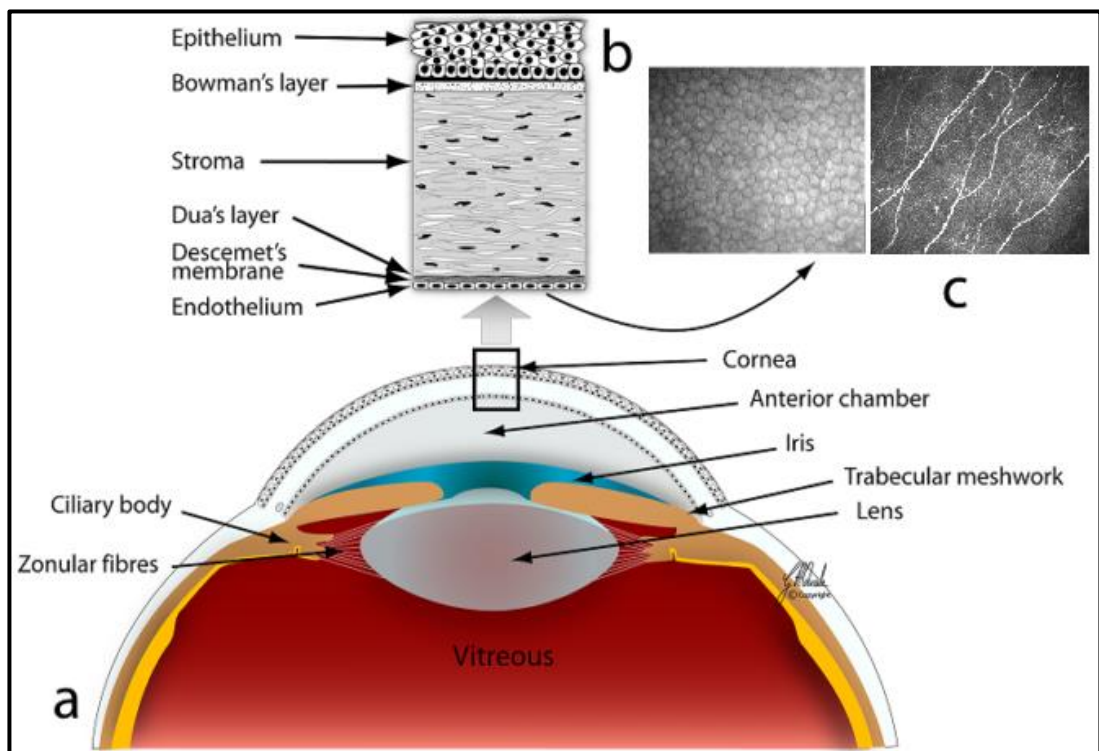


**Figure 1.2:** The anatomy of the human eye and the cornea (a) Section of the frontal part of the human eye, (b) Six layers from the anterior to the posterior cornea, (c) In Vivo corneal confocal microscopy image of the corneal epithelium and endothelium layers. Adopted from (Navaratnam *et al.*, 2015).

Descemet's membrane includes collagen fibres which are considered different from those of the stroma layer and are supported by the endothelial cells layer that lies below it. In the injured state, Descemet's membrane layer regenerates (Acharya, Ng and Suri, 2008). The endothelium layer is extremely thin and the deepest layer of the cornea. The cells of endothelial are necessary to keep the cornea transparency by preserving the balance of the liquid in the cornea. The role of the endothelium is to pump excess liquid that leaks from inside the eye into the stroma layer, then out of the cornea into the aqueous humor. Without this mechanism, the stroma will swell with water and become hazy. At birth, the cells of a normal corneal endothelium are uniformly sized with regular hexagonal shapes and a honeycomb appearance (McCarey, Edelhauser and Lynn, 2008). This regular appearance is influenced by pathologies and ageing causing cells to die, with no new cells replacing them, thereby resulting in permanent damage to the endothelium. Once endothelial cells are destroyed, they are lost forever, the surrounding cells extend to fill holes, hence increasing the average size of the endothelial cells and producing variations from the regular hexagonal shape throughout life. If too many cells are destroyed, blindness ensues, with corneal transplantation being the only available therapy (Vincent, 1992).

### **1.3 Diabetes Effects on Ocular Health**

The diabetes is the main cause of permanent blindness in adults. Type 1 diabetes accounts for approximately 10% of the autoimmune etiology that broadly affects children and young people, while Type 2 diabetes accounts for approximately 90% of cases, which are mainly linked with insulin resistance and obesity. The Diabetic Peripheral Neuropathy (DPN) is one of the most common

types of diabetes that can affect the ocular tissues, which results in around 12,000 to 24,000 new occurrences of blindness every year (Skarbez et al. 2010). For example, in 2015, the American Diabetes Association<sup>1</sup> reported that, out of 30.3 million (9.4%) of the total US population, about 23.1 million people were diagnosed with diabetes and an estimated 7.2 million people were undiagnosed. Approximately, 79,535 death certificates were associated with this disease, which put it as the 7th leading cause of death in the United States in 2015. In the UK, most health experts reported that diabetes remains one of the biggest health problems facing the UK population, due to the large increase in the number of people diagnosed with diabetes, which has increased from 1.4 million to 2.9 million, since 1996. By 2025, about 5 million people will have this disease, whether diagnosed or undiagnosed. Most of them are expected to be diagnosed with Type 2 diabetes, due to the ageing population problem and rapidly increasing numbers of obese and overweight people (DiabetesUK, 2012). Hence, it is significant that ophthalmologists pay close attention to pathological changes in their diabetic patients, so all abnormal cases can be diagnosed and treated early (Skarbez *et al.*, 2010). The wide ranges of diabetic complications that affect ocular tissues are reviewed briefly, as follows:

- a) Conjunctiva:** Diabetics are at the highest risk of developing bacterial infections of the conjunctiva, especially acute infectious conjunctivitis. The infective conjunctiva is an infection that affects the front skin of one or both eyes. A number of significant symptoms can be noted in affected patients, such as the whites of one or both eyes appearing inflamed, and red or

---

<sup>1</sup> American Diabetes Association website: <http://www.diabetes.org/diabetes-basics/statistics/>



pink. According to many studies, up to 86% of diabetic patients have abnormal changes in the conjunctiva (Schönheyder, 2006).

- b) Dry Eye:** One of the most common conditions in diabetic patients is the dry eye syndrome, which can result in reduced corneal sensitivity. This leads to the negative effect of not making enough reflex tears, so the eye becoming inflamed (red and swollen) (Najafi *et al.*, 2013).
- c) Lids/Lashes:** This disease is reported as yellowish collections of cholesterol, which is more common in diabetic patients. These collections of cholesterol do not cause any pain and can be easily treated under the skin on or around the lids (Negi and Vernon, 2003).
- d) Cornea:** Neurotrophic Keratopathy is the degenerative disease of the corneal epithelium layer, which is responsible for several corneal complications, such as repeated corneal erosions, persistent epithelial defects and disabled corneal innervation. These corneal complications have been connected to decreased sensitivity of the cornea, tear secretion abnormalities and poor cohesion between epithelium cells and the basement membrane (Choo *et al.*, 2010).
- e) LASIK:** This refers to the most common laser eye surgery for the correction of myopia, hyperopia, and astigmatism. As a result of it increasing corneal defects, some concerns have been raised about whether Laser-Assisted in situ keratomileusis (LASIK) can be safely performed on diabetic patients. Several studies have reported an increased incidence of epithelial complications in diabetic patients caused by LASIK (Jabbur *et al.*, 2004).

- f) Contact Lenses:** Several studies have shown that diabetic patients are at a higher risk of developing contact lens complications than non-diabetic patients, especially, patients who wear contact lenses for a long period. Moreover, glucose levels in diabetic patient's tears are higher than in non-diabetics, which can increase the opportunity for eye infections (O'Donnell and Efron, 2012).
- g) Iris:** Neovascularization is the most serious consequence of diabetes that can be observed around the pupil region and the complete iris surface in advanced cases. Several clinical reports have pointed out that Neovascularization can be found in up to 7 % of diabetic eyes and 60% of eyes with proliferative retinopathy. In addition, the iris epithelium in diabetic patients is at higher risk of becoming depigmented. This release of pigment from the iris has a negative effect on the corneal endothelium of diabetic patients (Chen, Chew and Chan, 2015).
- h) Mucormycosis:** Mucormycosis is an uncommon disease, but is very aggressive and is often considered an opportunistic disease that can progress rapidly. This fungal infection affects immunocompromised individuals and Type 1 diabetic patient. It commonly starts in the paranasal sinuses or palate and then spreads to the orbital contents. Some of the hallmarks of this infection are an ocular pain, loss of vision, and ophthalmoplegia. The treatment of this infection comprises an aggressive use of Amphotericin B and surgical debridement (Lee, Holland and Glasgow, 1996).

## **1.4 Corneal Imaging Techniques**

In many clinical cases, an accurate evaluation of corneal structures is required in order to help the ophthalmologists in monitoring and treating different corneal diseases early and efficiently. However, poor resolution of ophthalmic instruments (e.g. the slit-lamp) has always been a challenging problem for ophthalmic clinicians and researchers to get a precise evaluation of corneal structures and monitor the effects of treatments of the different layers of the cornea. To overcome the limitations of poor resolution, new corneal imaging techniques have been developed, such as In Vivo Confocal Microscopy and Optical Coherence Tomography.

### **1.4.1 In Vivo Confocal Microscopy (IVCM)**

IVCM is one of the most sophisticated and non-invasive imaging technique that is used to provide high-resolution images of the cornea, the conjunctiva and the limbus (Reinhard and Larkin, 2013). In 1955, the first confocal microscope was invented by Minsky while he was studying brain parenchyma cells. More recently, combining IVCM with high-performance digital imaging provides high-resolution images of the different layers of the cornea that can be stored and manipulated to produce 2D-images, 3D-images or numerical data such as corneal thickness. Figure 1.3 shows an example of these images captured from different layers of the cornea using IVCM. These images or subsequently extracted data are used to study and monitor both physiological and pathological cornea conditions. In fact, numerous publications have demonstrated the usefulness of IVCM as an important aid tool in the diagnosis and treatment of corneal dystrophies, infectious keratitis and the

assessment of corneal changes after refractive surgery or corneal surgery (Tervo and Moilanen, 2003), (Jalbert *et al.*, 2003b). Over the last few years, the most commonly used types of confocal microscopes have been:

- a) The Tandem Scanning Confocal microscope (TSCM).
- b) The ConfoScan 4 Slit-Scanning Confocal Microscope (ConfoScan 4-SSCM).
- c) The Heidelberg Retina Tomograph Rostock Corneal Module laser scanning confocal microscope (HRT or HRT3).

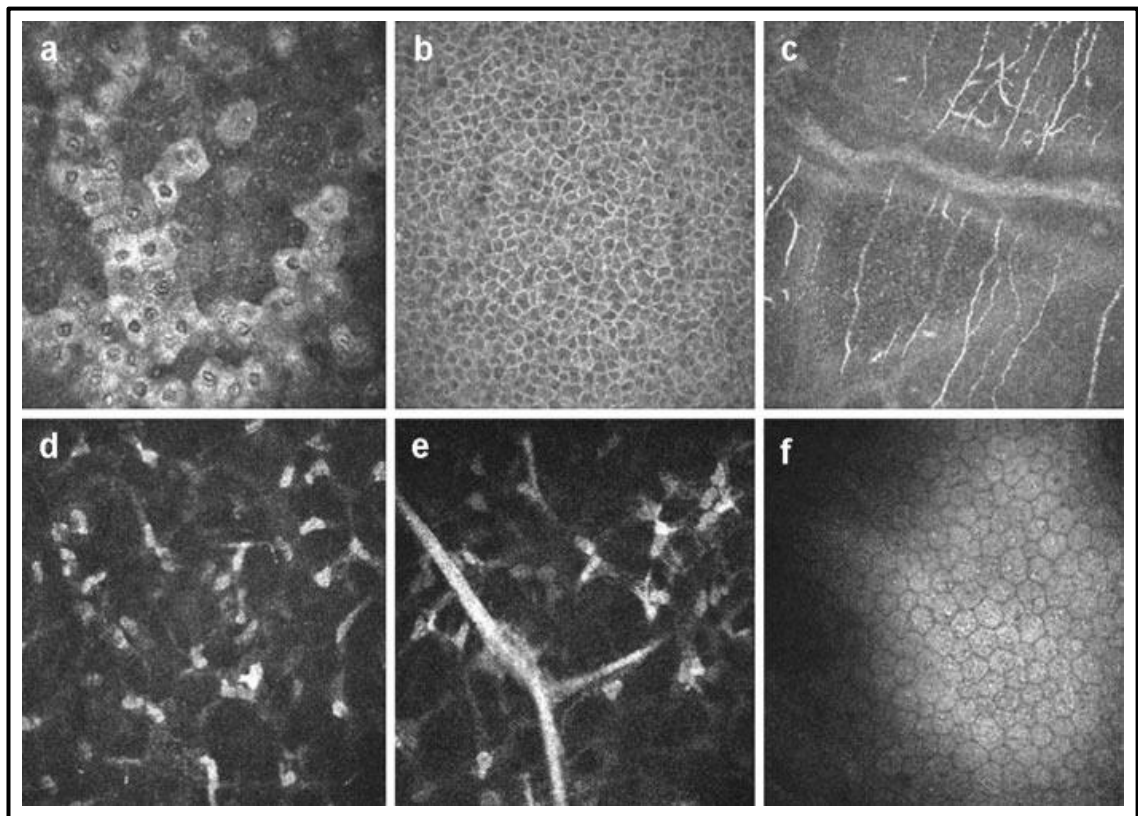


**Figure 1.3:** In Vivo confocal microscopy (IVCM) images (Heidelberg Retina Tomograph – Rostock Cornea Module (HRT-RCM), (400x400)  $\mu\text{m}$ ) (a) Superficial epithelial cells, (b) Basal epithelial cells, (c) Sub-basal nerves with Bowman layer, (d) Anterior Stroma with hyperreflective keratocyte nuclei, (e) Stromal nerve, (f) Endothelium (Reinhard and Larkin, 2013).

### 1.4.2 Ocular Coherence Tomography (OCT)

The OCT is a new, non-invasive imaging technique that uses light waves to capture cross-section images of the retina and the light-sensitive tissue at the back of the eye in a matter of seconds (Carlo et al. 2015). Analysis of the anterior part of the eye structure is also an essential aspect of ophthalmology examinations where many clinical cases require an accurate evaluation not only of the spatial relations but also the dimensions of the structures that comprise this part of the eye (Reinhard and Larkin, 2013). In clinical practice, corneal imaging is usually achieved using the slit lamp, which cannot be considered an objective quantitative evaluation technique. To overcome these limitations, new imaging techniques have been developed, which include anterior segment OCT.

The OCT was first used in analysing the posterior part of the eye, and then a number of modifications and improvements were made in order to capture high-resolution images of the anterior part of the eye, and the resulting technique is now called Anterior Segment Optical Coherence Tomography (AS-OCT). Numerous AS-OCT applications have been proposed, especially in the field of corneal graft and refractive surgery due to the ability of the new AS-OCT devices to measure the entire corneal thickness and the thickness of each corneal layer from the epithelium layer to the endothelium layer. Figure 1.4 shows two anterior segment images acquired using the OCT imaging technique (Zysk *et al.*, 2007).

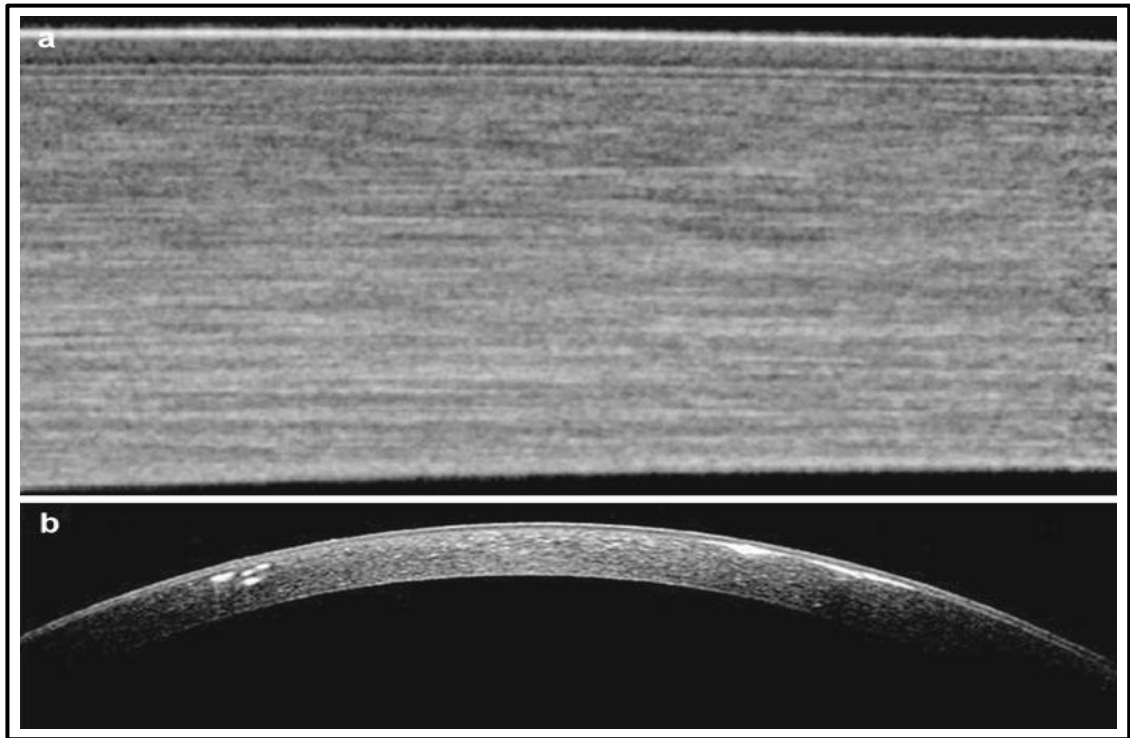


**Figure 1.4:** Spectral domain of the Anterior Segment Ocular Coherence Tomography (SD-OCT) images: (a) Normal cornea and (b) Avellino corneal dystrophy (Reinhard and Larkin, 2013).

## 1.5 Problem Definition

In order to build an efficient and robust system for segmenting sub-basal epithelium nerves and endothelium cells in human corneal confocal images, a number of issues need to be taken into account, as discussed below.

The Corneal Confocal Microscopy (CCM) images usually suffer from different types of artefacts (e.g., blurring, noise, specular reflections, low contrast, non-uniform illumination, etc.) associated with the acquisition process. This is due to a several factors including:

- a) The saccadic eye movement during the scanning process which causes a motion, blurring and/or displacement effects of the nerve fibers.

- b)** The spherical-like shape of the cornea layers which can lead to a non-uniform distribution of the lighting in different areas of the corneal layers, and different attenuation of light along the various paths of illumination. This non-uniform distribution of the lighting causes the CCM images to have darker areas in their peripheral regions in most cases, making the characteristics of the cornea's nerves and cells unclear.
- c)** Subject movement due to breathing and the cardiac pulse occurring during the acquisition process may cause some images to be out of sequence in terms of depth.
- d)** The appearance of small unwanted structures (e.g., basal epithelial cells, nerve deformities, keratocytes, etc.), which are neither corneal sub-basal nerves nor corneal endothelial cells. These artefacts make the detection of the corneal sub-basal nerves and the correct boundaries of the corneal endothelial cells a challenging task. Some representative examples of CCM images with different types of noise and artefacts are shown in Figure 1.5.

A major challenge for carrying out this research is the unavailability of large public benchmark datasets of confocal microscopy images of the cornea. Hence, collaborations with leading experts were formed to provide necessary data for this research. Two datasets have been provided in collaboration with an expert advisory board from the Division of Medicine, Weill Cornell Medicine-Qatar, Doha, Qatar and the Manchester Royal Eye Hospital, Centre for Endocrinology and Diabetes, UK. In addition, one dataset has been provided by a volunteer at the University of Coimbra, Portugal.

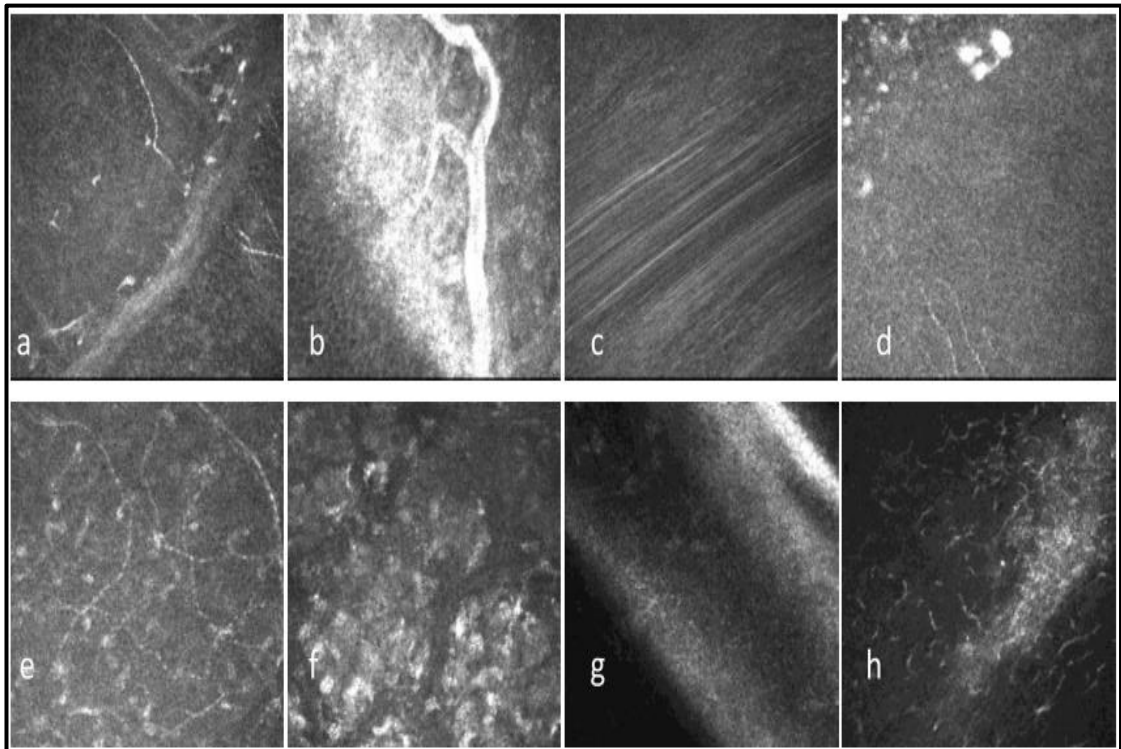


**Figure 1.5:** Representative examples of CCM images with different types of noise and artifacts: (a) Corneal tissue deformation, (b) Illumination artifacts and blood vessel, (c) Blurring effect due to saccadic eye movement, (d) Unwanted structures, (e) Stromal cells, (f) Depth differences and unwanted bright structures, (g) and (h) Illumination artifacts (Otel, 2012).

## 1.6 Aims and Objectives

The main aim of this research is to developing new diagnostic tools for extracting clinical features from the cornea's epithelium and endothelium layers. Abnormalities of both corneal sub-basal nerves and corneal endothelial cells may be associated with a number of corneal and systemic diseases. For instance, damage to the endothelial cells can significantly affect the corneal transparency by altering the hydration of the corneal stroma, which is associated with irreversible endothelial cell pathology requiring corneal transplantation. To date, quantitative analysis of corneal sub-basal nerve and endothelial cell abnormalities has been manually performed by



ophthalmologists using time-consuming and highly subjective semi-automatic tools, which require an operator interaction. Specific objectives are designing and implementing two fast and fully-automated diagnostic systems for these two corneal layers, and extracting meaningful clinical features, which are aimed at helping ophthalmologists in monitoring and treating different corneal diseases early and efficiently. Further objectives are addressing the problem of the discontinuous corneal nerves and developing an automatic corneal sub-basal nerve registration system to address the displacement problem and produce a more informative corneal image that contains structural and functional information. The main objectives of this research work are:

1. Propose efficient and robust image enhancement algorithms to improve the quality of the CCM images. For corneal sub-basal nerves, the emphasis will be on keeping the image structures, while removing noise and unwanted objects. In contrast, using corneal endothelial cells the emphasis will be on correcting the non-uniform illumination and reducing the amount of noise.
2. Development of a fully-automated system that can be used for tracing the sub-basal nerves in corneal images and extracting meaningful clinical features, including thickness, tortuosity, length and density of the nerve to aid in the early diagnosis of DPN and when planning LASIK or Photorefractive keratectomy (PRK).
3. The objective in 2 involves several issues that need to be tackled efficiently, including (i) developing an efficient and fully-automated nerve connection algorithm to connect the discontinuous corneal sub-basal nerves, which result from low visibility of parts of nerves or noise

introduced into the corneal images. Employing this procedure can play a significant role in calculating helpful and meaningful clinical features. (ii) Development of an efficient and accurate nerve thickness algorithm, without any manual intervention.

4. Development of a fully-automated and real-time system for the segmentation and computation of endothelial cells in images of the human cornea obtained by In Vivo CCM. In this task, a number of useful clinical parameters will be extracted and calculated, including Mean Cell Density (ECD), Polymegathism, Pleomorphism, Mean Cell Area (MCA) and Mean Cell Perimeter (MCP). These clinical parameters could play a significant role in the early diagnosis of corneal pathology and in determining the health status of corneas for transplantation.
5. Investigations into the design of an efficient and practical corneal nerve image registration system to produce a more informative corneal nerve image than the original images using a set of sequenced CCM images. This task also involves producing a colour coded corneal image map that can be used to give ophthalmologists an efficient and clear representation of the extracted clinical features for each nerve and layer in the corneal image.
6. Evaluating the performance of the proposed systems and the possibility of utilizing them in real-world clinical setting to enable rapid diagnosis and for patient follow-up. In this task, the effectiveness and robustness of the proposed systems will be evaluated against manually traced benchmark images formulated by ophthalmologists for both corneal sub-basal nerves and corneal endothelial cells.

## 1.7 Contributions

The main results and contributions made in this PhD research can be summarized as follows:

1. Development of an objective, real-time and fully-automated system for tracing the sub-basal nerves in corneal images and extracting meaningful clinical features for the early diagnosis of diabetic neuropathy. In this system, an efficient image enhancement algorithm based on applying the Coherence filter followed by Gaussian filtering to enhance the visibility of the nerves and remove noise. Furthermore, a number of useful and meaningful clinical features are extracted (e.g., nerve tortuosity, nerve thickness, nerve length, etc.) which may be used for early diagnosis of diabetic polyneuropathy and when planning LASIK or PRK.
2. A new nerve connection algorithm is proposed for connecting discontinuous nerves without any manual intervention, which can play a significant role in calculating helpful and meaningful clinical features, such as nerve tortuosity and nerve length that mainly depend on the whole structure of the nerve. In addition, an efficient and accurate nerve thickness algorithm based on distance transform, without any manual intervention, is also proposed.
3. The performance of the proposed corneal sub-basal nerves system has been evaluated against manually traced ground-truth images from two databases. The first database consists of 498 corneal sub-basal nerve images (238 are normal and 260 are abnormal) captured using Heidelberg Retinal Tomograph equipped with a Cornea Rostock Module (HRT-CRM: Heidelberg Engineering, Heidelberg, Germany). While the second

database consists of 919 images taken from healthy subjects and diabetic patients with and without neuropathy using a Heidelberg Retina Tomograph equipped with Rostock Cornea Module (HRT-III). The results obtained demonstrate that the proposed system can be readily used as a useful clinical tool to support the expertise of ophthalmologists and save the clinician time in a busy clinical setting.

4. An automatic corneal sub-basal nerve registration system is proposed to produce a colour coded corneal image map by overlaying a sequence of CCM images that may differ in their displacement, scaling, and rotation to each other. This system produces a new more informative corneal image containing structural and functional information that can be used to give ophthalmologists an efficient and clear representation of the extracted clinical features for each nerve and layer in the corneal image. In addition, the corneal image map can improve the nerve visibility and help with acquiring more precise clinical feature faster instead of manually searching through a sequence of CCM images to extract these features from each image individually.
5. The performance of the proposed corneal sub-basal nerve registration system has been assessed on a database of 30 subjects (18 controls and 12 diabetic patients) with a sequence of CCM images that varies between 3 and 4 images per subject. We have managed to demonstrate the efficiency of the generated corneal image map in providing a better structural and functional information with less execution time compared to the original images by calculating four useful clinical features (e.g., nerve tortuosity, nerve thickness, nerve length and nerve density).

6. A totally automatic, robust and real-time system is proposed, termed the Corneal Endothelium Analysis System (CEAS) for the segmentation and computation of the different morphological parameters of endothelial cells in human cornea obtained by In Vivo corneal confocal microscopy. In this system, an efficient region-based segmentation approach based on the Voronoi Tessellation approach is employed to draw the boundaries of the corneal endothelial cells and ensure that a wider range of corneal endothelial parameters can be derived and analyzed (e.g., endothelial cell density, endothelial cell area, endothelial cell perimeter, polymegathism and pleomorphism).
7. The performance of the proposed CEAS system has been evaluated against manually traced ground-truth images from two databases (each one consisting of 40 images). The images in these databases are acquired using a laser CCM (Heidelberg Retinal Tomograph III Rostock Cornea Module HRT III RCM; Heidelberg Engineering GmbH; Heidelberg; Germany), had very low quality compared to those in the literature. The overall measurement results have demonstrated the efficiency of the proposed CEAS system and the possibility of utilizing it in a real-world clinical setting to enable rapid diagnosis and for patient follow-up, with an execution time of only 6 seconds per image.

## **1.8 Thesis Organization**

This PhD Thesis is organized into six chapters including this chapter. An overview of these chapters is presented below. The chapters' organization and the dependence among these chapters are illustrated in Figure 1.6:

- **Chapter 2** presents literature review of previous investigations into cornea epithelium nerve analysis techniques; cornea nerve registration techniques; and cornea endothelium cells analysis techniques. It also details the motivations for this PhD research based on previous related work.
- **Chapter 3** introduces a robust, fast and fully-automated nerve segmentation and nerve morphometric parameters quantification system for confocal microscope images of the epithelium. This system is considered as a tool for early diagnosis of diabetic neuropathy. In this work, a number of features are extracted, including thickness, tortuosity, length and density of the nerve, which may be used for the early diagnosis of diabetic polyneuropathy
- **Chapter 4** introduces an automatic corneal sub-basal nerve registration system using FFT and phase correlation techniques for an accurate DPN diagnosis. This system is aimed at producing a new informative corneal image that contains structural and functional information of the corneal nerves.
- **Chapter 5** presents a fully-automated, robust and efficient real-time system for the segmentation and computation of morphological parameters associated with endothelial cells in human cornea obtained by In Vivo confocal microscopy. In this system, meaningful clinical parameters to improve diagnostic value are extracted which shows the possibility of utilizing it in real-time for early diagnosis of patients and for follow-up.

- **Chapter 6** presents the overall conclusions, achievements and some limitations of the research. Possible future directions of this research are also outlined In this work.

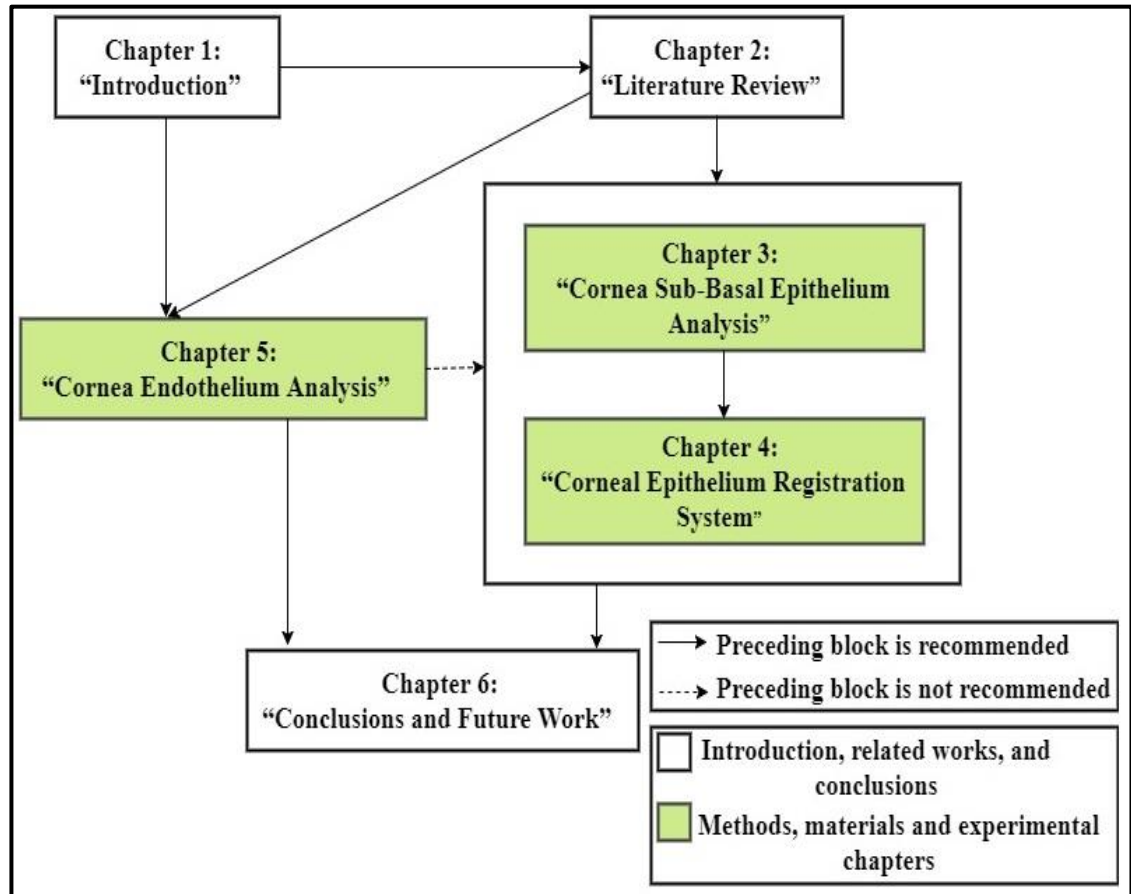


**Figure 1.6:** Chapters' organization and the dependence among dissertation chapters.

# Chapter 2

## Literature Review

### 2.1 Introduction

Over the last few years, researchers have demonstrated an increased interest in the field of automatic segmentation of corneal confocal images. However, the research related to corneal confocal images is limited and most of the systems proposed are incapable of detecting the corneal epithelium nerves or endothelial cells without the aid of manual (interactive) inputs such as the provision of seed points. Most of the methods presented are based on images from a specular microscope, which is excellent for imaging the central corneal. A specular microscope provides high contrast between different endothelial tissues and creates good, high contrast images with trivial light dispersal. In addition, small datasets of corneal images have been used in the assessment of most of these presented methods. In this work the literature review is organized as follows: corneal sub-basal epithelium analysis is reviewed in Section 2.2. Corneal nerve registration techniques are presented in Section 2.3. The review of corneal endothelium cell analysis is provided in Section 2.4. The knowledge gaps are presented in Section 2.5. Section 2.6 is a short summary.

### 2.2 Corneal Sub-Basal Epithelium Nerve Analysis

The work proposed in (Ferreira, Morgado and Silva, 2010) is a phase symmetry-based system for the segmentation of corneal nerves of images acquired by corneal confocal microscopy. Firstly, the contrast of the nerves is



increased and the noise is reduced, using contrast equalization, a phase symmetry-based approach and histogram processing. This is followed by a region growing, a nerve reconstruction technique to join the disconnected nerves. Small, isolated segments are discarded. Finally, two morphometric parameters are measured nerve tortuosity and the nerve length. The method was tested on a small dataset consisting of 15 images and achieved  $87.1\% \pm 8.1\%$  correctly segmented nerves. The authors in (Otel *et al.*, 2013) used the same algorithm as in (Ferreira, Morgado and Silva, 2010) but with a different dataset to extract a set of morphometric parameters consisting of tortuosity, density, length, width and branching measure. These were used to identify diabetic peripheral neuropathy and measure its severity. However, the authors found that the proposed nerve segmentation method did not give excellent results in extracting the clinical features. Therefore, manual segmentation with the aid of SPSS program was used to compute each morphometric parameter.

(Ruggeri, Scarpa and Grisan, 2006) proposed a corneal nerve tracing and recognition system. The system starts by normalizing the contrast and luminosity of a corneal image and then applies an averaging filter to reduce its noise. A tracking procedure is then applied starting from a set of automatically defined seed points. In the final stage, fuzzy c-mean clustering is applied to classify the pixels as “nerve” or “non-nerve” pixels. The system performance was tested on 12 images and the execution time was 4-5 minutes per image. No further details on how they measured execution time were given. The results showed that the performance of the system could be affected by the presence of cells in images. Epithelium cells could be incorrectly identified as segments of nerves. (Poletti and Ruggeri, 2013) presented an algorithm for corneal nerve

recognition based on an automatically identified set of seed points lying all over the image. The nerves are traced by connecting the seed points using their minimum cost paths. This system was tested using a dataset consisting of 30 epithelium corneal images. The algorithm achieved an average sensitivity of about 0.85, a false detection rate of 0.05 and an execution time of 25 seconds per image. No further details about how the execution time was measured are available.

(Ferreira, Morgado and Silva, 2012) developed an automatic segmentation and morphometric analysis system for sub-basal corneal nerves images obtained by using corneal confocal microscopy. The system starts by enhancing the image contrast and reducing the noise using contrast equalization and a histogram procedure, respectively. To identify the nerve structures, a phase symmetry-based algorithm using a wavelet transform filter is used. Then, a nerve reconstruction process is implemented using manually selected sets of seed points, followed by a sequence of morphological operations to discard small segments. The system failed to recognize 5.3% of the nerves correctly. (Scarpa, Grisan and Ruggeri, 2008a) presented an algorithm for detecting corneal nerves in CCM images. Firstly, the algorithm starts by enhancing the luminosity and contrast of the corneal images by employing an equalization technique. This is followed by an automatic procedure to identify a set of seed points all over the input image to be used as starting points to detect each nerve in the image. The algorithm was tested on a dataset consisting of 90 images of control and patient subjects. It correctly recognized 80.4% and 83.8% of nerve length, compared with the manually traced nerves length, in control and patient subjects, respectively. (Scarpa *et*

*al.*, 2011) presented an automatic algorithm to calculate and classify the tortuosity of corneal nerves using a dataset containing 30 corneal sub-basal nerve images. The proposed algorithm is based on the tracing and recognition system for corneal nerves in (Scarpa, Grisan and Ruggeri, 2008a). Nerve tortuosity was calculated using an algorithm based on the number of twists in the curvature sign and on the amplitude. The results obtained were compared against the manual evaluation performed by an expert. Only 2 classification errors in 30 images were made by the proposed algorithm. An automatic analysis and classification system for detecting nerves in confocal microscopy corneal images based on a multi-scale dual model detection algorithm was presented in (Dabbah *et al.*, 2011). Feature vectors were generated from this dual-model detection to be used in the classification stage, which is based on the Random Forest (RF) and Neural Networks (NN) to classify the pixels as nerve or non-nerve pixels. The performance of the proposed system was evaluated using a database consisting of 521 CCM images, which is a subset of a database used in the work presented in this PhD Thesis. The highest sensitivity and specificity using the proposed system were achieved at an EER of 15.44%. The work reported in (Guimar *et al.*, 2014) presents an automatic system to trace sub-basal plexus nerves in images which are acquired by CCM. First, a top-hat Morphological operation is used to enhance the image's contrast. Next, a Log-Gabor filter is applied to enhance the corneal nerve structure. This is followed by hysteresis thresholding to obtain candidate nerve segments that are input to a Support Vector Machine (SVM) to distinguish between nerve and non-nerve segments. The system performance was tested on 246 images and achieved an average sensitivity of  $0.88 \pm 0.06$ .

(Dabbah *et al.*, 2009) developed two techniques for nerve detection. The first technique was based on a linear operator, which was devised originally for asbestos fibres. This technique exploits the line-like structure of the nerve. The second technique is based on Gabor wavelet filtering to detect nerve fibres in the corneal image. Then a thresholding operation is applied on both methods to obtain binary images followed by thinning to provide a skeleton image with a tolerance of about  $\pm 3.1\mu\text{m}$  in nerve location. The two proposed techniques were tested on only 12 CCM images, which cannot be considered enough to give a clear indication of the performance of the proposed techniques. A supervised learning algorithm to classify CCM images based on manually traced tortuosity of the nerves was introduced in (Annunziata *et al.*, 2014). The method was applied to 100 corneal nerve images and tortuosity was classified into four classes (normal, mild, high and severe) by three ophthalmologists. Curvature and number of inflection points are used in the feature vector for the proposed supervised-learning system. In this system, a training phase is needed and the performances of the proposed system were tested on unseen CCM images by employing 20 fold cross-validation procedure.

### **2.3 Corneal Nerve Registration Techniques**

It is worth mentioning, that over the last few years, only a very limited number of practical medical image registration techniques of corneal confocal images have been proposed: (Elbita *et al.*, 2014) proposed an automatic system to produce a 3D visualization from a sequence of 2D corneal images taken from different layers. A comparison study between the use of speeded-up robust features (SURF) and scale invariant feature transform (SIFT) based

technique was done to evaluate their performance in overlaying a sequence of CCM images that differ in their displacement and illumination conditions. (Scarpa, Fiorin and Ruggeri, 2007) proposed an image registration algorithm based on normalized correlation to create a 3D model of the cornea using a sequence of CCM images from epithelium to endothelium. A method of registration based on normalized correlation is used on each image to take account of the normal movements of the eye during the acquisition which causes shifts in the sequence of images to take place. A stack of 2D images is reconstructed allowing for shifts directions along x, y, and z. The data missing is reconstructed using lines from adjacent images. The registration algorithm is affected by large displacements along the z-direction and the quality of CCM images to be registered. (Ito *et al.*, 2008) proposed a medical image registration method using Phase-Only Correlation (POC) to overlay two dental radiograph images. The method searches for corresponding points between two dental images using POC and corrects non-linear distortion based on a Thin-Plate Spline (TPS) technique. Experimental evaluation of the proposed algorithm indicates efficient performance even when the radiograph is distorted. More proposed medical image registration techniques can be found in (Oliveira and Tavares, 2014; Tang and Chen, 2012).

## **2.4 Corneal Endothelium Cells Analysis**

The work described in (Foracchia and Ruggeri, 2000) proposed a corneal endothelial cells segmentation approach based on a neural network architecture whose weights parameters (numerical filters) were specifically prepared for a border detection problem and obtained from a Boundary Contour

System (BCS). The “expert correction” approach was proposed to recover missing boundaries and tentative splitting or merging of cell bodies. This algorithm also used endothelial images collected from 3 different ophthalmic instruments with no information given about these instruments. In (Ruggeri, Grisan and Jaroszewski, 2005) a fully automated algorithm is presented for estimating endothelial cell density based on extracting the spatial frequencies present in digital endothelial images using a 2D-Discrete Fourier Transform (DFT) approach. The frequency information obtained from a circular band in the 2D-DFT of the endothelial images contains information related to the endothelial cell density. The performance was evaluated on 100 corneal endothelial images obtained by following the same procedures usually employed at the Berlin Cornea Bank. The endothelial images of these corneas were acquired using an inverse phase contrast microscope. The mean difference between automated and manual densities was 14 (cells/mm<sup>2</sup>), with a standard deviation of 119 (cells/mm<sup>2</sup>) and the running time was (1-2) seconds per image. An approach to derive the density of endothelial cells without determining the cell boundaries was proposed in (Grisan *et al.*, 2005) and assumed an approximately regular tessellation of hexagonal shapes. The approach calculated the inverse transpose of a matrix (aka basis) producing this cellular lattice, which is used to estimate the cell density. Due to the different sizes and spatial orientations of endothelial cells throughout the image, the basis matrix could differ significantly from one region to another and a local estimation is performed to reduce the effects of this variability. The performance of this approach was evaluated on a set of 21 corneal endothelial images captured using an inverse phase-contrast microscope in the Berlin corneal bank. The mean difference between the

manual and automated endothelial cell densities was -0.1% (6.5% for absolute differences).

(Foracchia and Ruggeri, 2007) have presented a new automatic detection and analysis approach based on a set of single cell boundary models, which statistically describe individual endothelial cells in terms of a priori shape information and a-posteriori image representation. Each cell was individually determined (by Maximum Posteriori estimation) in an image given a starting point and a Simulated Annealing (SA) as an optimization algorithm. While a cell field is estimated, further information is introduced and the overall model identification is improved by using the interaction between cell models. The results show an improvement in the detection of cell contours of specular microscope images. (Hiroyasu *et al.*, 2013) proposed a corneal endothelial cell segmentation system based on constructing a tree-structural image-processing filter, which can be applied to images of regions with different statistics. This system produces two types of nodes (e.g., one type represents well-known image-processing filters and the second represents conditional branches); their combination is optimized using genetic programming (GP). Experiments were undertaken on only two corneal endothelial images captured using a phase-contrast microscope.

(Scarpa and Ruggeri, 2015) proposed a segmentation system identifying endothelial cell boundaries based on a genetic algorithm technique. The operation of the genetic algorithm is mainly dependent on combining information about the model regularity of endothelial cell appearance with the intensity of the actual pixels in the corneal image. Experiments on 15 corneal endothelial images captured with a specular endothelial microscope were

achieved by comparing with ground truth acquired from manually drawn endothelial cell boundaries. The average difference between the manual and automated approach was 4%, and the maximum difference was lower than 7%.

(Poletti and Ruggeri, 2014) have also presented an analysis method based on a supervised classification system for endothelial cell segmentation. This method was used to extract the cell boundary polygon in terms of its three elements: vertices, sides and body, employing a multi-scale approach with 2D matched filters. In particular, three kernels were prepared to extract the three endothelial cell components' signatures. These components' signatures were used as features to train Support Vector Machine (SVM) classifier, to provide the final endothelial cell segmentation. The performance of this method was evaluated on a set of 20 images acquired by In Vivo specular microscopy and the running time was 5 to 10 seconds per image. Two approaches to analyze and quantify corneal endothelial cells captured by In Vivo white light slit-scanning confocal microscopy were presented by (Selig *et al.*, 2015). The first approach depends on a spatial frequency spectrum analysis approach to evaluate the Endothelial Cell Density (ECD). In the second approach, endothelial cells are automatically segmented by employing a stochastic watershed approach after randomly placing the seeds over the whole image. Due to noise in the input image, which causes over-segmentation, a smoothing filter with a Gaussian kernel and H-minima transform was applied before applying the stochastic watershed approach to estimate endothelial cell density, polymegathism and pleomorphism. However, in some cases, an operator interaction is required to correct the final segmented results, which can take approximately 30 seconds and altogether 4 minutes are required to estimate the



cell density, limiting real-time application in a clinic. The performance of the two algorithms was evaluated on a set of 52 corneal endothelial images captured from 23 patients using a white-light slit-scanning confocal microscope and compared with the NAVIS software.

(Sharif *et al.*, 2015) developed a hybrid model for analyzing confocal endothelial images based on a combination of Active Contour Model (ACM) of the Snake (S) model and the Particle Swarm Optimization (S-PSO) approach. Firstly, a pre-processing procedure is employed using DFT combined with a Band-pass Butterworth filter to enhance the quality and reduce the noise level of the input image. Then, boundaries of the corneal endothelial cells are traced using the (S-PSO) approach. Results from 11 abnormal confocal endothelial images were compared with manual and two other approaches based on morphological operations. The mean differences between manual and automated cell densities were 5%, 7% and 13%, respectively.

## **2.5 Current Challenges and Knowledge Gaps**

Through these surveys of the previous research on cornea epithelium nerve analysis techniques, cornea nerve registration techniques and cornea endothelium cells analysis techniques it is clear that there is a significant need for an improved methodology to quantify corneal nerve and cell morphology. Firstly, most of the methods presented are based on images from a specular microscope, which is excellent for imaging the central cornea. A specular microscope provides high contrast between the different cornea tissues and creates good, high contrast images with trivial light dispersal. Despite increasing use of In Vivo corneal confocal microscopy for both clinical and research

purposes, little research has been undertaken to develop a fast and fully-automated segmentation algorithm for quantifying corneal endothelial images acquired with In Vivo corneal confocal microscopy.

In this state, this makes it impossible to compare our results with other studies. Secondly, most of the existing methods are based on defining a set of seed points all over the image, whether manually or automatically. Thirdly, relatively small datasets of corneal confocal microscopy images have been employed in the assessment of most of these presented methods, which are insufficient to reliably reveal the real world performance of the proposed approaches. Moreover, the processing time for tracing all the nerves or determine each cell in a single image can take more than one minute in some cases. In this PhD Thesis to overcome these deficiencies, for clinical diagnostic use for epithelium and endothelium cornea layers, an accurate, fast and fully automatic corneal analysis system is proposed.

## **2.6 Summary**

In this work, a brief literature review of previous research related to cornea epithelium nerve and endothelium cell images is presented. A number of limitations have been highlighted, as discussed in the previous section. In this PhD Thesis, three databases are used to assess the efficiency of the proposed systems. The first consists of a total of 498 nerve images from 20 subjects (Otel *et al.*, 2013) and the number of images per subject vary between 12 and 38. In this dataset, 12 subjects had diabetes and 8 had no diabetes. The second database (Chen *et al.*, 2015a) consists of a total of 919 nerve images where 445 images are from 84 control subjects and the remaining 350 images are

from 63 diabetic patients without neuropathy, and 124 images are from 25 patients with neuropathy. The third database, a total of 80 images of corneal endothelial cells was acquired using a laser CCM (Tavakoli and Malik, 2011). These images were divided into two databases, each containing 40 images. There is no previous work on this database.

## Chapter 3

# Cornea Sub-Basal Epithelium Analysis

### 3.1 Introduction

The cornea consists of five layers: the Epithelium, Bowman, the Stroma, Decement's membrane and the Endothelium layer, as shown in (Chapter 1, Figure 1.2) (Patel *et al.*, 2002). It contains sensory and autonomic nerves located at the interface between the Bowman's layer and the basal epithelium. Corneal Confocal Microscopy (CCM) is a rapid non-invasive In Vivo clinical technique for capturing images of the different corneal layers (Jalbert *et al.*, 2003). Morphological alterations in the epithelium, stroma and endothelium provide insights into a variety of corneal diseases (Bitirgen *et al.*, 2013; Bitirgen *et al.*, 2015) and assessment of the effects of wearing contact lenses (Patel *et al.*, 2002), LASIK or PRK (Moilanen *et al.*, 2003), fungal keratitis (Kurbanyan *et al.*, 2012), corneal transplantation (Niederer *et al.*, 2007) or conditions such as keratoconus (Patel and McGhee, 2006; Simo Mannion, Tromans and O'Donnell, 2005). CCM has also been used in the assessment of peripheral neuropathies (Chen *et al.*, 2015; Alam *et al.*, 2015). The development of automated imaging algorithms for the processing of CCM images is a necessary accompaniment to such work. Diabetes is the main cause of neuropathy complications and in the present work patients with a known history of cancer, chemotherapy, alcoholism, celiac disease or a deficiency of vitamin B12 or folate, abnormality in ANA or immunoglobulins were excluded to remove other causes of peripheral neuropathy from the input data. Diabetes can result

in nerve disorders and nerve damage that affect various parts of the human body, such as the digestive tract and the cardiovascular system (Dehghani *et al.*, 2014; Pacaud *et al.*, 2015). Quantifying corneal nerve morphology has been shown to have promise as an imaging biomarker for early diagnosis of sub-clinical diabetic neuropathy (Quattrini *et al.*, 2007; Azmi *et al.*, 2015) and to have value in predicting those who develop clinical neuropathy (Lovblom *et al.*, 2015; Pritchard *et al.*, 2015) and response to therapy (Tavakoli *et al.*, 2013). Presently, most analysis methods of the corneal nerves are based on wearisome and are very time consuming manual tracing programs. As a result, the information obtained on the clinical parameters quantification is subjective and can have limited reproducibility (Petropoulos *et al.*, 2013). A fully automatic and real-time system for tracing sub-basal nerves and extracting clinically meaningful parameters is required. Such a system would reliably and efficiently assess nerve pathology in diabetic patients and provide an objective means for diagnostic and staging purposes (Ferreira, Morgado and Silva, 2010; Dabbah *et al.*, 2011; Petropoulos *et al.*, 2014). However, in order to build an efficient and robust system for segmenting the sub-basal nerves in corneal images, a number of issues need to be taken into account, including the visual contrast of nerves, the discontinuities in some nerve images, and the inconsistent intensities of corneal sub-basal images, which can all play a significant role in decreasing segmentation performance.

In this work, a robust, fully automatic segmentation and morphometric parameter quantification system for CCM images of human corneal sub-basal nerves is proposed. The segmentation part consists of three main steps. Firstly, a pre-processing step to enhance the visibility of the nerves and reduce noise

by applying anisotropic diffusion filtering (Coherence filter) and a Gaussian filter. Secondly, unwanted features such as epithelial cells and other small structures, which are not nerves, are removed from the input image by applying a number of morphological operations. Finally, an edge detection process is applied to detect all the nerves in the input image. In the quantification of morphometric parameters, a number of useful clinical features are extracted, including nerve tortuosity, nerve thickness, nerve length, nerve density and other clinical features of the nerve to aid in the early diagnosis of DPN. The main contribution of this work is developing an objective and fully automatic system that can be used for tracing the sub-basal nerves in corneal images and extracting meaningful clinical features for early diagnosis of diabetic neuropathy. Moreover, an efficient algorithm is proposed for connecting discontinuous nerves without any manual intervention, which can play a significant role in calculating helpful and meaningful clinical features, such as nerve tortuosity and nerve length that mainly depend on the nerve structure. Finally, an efficient and accurate nerve thickness algorithm, without any manual intervention, is also proposed.

This chapter is organized as follows: Section 3.2 includes descriptions of the proposed methodology of corneal sub-basal nerve segmentation and quantification system with the materials used. The experimental results are presented in Section 3.3. Finally, a summary is stated in the last section.

### 3.2 The Proposed Methodology

The proposed automatic nerve evaluation system is divided into two main stages: the nerve segmentation stage and the morphometric parameters quantification stage. The segmentation stage consists of three main steps: a pre-processing step to enhance the images; a morphological operations step to remove unwanted objects and an edge detection step to detect the nerves. In the morphometric parameter quantification stage, clinically useful nerve features (e.g., thickness, tortuosity, length, density, etc.) are extracted and presented in a quantitative format. A block diagram of the proposed system is shown in Figure 3.1.

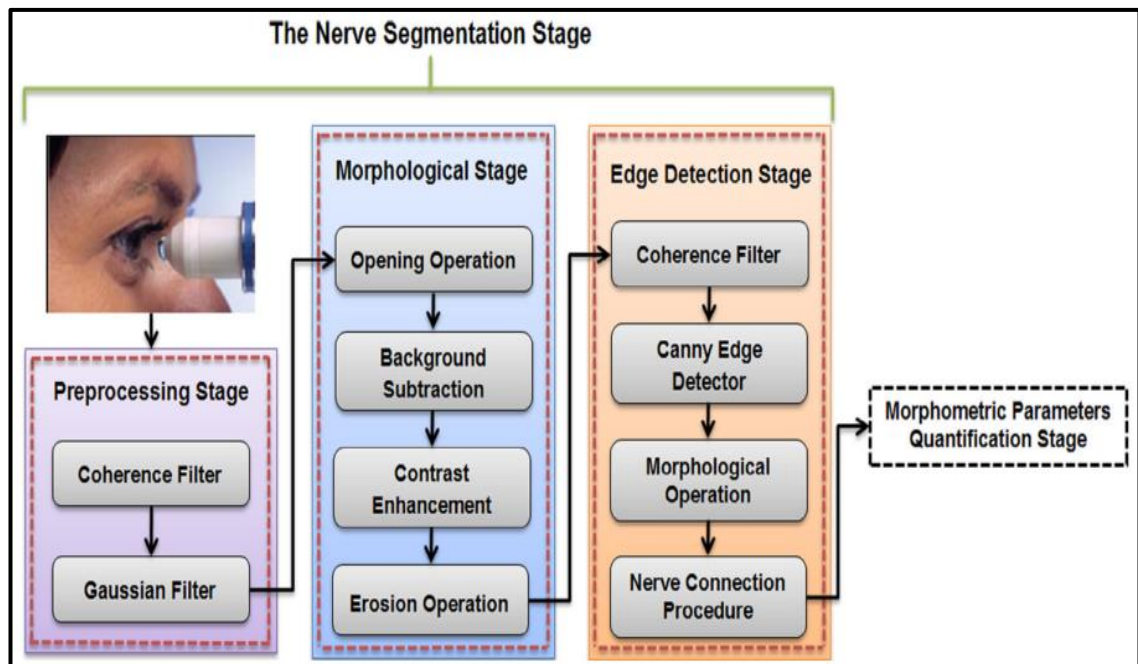


**Figure 3.1:** Overview of the automatic proposed corneal nerve segmentation and quantification system.

### 3.2.1 Data Used

Two databases were used to assess the efficiency of the proposed corneal nerve system. The first consists of a total of 498 images from 20 subjects (Otel *et al.*, 2013) and the number of images per subject varies between 12 and 38 with 12 subjects had diabetes and 8 had no diabetes, and mean ages of  $(58 \pm 10)$  years and  $(54 \pm 7)$  years, respectively. Diabetic patients were classified into 3 groups: 4 with No neuropathy (mean age  $53 \pm 11$  years), 5 with Mild Neuropathy (mean age  $58 \pm 9$  years) and 3 with Moderate neuropathy (mean age  $60 \pm 9$  years). Images (samples are shown in Figure 3.2) were acquired using a Heidelberg Retinal Tomograph equipped with a Cornea Rostock Module (HRT-CRM: Heidelberg Engineering, Heidelberg, Germany). The images were saved in JPEG compressed format with a size of  $(384 \times 384)$  pixels covering a  $(400 \times 400) \mu\text{m}^2$  frame size at an optical magnification of 63X. The second database (Chen *et al.*, 2015a) consists of a total of 919 images where 445 images are from 84 control subjects and the remaining 350 images are from 63 diabetic patients without neuropathy, and 124 images are from 25 patients with neuropathy. The CCM images were captured using a Heidelberg Retina Tomograph equipped with Rostock Cornea Module (HRT-III). The images have a size of  $(384 \times 384)$  pixels with a pixel size of  $1.0417 \mu\text{m}$  and 8-bit grey levels and were saved in BMP format.



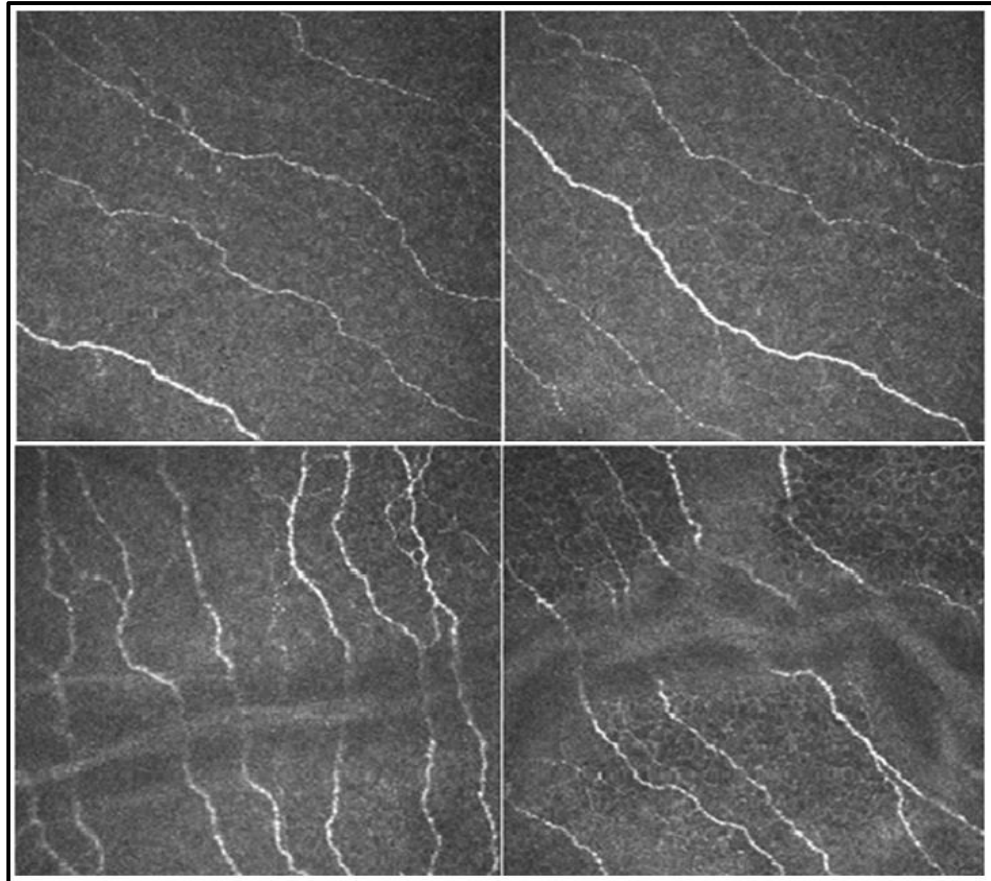


**Figure 3.2:** Images from the dataset used. The first two images from the top are from healthy control subjects, while the bottom two images are from diabetic patients.

### 3.2.2 Pre-processing Stage

The pre-processing stage aims at addressing a number of issues related to enhancing and improving the quality of the corneal images. Movements of the eye during the image acquisition process can cause a motion blurring effect and those CCM images of adjacent layers to be displaced laterally with respect to each other. In addition, the spherical shape of the cornea layer leads to unequal distribution of lighting cornea areas during the acquisition process. Image acquisition process can also lead to the emergence of some observed artefacts.

In order to address all the above problems, coherence filtering (anisotropic diffusion filtering) and Gaussian filtering have been used to enhance edges in the corneal image and reduce noise while preserving nerve structure. In this stage, a tensor form was used to adjust the diffusion to the underlying corneal image structure and reduce the noise along the edges of the nerves, rather than using a scalar diffusion constant. In general, the tensor can be built in many ways. Either Coherence-Enhancing Diffusion (CED) for enhancing line-like textures in the image or Edge-Enhancing Diffusion (EED) to reduce the noise while enhancing edges is used (Mendrik *et al.*, 2009; Weickert, 1998). In this work, a Hybrid Diffusion filter with a Continuous Switch (HDCS) has been used, combining the CED and EED algorithms (Mendrik *et al.*, 2009). The HDCS is an important approach for nerve enhancement, because the corneal image contains tubular and planar image structures. Therefore, if the structure of the image is tubular, the HDCS turns into CED and if it is planar, the HDCS turns into EED. In addition, the standard discretization scheme, non-negative discretization scheme and the optimized discretization scheme have been used as diffusion schemes.

### 3.2.2.1 Diffusion Filtering

Dirk-Jan Kroon used anisotropic diffusion filtering (Kroon, Slump and Maal, 2010) as an iterative filtering approach for edge-preserving smoothing in medical images, which can also be used to enhance the edges in a corneal image, reduce noise and preserve the nerve structure. The structure of the local image required in diffusion filtering is described using a structure tensor  $J(\nabla I)$ ,

(also referred to as a "second-moment matrix") given by Eq.3.1. More details can be found in (You *et al.*, 1996).

$$J(\nabla I) = K_j * (\nabla I \cdot \nabla I^T) \quad (3.1)$$

Here,  $\nabla$  is the del or nabla operator,  $\nabla I$  is the image gradient and  $K_j$  denotes a Gaussian kernel and  $*$  is the convolution operator. The local orientation of the image is obtained from the eigen decomposition of the structure tensor:

$$J(\nabla I) = [V_1 \ V_2] \cdot \begin{bmatrix} \mu_1 & 0 \\ 0 & \mu_2 \end{bmatrix} \cdot \begin{bmatrix} V_1^T \\ V_2^T \end{bmatrix} \quad (3.2)$$

where  $V_1, V_2$  are eigenvectors that give the orientation of the local image with  $V_1 = [v_{11} \ v_{12}]^T$ , etc., and the eigenvalues, with  $\mu_1 \geq \mu_2$  can be used to describe the average contrast in these directions. This structure tensor is used to define the diffusion tensor  $D$ , which can be defined as follows (Weickert and Scharr, 2002):

$$\frac{\partial u}{\partial t} = \nabla \cdot (D \nabla u) \quad (3.3)$$

where  $u(u = u(t, x, y))$  is the image,  $t$  the diffusion time and  $x, y$  are the pixel coordinates and  $\nabla u$  is the gradient of the image  $u$ . In general, the diffusion tensor  $D$  has the same eigenvectors set as given by the structure tensor:

$$D = \begin{bmatrix} D_{11} & D_{12} \\ D_{12} & D_{22} \end{bmatrix} \quad \text{with } D_{ij} = \sum_{n=1..2} \lambda_n v_{ni} v_{nj} \quad (3.4)$$

In Eq.3.2 and Eq.3.4, It has been noticed that the symmetry between  $\lambda_1, \lambda_2$ , which are the eigenvalues of the diffusion tensor and the structure tensor. Due to the nature of the corneal image, which consists of planar and tubular structures, the HDCS is used in this work.

Depending on the local corneal image structure, the HDCS switches between CED and EED, the former if the local structure is tubular, or the latter if the local structure is planar.

### 3.2.2.2 Hybrid Diffusion With Continuous Switch (HDCS)

In general, medical images have complex structures with varying level of intensities, shapes and sizes. If the EED is applied to a corneal confocal image, it filters the noise and enhances the edges and curves of the image, but blurs small structures. On the other hand, if the CED is applied, it enhances line-like structures such as nerves and preserves small structures (Mendrik *et al.*, 2009). Therefore, a new filter combining the advantages of both EED and CED could lead to better results. As mentioned before, a structure tensor is used to construct the diffusion tensors for the EED and CED.

(Frangakis and Hegerl, 2001) have proposed a discrete switch form to integrate EED and CED based on the difference ( $\mu_1 - \mu_2$ ) of the structure tensor eigenvalues. However, the proposed filter cannot be applied properly in some situations. On the other hand, (Mendrik *et al.*, 2009) have proposed a Hybrid Diffusion with Continuous Switch (HDCS) by continuously combining the intermediate geometries of the EED and CED. The eigenvalues of the proposed hybrid diffusion tensor ( $\lambda_{h_i}$ ) are adjusted to be a linear combination of the eigenvalues of the EED ( $\lambda_{e_i}$ ) and CED ( $\lambda_{c_i}$ ), which are given as follows:

$$(\lambda_{h_i}) = (1 - \varepsilon) \cdot (\lambda_{c_i}) + \varepsilon \cdot (\lambda_{e_i}) \quad (3.5)$$

where ( $\varepsilon$ ) refers to the EED fraction which switches between using the eigenvalues of the EED eigenvalue ( $\varepsilon \rightarrow 1$ ) or the CED eigenvalue ( $\varepsilon \rightarrow 0$ ) diffusion tensor. In this work, Hybrid Diffusion with Continuous Switch

(HDGS) is proposed to enhance the structure of the corneal sub-basal nerves and reduce the unwanted noise. Therefore, the CED should be applied first, to preserve small structures and followed by EED, to reduce the noise isotropically (Mendrik *et al.*, 2009).

$\frac{b_{i-1,j} - b_{i,j+1}}{4}$	$\frac{c_{i,j+1} + c_{i,j}}{2}$	$\frac{b_{i+1,j} + b_{i,j+1}}{4}$
$\frac{a_{i-1,j} + a_{i,j}}{2}$	$-\frac{a_{i-1,j} + 2a_{i,j} + a_{i+1,j}}{2} + \frac{c_{i,j-1} + 2c_{i,j} + c_{i,j+1}}{2}$	$\frac{a_{i+1,j} + a_{i,j}}{2}$
$\frac{b_{i-1,j} + b_{i,j-1}}{4}$	$\frac{c_{i,j-1} + c_{i,j}}{2}$	$\frac{b_{i+1,j} - b_{i,j-1}}{4}$

(a)

$\frac{ b_{i-1,j+1}  - b_{i-1,j+1}}{4}$ + $\frac{ b_{i,j}  - b_{i,j}}{4}$	$\frac{c_{i,j+1} + c_{i,j}}{2} - \frac{ b_{i,j+1}  +  b_{i,j} }{2}$	$\frac{ b_{i+1,j+1}  + b_{i+1,j+1}}{4}$ + $\frac{ b_{i,j}  + b_{i,j}}{4}$
$\frac{a_{i-1,j} + a_{i,j}}{2}$ - $\frac{ b_{i-1,j}  +  b_{i,j} }{2}$	$-\frac{a_{i-1,j} + 2a_{i,j} + a_{i+1,j}}{2}$ - $\frac{ b_{i-1,j+1}  - b_{i-1,j+1} +  b_{i+1,j+1}  + b_{i+1,j+1}}{4}$ - $\frac{ b_{i-1,j-1}  + b_{i-1,j-1} +  b_{i+1,j-1}  - b_{i+1,j-1}}{4}$ + $\frac{ b_{i-1,j}  +  b_{i+1,j}  +  b_{i,j-1}  +  b_{i,j-1}  + 2 b_{i,j} }{2}$ - $\frac{c_{i,j-1} + 2c_{i,j} + c_{i,j+1}}{2}$	$\frac{a_{i+1,j} + a_{i,j}}{2}$ - $\frac{ b_{i+1,j}  +  b_{i,j} }{2}$
$\frac{b_{i-1,j-1} + b_{i-1,j-1}}{4}$ + $\frac{ b_{i,j}  + b_{i,j}}{4}$	$\frac{c_{i,j-1} + c_{i,j}}{2} - \frac{ b_{i,j-1}  +  b_{i,j} }{2}$	$\frac{ b_{i+1,j-1}  - b_{i+1,j-1}}{4}$ + $\frac{ b_{i,j}  - b_{i,j}}{4}$

(b)

**Figure 3.3:** Notations for (a) the standard discretization scheme and (b) the non-negative discretization scheme.

### 3.2.2.3 Diffusion Schemes

The diffusion tensor equation (Eq.3.3) can be solved numerically using finite differences methods, using central differences instead of the spatial differences, and a forward difference approximation to discretize  $\partial u/\partial t$

(Frangakis and Hegerl, 2001), as shown in Eq.3.6. The result is the basic structure of an explicit scheme, which can be used to compute the values at a new time level from the previous level as shown in Eq.3.7:

$$\frac{\mathbf{u}_{i,j}^{k+1} - \mathbf{u}_{i,j}^k}{\mathcal{T}} = \mathbf{A}_{i,j}^k * \mathbf{u}_{i,j}^k \quad (3.6)$$

$$\mathbf{u}_{i,j}^{k+1} = (\mathbf{I} + \mathcal{T}\mathbf{A}_{i,j}^k) * \mathbf{u}_{i,j}^k \quad (3.7)$$

Here,  $\mathcal{T}$  refers to the time step size and  $\mathbf{u}_{i,j}^k$  refers to the approximation of  $\mathbf{u}(\mathbf{x}, t)$  in pixel  $(i, j)$  at time  $k_{\mathcal{T}}$ . The notation  $\mathbf{A}_{i,j}^k * \mathbf{u}_{i,j}^k$  is a discretization of the diffusion tensor expression. In this work, three schemes have been investigated. These are the standard discretization scheme (Fritz, 2006), the non-negative discretization scheme (Weickert, 1998) and the optimized scheme (Kroon, Slump and Maal, 2010). Figure 3.3 (a) and (b) show the stencil representations of the standard discretization and the non-negative discretization for  $\mathbf{A}_{i,j}^k$ , assuming that the pixels have length **1** in both directions. Here  $\mathbf{a}$ ,  $\mathbf{b}$  and  $\mathbf{c}$  are the output of the diffusion tensor  $\mathbf{D}$ . The last scheme is the optimized scheme for rotational invariant structures proposed by Dirk-Jan et al, for which more details to optimize the image derivatives in a numerical way can be found in (Kroon, Slump and Maal, 2010). In this work, the coherence filter has been applied over four iterations, three in the pre-processing stage and one at the beginning of the edge detection stage. Each has been executed using a different diffusion scheme trying to enhance the structure of the corneal nerve without losing important information. In the pre-processing stage, the parameters have been set empirically, as follows: Diffusion Time = 2, Diffusion Time Step size = 0.5,  $\sigma = 8$ ,  $\mathbf{D} = \text{HDCS}$ , with the diffusion scheme set to

standard discretization in the first iteration and set to non-negative discretization in the second and third iterations. In fact, all the parameter values in this step were chosen after an intensive empirical study investigating their influence on corneal images of different degrees of resolution. For example, the temporal step was set to be equal to 2, given that for lower values than 2, the produced image still has some noise, which results in detecting unwanted segments (e.g. small cells). Whereas for higher values than 2, a highly smoothed image will be produced with a large number of discontinues nerves. An example of a filtered image is shown in Figure 3.4 (b). The output of the coherence filter is smoothed further using a 2D-Gaussian filter, to reduce false artefacts, obtain a better corneal image for the edge detection stage and enhance the corneal image quality, with the result shown in Figure 3.4(c). The Gaussian filter (Haddad and Akansu, 1991) modifies the input signal through convolution with a 2D-Gaussian function defined as follows:

$$G(x, y) = \frac{1}{2\pi\sigma^2} e^{-\frac{x^2+y^2}{2\sigma^2}} \quad (3.8)$$

where  $x$  and  $y$  are the distances from the origin along the horizontal and vertical axes respectively, and  $\sigma$  (set to 2) is the standard deviation of the Gaussian distribution.

### 3.2.3 Morphological Operations Stage

The main purpose of this stage is to describe the nerve structure more accurately by removing imperfections (e.g. various types of noise that can affect the nerve's structure) and make the nerve more visible. In this stage, the opening and erosion operations are used. Morphological operations are also

used in other places in the proposed system to eliminate unwanted areas (small segments) without affecting the overall shape of the nerve. Generally, the morphological operations require two inputs, the input image that is to be processed and a structuring element (De, Chanda and Chattopadhyay, 2006). Dilation and erosion operations are the basic operations used in most morphological operations and are defined as follows:

$$f \oplus B = \max_{u,v} (f_{(x-u,y-v)} + B_{(u,v)}) \quad (3.9)$$

$$f \ominus B = \min_{u,v} (f_{(x+u,y+v)} - B_{(u,v)}) \quad (3.10)$$

where  $f$  is a greyscale image,  $B$  is a structuring element.  $f \oplus B$  and  $f \ominus B$  represent a dilation and erosion, respectively. The opening and closing operations are defined in terms of the dilation and erosion operations, in Eq.3.11 and Eq.3.12, respectively:

$$f \circ B = (f \ominus B) \oplus B \quad (3.11)$$

$$f \bullet B = (f \oplus B) \ominus B \quad (3.12)$$

The values of the parameters used in this stage were selected empirically after a number of experiments were carried out using corneal sub-basal images with different levels of noise and illumination, taken into account enhancing the structure of the corneal nerve without losing important information in the whole image rather than a specific region of interest (ROI). The morphological opening operation is carried out on the image output from the Gaussian filter, using a disk-shaped structure element of 4 pixels radius, followed by a background subtraction operation to separate out foreground



objects from the background and detect the corneal nerves correctly. Then, an image contrast enhancement procedure is applied to enhance nerves visibility and to enhance the illumination uniformity of the corneal image by stretching the overall contrast of the image between two predefined lower and upper cutoffs which are empirically set to be 0.55, and 0.999, respectively. Finally, a morphological erosion operation using a structure element of 1-pixel is applied to refine the shapes of the corneal nerves, as shown in Figure 3.4 (d). Objects of 1-pixel size are discarded.

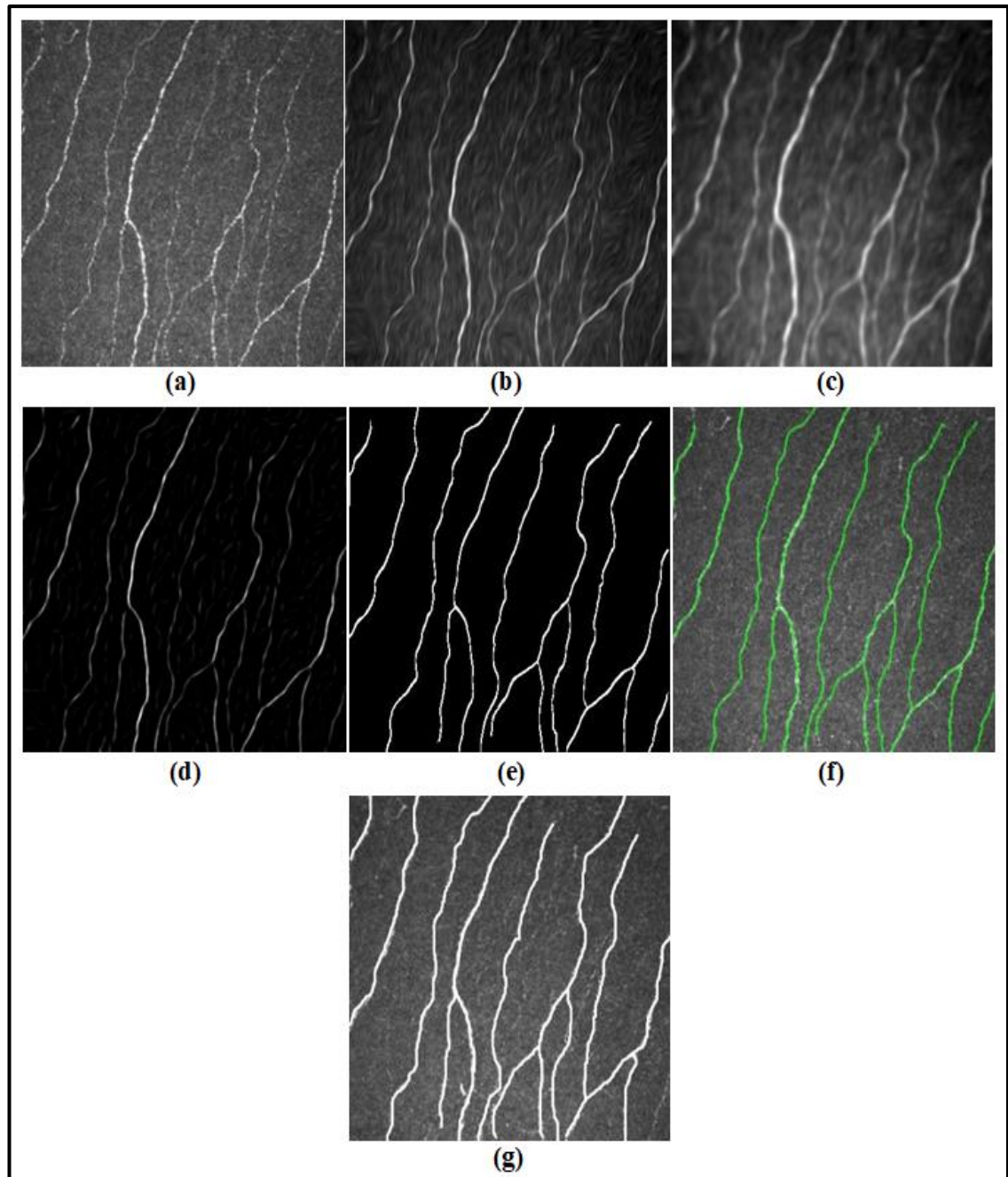


**Figure 3.4:** Corneal nerve segmentation system outputs: (a) Original corneal image, (b) Coherence filter output, (c) Gaussian filter output, (d) Morphological operations stage output, (e) Segmented image from the edge detection stage, (f) Automatically traced corneal sub-basal nerves, (g) Manually traced corneal sub-basal nerves.

### 3.2.4 Edge Detection Stage

The edge detection process is used here to preserve useful structural information about nerve boundaries and to drastically reduce unwanted areas. The main implemented approaches in edge detection stage are shown in Figure 3.5. Firstly, the coherence filter is applied again for further enhancement and removal of noise introduced by the morphological stage, which can affect the accuracy of the nerve detection in the subsequent stages. In this step, the parameters of the coherence filter have been set empirically as follows: Diffusion Time =1, Diffusion Time Step size = 0.1,  $\sigma = 8$ , D = HDCS, and the diffusion scheme = Optimized Derivative Kernels Scheme. The corneal nerves are then detected by applying a Canny edge detector (Canny, 1986); more details in Appendix A. Further refinement is required to preserve the accurate thickness of the detected nerves, to remove some noisy background pixels, and to connect discontinuities in nerves in the segmented image. A morphological dilation operation is applied firstly using two line-shaped structural elements, with lengths of **3** and angles of **90°** and **0°**, respectively. Secondly, a morphological erosion operation is applied twice using structure element of one pixel size, to refine the shapes of the detected nerves. This is followed by a candidates' selection procedure based on the properties of the connected objects in the refined image where only objects that have a total area of more than **150** pixels are retained (Figure 3.4 (e)). Then, a nerve connection procedure is applied to connect the discontinuous nerves. The gaps in nerve structures and branches appear in segmented nerves as a result of low visibility of parts of the nerves, or noise introduced into the corneal images, for example.

In the present study, a new technique has been proposed to link the discontinuous nerves correctly, which is summarized as follows:

1. Take the skeleton form of the final segmented image and determine the endpoints of each nerve segment in the segmented image.
2. Determine a possible maximum gap size between the endpoint of each disconnected nerve and neighbouring nerve. Then a binary circular region of ***radius = (maximum gap size)/2*** is placed at the endpoint of each nerve segment. If the endpoints of two nerve segments are close to each other, a straight line is drawn connecting these two segments within the area covered by the circular structure elements, as shown in Figure 3.6 (b).
3. Finally, by thinning the resultant image, the overlapped circular structure elements at the endpoints of each segment will leave behind a line of pixels linking the two endpoints of the nerve. While, the isolated endpoints are restored to their original structure, as shown in Figure 3.6 (c).

This step has a significant effect on calculating the tortuosity of nerves, because nerves' discontinuities affect the measurements of nerve length, and hence the calculated tortuosity of the nerve. The values of the parameters used in the system were selected empirically after a number of experiments were carried out using corneal sub-basal images with different levels of noise and illumination.

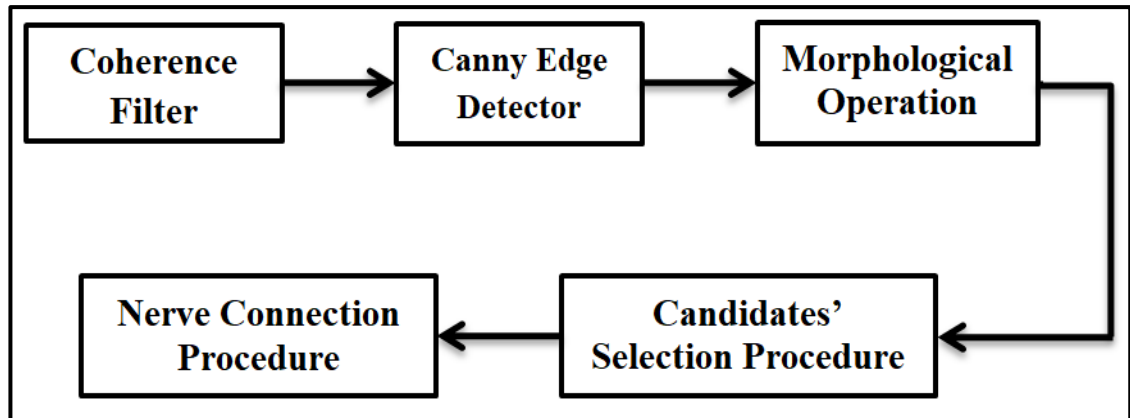


**Figure 3.5:** The main implemented approaches in the edge detection stage.

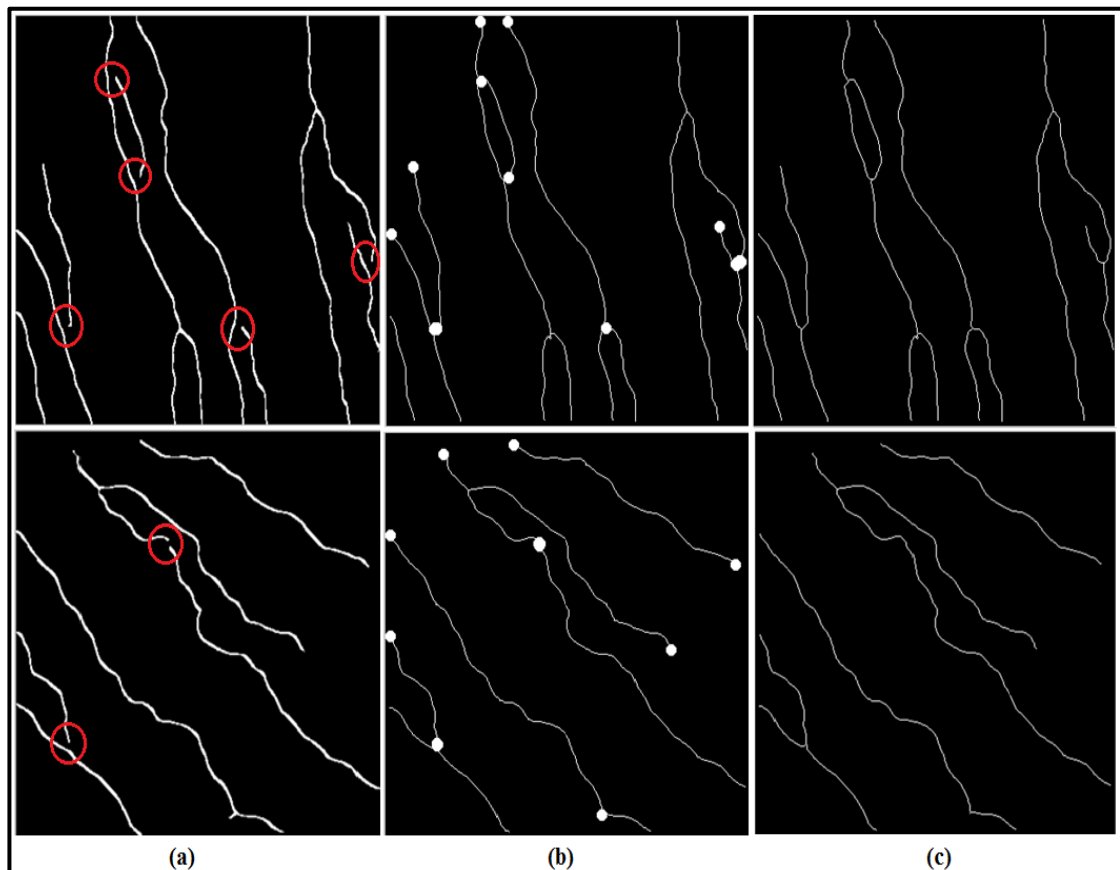


**Figure 3.6:** Nerves' connection procedure: (a) Two segmented images with disconnected nerves circled in red, (b) The binary circular structure element (white circles) drawn at the endpoints, and (c) Output image with connected nerves.

### 3.2.5 Morphometric Parameters Quantification Stage

The morphometric parameters quantification stage extracts a set of features from the automatically traced corneal sub-basal nerves in an easy and objective way. These clinical features are measured and extracted automatically so the proposed system can serve as a clinically helpful diagnostic tool for early detection and follow up of DPN from CCM images. In this work, the set of morphologically extracted features related to the cornea's state of health which is investigated include, nerve thickness, length, density and tortuosity. Additional features, such as nerve perimeter, area, and image intensity are also calculated for internal use.

#### 3.2.5.1 Nerve Length

The nerve length in ( $\mu m$ ) is calculated for each nerve segment by taking the skeleton form of the nerve and then finding the branch points in order to break up the length of nerve segment ( $S$ ) into ( $b$ ) branches as follows:

$$S = s_1 + s_2 + \dots + s_b \quad (3.13)$$

Finally, the nerve length is calculated by summing the distance between consecutive pixels in the nerve segment, as follows:

$$Nerve_{length} = \sum_{i=1}^{N-1} \sqrt{(x_{i-1} - x_i)^2 + (y_{i-1} - y_i)^2} \quad (3.14)$$

where  $N$  is the number of constituent pixels which is obtained from the nerve skeleton segment and  $(x_i, y_i)$  are the pixels coordinate in the nerve segment.

### 3.2.5.2 Nerve Density

Corneal nerve density in ( $pixels/\mu m^2$ ) is computed by dividing the sum of the nerve pixels by the image area as follows:

$$Nerve_{density} = \frac{\sum Nerve\ pixels}{ImageArea\ (\mu m^2)} \quad (3.15)$$

### 3.2.5.3 Tortuosity Coefficient

Tortuosity Coefficient (TC) is used to gain information about the average curvature changes of the nerves. In this work, the average TC is calculated for the whole image and for each corneal nerve as well. Firstly, the length of each nerve segment ( $S$ ) is calculated, as in (Section 3.2.5.1). Then, the TC index for nerve segment ( $S$ ) is then calculated as follows:

$$TC(S) = \sum_{n=1}^b s_{length}(n) / s_{straight}(n) \quad (3.16)$$

where  $s_{length}$  is the branch length and is calculated by Eq.3.14.  $s_{straight}$  refers to the straight distance between the endpoints and is calculated as follows:

$$s_{straight} = \sqrt{(x_N - x_1)^2 + (y_N - y_1)^2} \quad (3.17)$$

where  $N$  is the number of constituent pixels obtained from the nerve skeleton branch, and  $(x, y)$  are pixels coordinate in the nerve branch. Finally, the average tortuosity of the whole image is obtained by computing the average tortuosity scores derived from each nerve.

#### 3.2.5.4 Nerve Thickness

Nerve thickness in ( $\mu m$ ) is a measure of the average thickness of each corneal sub-basal nerve plexus, as shown in Figure 3.7. In this work, a new algorithm for calculating nerve thickness is proposed. The main steps of the proposed algorithm after labelling each nerve are as follows:

1. The distance transform is applied to the binary segmented image to calculate the Euclidean distance between each pixel in a nerve to the closest background pixel. In other words, for each nerve pixel, the distance from that particular pixel to the closest boundary pixel of the nerve is calculated.
2. Regarding distance values produced by the distance transform as heights in a 2D surface, the highest nerve pixels will be located along a ridge in the middle of the nerve segment. The distance values, associated with the half-way line in between the nerve segment are collected with some tolerance due to floating point arithmetic.
3. Finally, the average of all collected distances determines the half-width of the nerve segment. Hence, the full thickness can be calculated by multiplying the result obtained by 2.



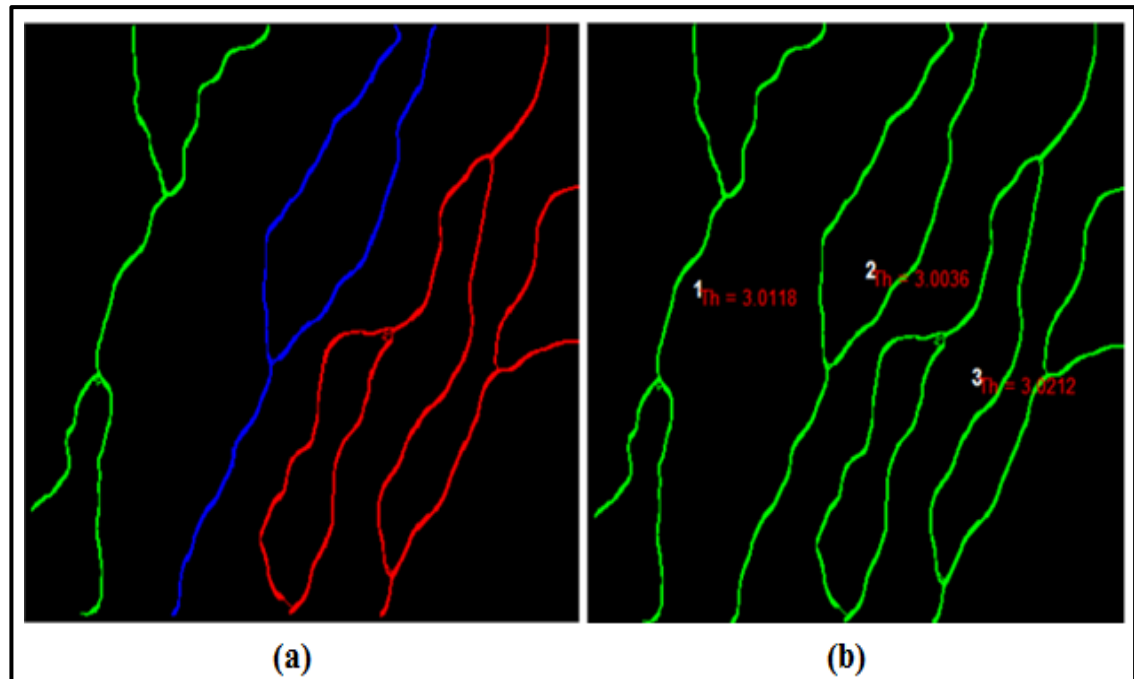


**Figure 3.7:** The thickness algorithm output: (a) Labelling of corneal nerves 1, 2 and 3 in green, blue and red, respectively, (b) Image map for the corneal nerves with their average thickness values indicated.

### 3.3 Experimental Results

The performance of the corneal sub-basal nerve segmentation system was evaluated initially on the first database containing 498 images where 238 images were taken from 8 healthy control subjects and the rest were taken from 12 diabetic patients with associated ground-truth as indicated previously in (Section 3.2.1). The evaluation is based on the calculation of the four quantitative performance measures: Structural SIMilarity Index (SSIM) (Wang *et al.*, 2004), Probabilistic Rand Index (PRI) (Kaur, Agrawal and Vig, 2012), Variation of Information (Vol) (Meil, 2007), and Global Consistency Error (GCE) (Martin *et al.*, 2001). These metrics are widely used in literature for evaluating the performance of segmentation systems and are defined as follows:

- 1. The Structural SIMilarity Index** is an image quality assessment algorithm which measures the structural similarity index between the segmented image and a ground-truth image. The measurement compares three components: luminance, contrast and structure between the segmented image ( $\mathbf{X}$ ) and the ground-truth image ( $\mathbf{Y}$ ) within a local window as follows:

$$SSIM(x, y) = \frac{(2\mu_x\mu_y + C_1)(2\sigma_{xy} + C_2)}{(\mu_x^2 + \mu_y^2 + C_1)(\sigma_x^2 + \sigma_y^2 + C_2)} \quad (3.18)$$

Here,  $(\mu_x$  and  $\mu_y)$  and  $(\sigma_x^2$  and  $\sigma_y^2)$  are the mean intensities and the standard deviations of  $\mathbf{x}$  and  $\mathbf{y}$ , respectively.  $\sigma_{xy}$  is a covariance measure for  $\mathbf{x}$  and  $\mathbf{y}$ .  $C_1=(k_1L)^2$ ,  $C_2=(k_2L)^2$  are small constants used to maintain stability when either  $(\mu_x^2 + \mu_y^2)$  or  $(\sigma_x^2 + \sigma_y^2)$  is very close to zero;  $L$  represents the dynamic range of the pixel values (255 for 8-bit grayscale images) and  $k_1, k_2 < 1$ . In this work,  $k_1$  and  $k_2$  are set to the default values **0.04** and  $L$  is set at **100**. The local measurements of  $\mu_x, \mu_y$  and  $\sigma_{xy}$  are found within a local (8x8) square window, which moves pixel by pixel over the whole image and at each step the local measurements and SSIM are computed within the local window. In this work, the overall quality measure of the entire image is obtained by calculating the mean of SSIM as follows:

$$MSSIM(X, Y) = \frac{1}{M} \sum_{i=1}^M SSIM(x_i, y_i) \quad (3.19)$$

where  $x_i$  and  $y_i$  are the image contents at the  $i$ -th local window,  $M$  is the number of local windows in the image and the MSSIM value ranges between **0** and **1**; a higher value indicates greater similarity. Moreover, the SSIM index map can be obtained to provide a measurement of the local

image quality over space, where a brighter SSIM index map indicates a better quality of segmentation, as shown in Figure 3.8.

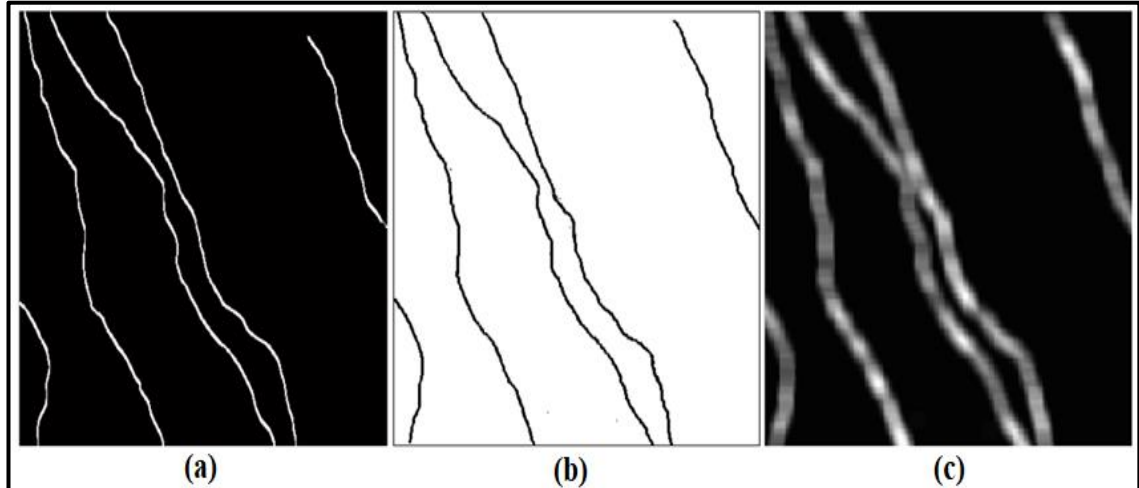


**Figure 3.8:** (a) A segmented image, (b) The binary form of the ground-truth image, (c) The SSIM index map.

2. **The Probabilistic Rand Index** calculates the number of the fraction of pairs of pixels between the segmented and the ground-truth images whose labels are harmonious, through averaging across a set of ground truth images to account for scale variation in human perception. The PRI value ranges between **0** and **1**, and a higher value indicates greater similarity.
3. **The Variation of Information metric** is a non-negative metric that measures the distance between automatic and manual segmentation in terms of the information difference between them. The Vol metric depends on entropy and mutual information to calculate the distance between two clustering. The Vol between segmented image (**S**) and the ground-truth image (**S'**) is given by Eq.3.20, where a lower Vol value points to greater similarity.

$$VoI(S, S') = H(S) + H(S') - 2I(S, S') \quad (3.20)$$

Here  $VoI$  ranges between  $0$  and  $\infty$ ,  $H$  and  $I$  represent the entropy and the mutual information, respectively. In this work, the mutual information of  $(S)$  and  $(S')$  can be calculated as follows:

$$I(S, S') = \sum_{k=1}^k \sum_{k'=1}^{k'} P(k, k') \log \frac{P(k, k')}{P(k)P(k')} \quad (3.21)$$

where  $P(k, k')$  is the joint probability distribution function of  $(S)$  and  $(S')$ , and  $P(k)$  and  $P(k')$  are the marginal probability distribution functions of  $(S)$  and  $(S')$ , respectively.

**4. The Global Consistency Error** measures the extent to which the segmented image can be viewed as a refinement of the ground-truth image. Segmentations are considered to be consistent, if the segment is a set of pixels and a pixel is in an area of refinement, if the segment  $(S)$  is a valid subset of segment  $(S')$ . In this case, the local error is equal to zero; otherwise, if there is no relationship between the two segments, the two segments overlap in an inconsistent manner. The local refinement error between two segments is calculated as follows:

$$E(S_1, S_2, p_i) = \frac{|R(S_1, p_i) \setminus R(S_2, p_i)|}{|R(S_1, p_i)|} \quad (3.22)$$

where  $\setminus$  denotes set difference,  $S_1$  and  $S_2$  are two segments. For a given pixel  $(p_i)$ , consider the segments that contain  $p_i$  in  $S_1$  and  $S_2$ . These sets of pixels are represented by  $R(S_1, p_i)$  and  $R(S_2, p_i)$ , respectively. The value of  $E(S_1, S_2, p_i)$  is zero when  $S_1$  is a refinement of  $S_2$ , but not vice versa. The

GCE between segmented image ( $\mathbf{S}$ ) and the ground-truth image ( $\mathbf{S}'$ ) is given by Eq.3.23, and ranges between  $\mathbf{0}$  and  $\mathbf{1}$ , a lower value being better.

$$GCE(\mathbf{S}, \mathbf{S}') = \frac{1}{n} \min \left\{ \sum_i E(\mathbf{S}, \mathbf{S}', p_i), \sum_i E(\mathbf{S}', \mathbf{S}, p_i) \right\} \quad (3.23)$$

The results obtained from the control subjects and the patient subjects are shown in Figure 3.9 and Figure 3.10, respectively. In these two figures, the overall average of each one of the four quantitative metrics is calculated for each subject in the dataset. The results obtained have demonstrated the robustness and effectiveness of the proposed nerve segmentation system, and the potentiality of using it as a fully automatic nerve tracing system to measure the morphological parameters for clinical diagnostic purposes, as a result of the high similarity rate obtained between the segmented images and reference images. In addition, the results obtained have demonstrated the ability of the proposed system to detect and trace the corneal nerves, effectively in real-time, with an execution time of about **7** seconds per image using a PC with Windows 8.1 operating system, a 1.80 GHz Core i5-3337U CPU and 6 GB of RAM. The system code was written in MATLAB R2010a. At each stage of the proposed system, parameter values were selected after intensive experiments on a number of corneal sub-basal images with various degrees of degradation and illumination.

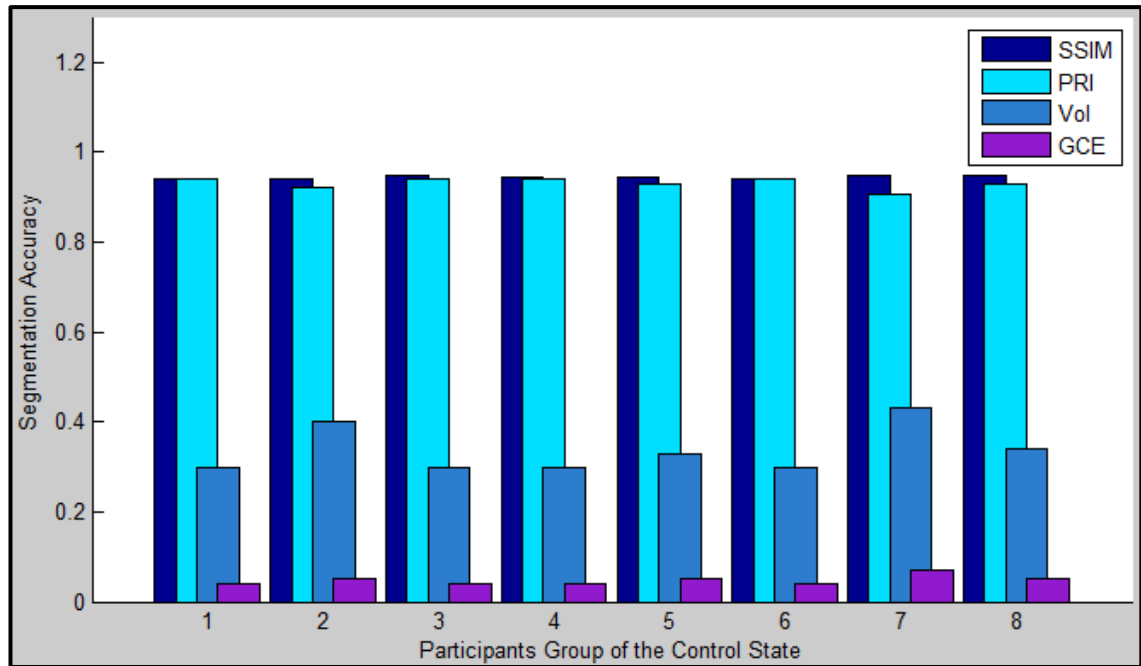


**Figure 3.9:** Descriptive statistics of the segmentation system performance of the control group of the first database, where a higher value of SSIM and PRI is better and a lower value of Vol and GCE is better.

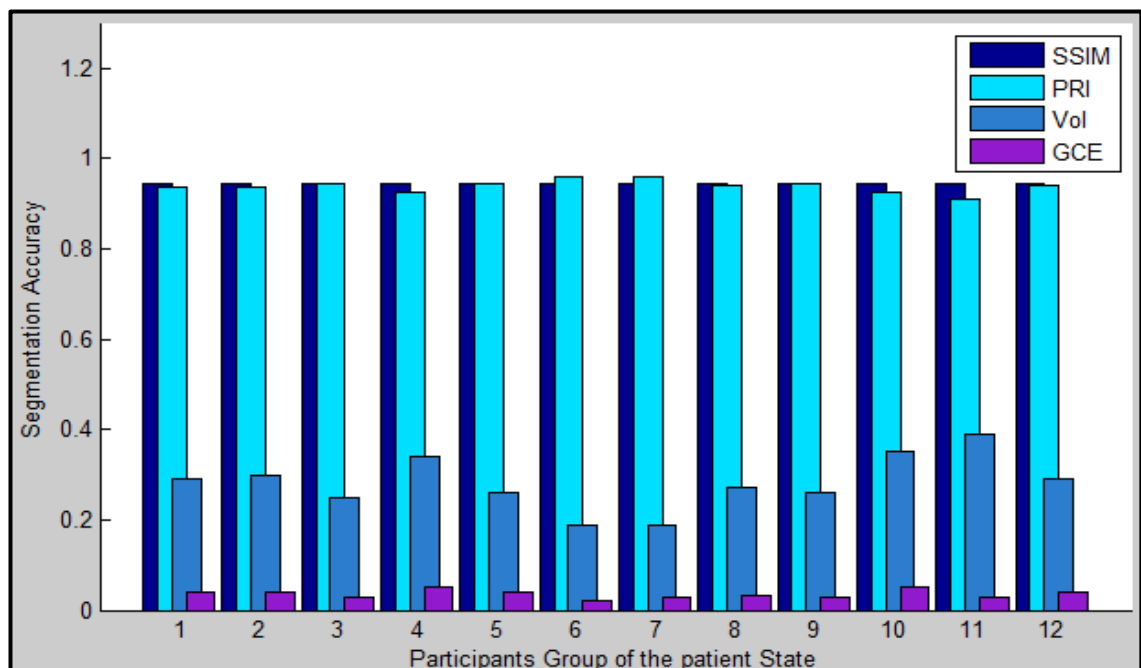


**Figure 3.10:** Descriptive statistics of the segmentation system performance of the patient group of the first database, where a higher value of SSIM and PRI is better and a lower value of Vol and GCE is better.

The overall performance of the proposed system was compared theoretically with other established automatic nerve detection systems (Dabbah *et al.*, 2010; Dabbah *et al.*, 2011), due to the unavailability of the datasets used in these works. These systems are mainly based on using single and multi-scale dual-models to detect nerve fibers. As shown in Figure 3.11, the output of the nerve detection system in (Dabbah *et al.*, 2010) can result into a number of discontinuous nerve fibers that can significantly affect the calculation of the clinical features and this issue was tackled efficiently by the proposed system here as described in (Section 3.2.4). Although, an efficient performance has been demonstrated in (Dabbah *et al.*, 2011), a training phase is required to train the adopted classifiers, which are used to classify the pixel to the fiber or non-fiber classes. However, promising results are provided by the proposed system for real-time requirements without any need for a training phase.

As mentioned before, the dataset was divided into four groups according to the severity of DPN. Therefore, clinical features, such as average nerve tortuosity, standard deviation of nerve tortuosity, average nerve thickness, length and density are computed for each subject in the database after determining the average for the whole image. This is followed by computing the overall average for each group, as summarized in Table 3.1. The extracted clinical features, obtained with the proposed system, are shown in Figure 3.12. There is a systematic decrease in nerve length and density and increase in nerve thickness and tortuosity associated with an increase in the severity of DPN, as shown in Table 3.1. However, the overall average nerve tortuosity did not give a useful estimation of the image tortuosity. This is because some images were classified by the ophthalmic clinicians as highly tortuous, because

they contained just one or two nerves with several branches. Therefore, the average image tortuosity is low for these images, even though some images for each subject had relatively larger average values.

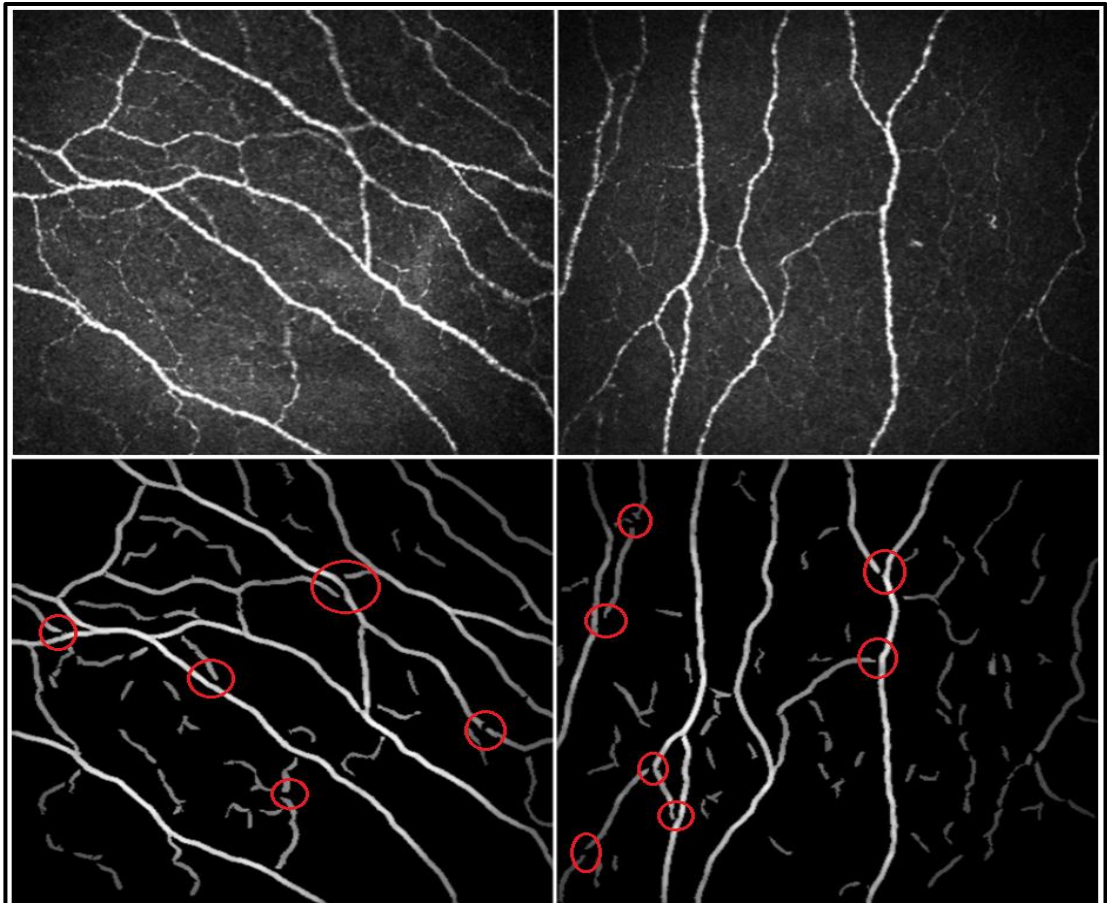
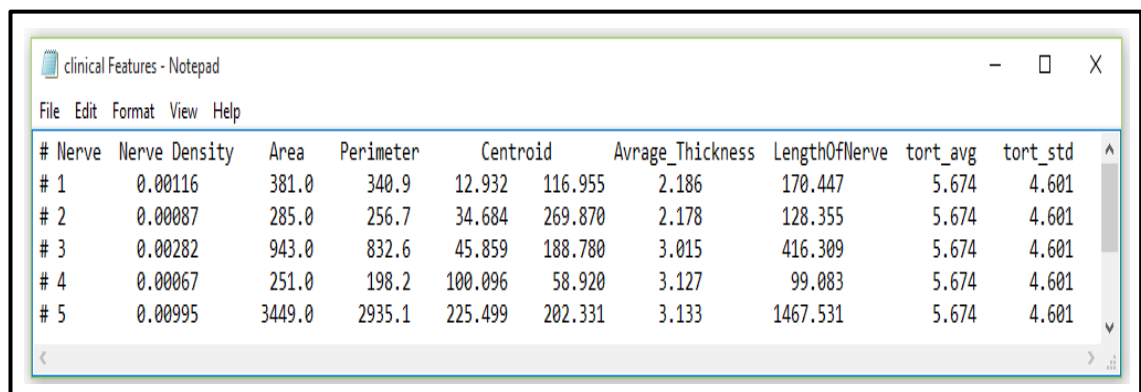


**Figure 3.11:** The output of the single scale dual-model detector: The images in the top row are the original images, while the bottom row is their response (Dabbah *et al.*, 2011).

By applying an empirical threshold to these averages, the image that provides an average tortuosity higher than the pre-defined threshold is counted. The average of the counted image is then combined with the overall average tortuosity for each subject by applying this procedure, it has been found that the overall average tortuosity provides meaningful information relating to the DPN severity, as shown in Figure 3.13 (a) and solves the problem mentioned above.



The most important clinical features are presented graphically in Figure 3.13. In this work, the clinical features obtained by the proposed automatic system, except for nerve thickness, were also compared against the ground truth manually traced by an experienced ophthalmologist. The main goal of this evaluation was to demonstrate the usefulness of the computed clinical features in differentiating control subjects from patients with diabetes and further differentiating diabetic patients in relations to the severity of neuropathy. The automated analysis of the proposed system presents equivalent results to the manual analysis, but the former is clearly quicker, more reliable and therefore clinically applicable. In this study, the execution time of the prototype was **13** seconds, starting from inputting the image until all the clinical features of each corneal image nerve are obtained.



# Nerve	Nerve Density	Area	Perimeter	Centroid	Average_Thickness	LengthOfNerve	tort_avg	tort_std
# 1	0.00116	381.0	340.9	12.932 116.955	2.186	170.447	5.674	4.601
# 2	0.00087	285.0	256.7	34.684 269.870	2.178	128.355	5.674	4.601
# 3	0.00282	943.0	832.6	45.859 188.780	3.015	416.309	5.674	4.601
# 4	0.00067	251.0	198.2	100.096 58.920	3.127	99.083	5.674	4.601
# 5	0.00995	3449.0	2935.1	225.499 202.331	3.133	1467.531	5.674	4.601

**Figure 3.12:** A readable text file format showing clinical features extracted from the first database.

**Table 3.1:** Summary of the descriptive clinical features of manually and automatically traced nerves extracted from the first database.

<b>Morphometric Parameters</b>					
<b>Groups</b>	<b>Manually Traced Nerves</b>				
	<b>Ave. Tort.</b>	<b>STD Tort.</b>	<b>Ave. Length (mm)</b>	<b>Ave. Density (Pixel/mm<sup>2</sup>)</b>	
<b>Control</b>	8.27	7.18	60.92	0.0262	
<b>Absent</b>	20.11	19.04	60.58	0.0222	
<b>Mild</b>	37.52	36.41	58.49	0.0188	
<b>Moderate</b>	40.45	39.30	57.08	0.0158	
<b>Groups</b>	<b>Automatically Traced Nerves</b>				
	<b>Ave. Tort.</b>	<b>STD Tort.</b>	<b>Ave. Length (mm)</b>	<b>Ave. Density (Pixel/mm<sup>2</sup>)</b>	<b>Ave. Thick (µm)</b>
<b>Control</b>	6.70	5.60	61.22	0.0316	2.83
<b>Absent</b>	13.9	12.79	60.34	0.0243	2.83
<b>Mild</b>	29.32	28.36	56.87	0.0182	2.85
<b>Moderate</b>	51.76	50.64	56.63	0.0164	2.88

To further evaluate and test the reliability and efficiency of the proposed system in extracting useful clinical features (e.g. nerve tortuosity, nerve thickness, nerve length and nerve density) and their relationship to DPN in a database of a total of 919 images taken from 172 individuals. The individuals were classified into controls, no neuropathy and neuropathy (See Section 3.2.1). The extracted clinical features using the proposed automated system are shown in Figure 3.14. There was an increase in the average nerve tortuosity and thickness and decreases in the average nerve length and density with increasing severity of DPN. The Graphical User Interface (GUI) of the proposed cornea sub-basal nerve system is shown in Appendix B.

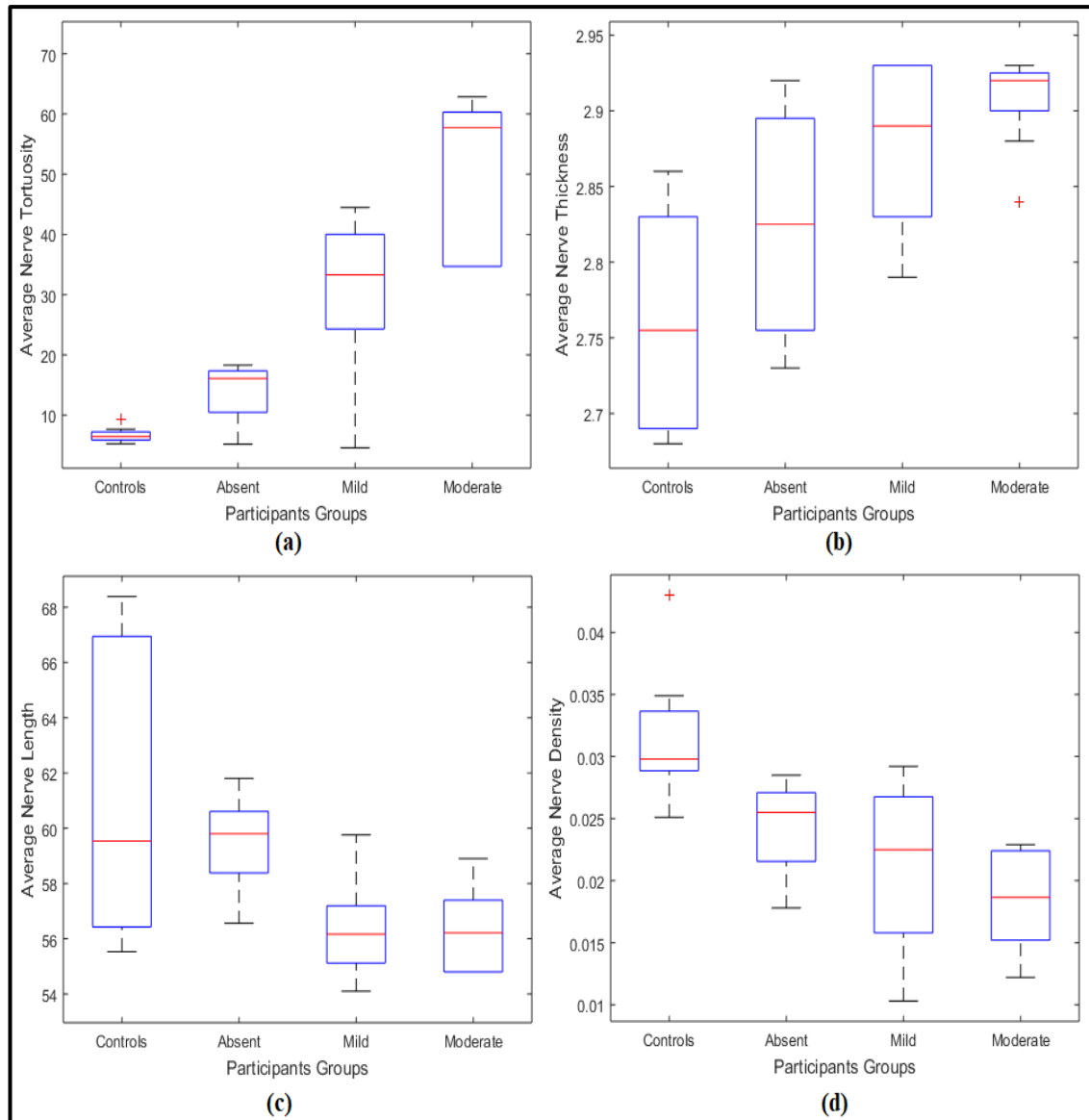


**Figure 3.13:** Representative box-plots with (median, inter-quartile range, outliers, and extreme cases of each parameter) illustrating the extracted clinical features from the first database: (a) Average Nerve Tortuosity, (b) Average Nerve thickness, and (c) Average Nerve Length, (d) Average Nerve Density.

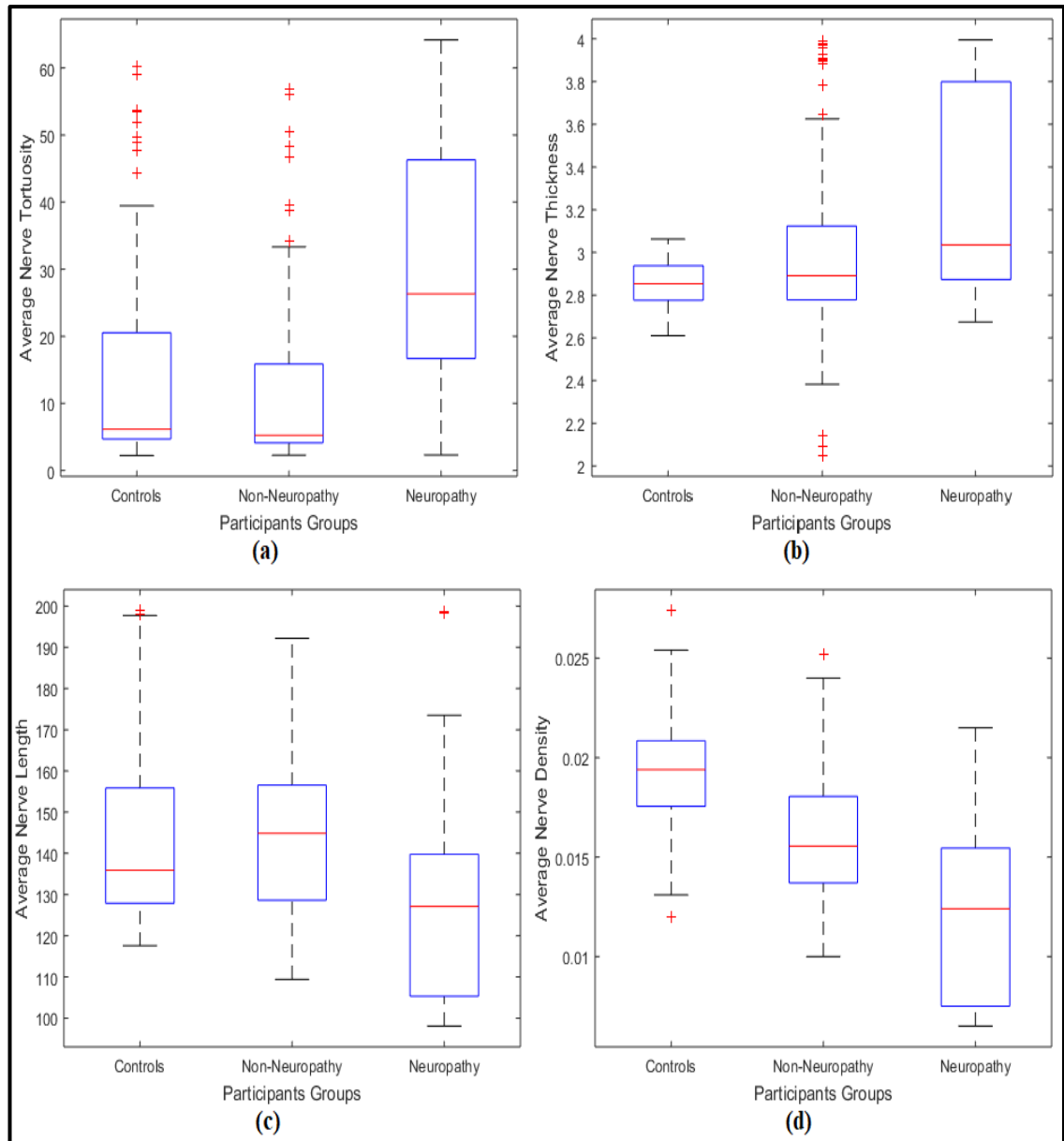


**Figure 3.14:** Representative box-plots with (median, inter-quartile range, outliers, and extreme cases of each parameter) illustrating the extracted clinical features from the second database: (a) Average Nerve Tortuosity, (b) Average Nerve Thickness (c) Average Nerve Length, and (d) Average Nerve Density.

### 3.4 Summary

In this work, a fully automatic, efficient real-time corneal sub-basal nerve segmentation and morphological parameter quantification system is proposed. Anisotropic diffusion and Gaussian filters were used to enhance the visibility of the nerve and to reduce the noise in the corneal image that can be caused by the acquisition process. In addition, an efficient technique is proposed to connect the discontinuous nerves. The results obtained have demonstrated the reliability and efficiency of the proposed segmentation system and the potential to use it as a real-time and a fully automatic nerve tracing system in patients with DPN as an early diagnostic and for follow-up. In the second stage, a number of useful clinical features, such as nerve length, density, thickness, and tortuosity as well as nerve perimeter, area and the image intensity were calculated for internal used. In this part, a new algorithm has been proposed to calculate the average nerve thickness. The results have demonstrated the effects of DPN on the corneal sub-basal nerves, in terms of increased average nerve tortuosity and thickness coupled with decreased average nerve length and density. Our results have demonstrated the effects of DPN on the corneal sub-basal nerves, in terms of increased average nerve tortuosity and thickness coupled with decreased average nerve length and density. For example, from Table 3.1 one can see that the average nerve tortuosity and thickness have increased from 6.70 and 2.83 respectively for the control group, to 51.76 and 2.88 in the moderate group. On the other hand, the average nerve length and density have decreased from 60.92 and 0.0262 respectively for the control group, to 57.08 and 0.0158 for the moderate group.

## Chapter 4

# Corneal Epithelium Registration System

### 4.1 Introduction

Recently, numerous clinical reports have pointed out that diabetes is a significant chronic health problem for which there is no currently an effective therapy (Malik *et al.*, 2003). In advanced cases, it is considered the main cause for foot ulceration, damage to the peripheral nerves and lower limb amputation. For example, in 2004, approximately 71,000 non-traumatic lower-limb amputations were conducted in the U.S. (Pritchard *et al.*, 2011). Moreover, DPN is one of the most long-term complications of diabetes and affects up to about 50% of patients (Boulton, 2005). Consequently, an accurate diagnostic and quantification of DPN are needed to define at-risk patients and for early diagnosis and application of new therapies. The eye is the only part of the human body in which nerves can be checked directly and non-invasively, therefore, a number of helpful clinical features can be extracted from images of these structures for early and accurate diagnostic of DPN. Particularly, rich nerve plexuses can be observed at the sub-basal corneal epithelial layer and in the retina using CCM and optical coherence tomography, respectively (Pritchard *et al.*, 2011).

In this study, a sequence of corneal images captured using CCM are used. In particular, those images contain the elongated and narrow corneal nerve fibers, which are captured from a specific corneal depth, a range of about 10  $\mu\text{m}$  inside the sub-basal epithelium layer. Recently, the analysis of corneal

nerves structures has received increasing interest because these nerves have been shown to produce quite important information about corneal damage various causes such as, surgical interventions on the cornea (e.g. LASIK and PRK) (Moilanen, 2003), wearing contact lens for a long time, corneal transplantation and fungal keratitis (Niederer *et al.*, 2007; Scarpa, Grisan and Ruggeri, 2008b). More recently, a significant link has been demonstrated between a number of clinical features extracted from these structures (e.g., nerve tortuosity, nerve thickness, nerve length, etc.) and the severity of diabetic neuropathy (Scarpa *et al.*, 2011). However, accurate estimation and quantification of these clinical features require a number of informative corneal images that have structural and functional information.

Image registration is an essential task in image analysis in which important information is obtained by integrating two or more images of the same object taken from different sensors, different viewpoints and/or at different times to produce a new informative image (Zitová and Flusser, 2003). Registration algorithms can be divided into four classes: correlation algorithms, FFT-based algorithms, feature-based algorithms and graph-theoretic algorithms (Srinivasa Reddy and Chatterji, 1996). Medical image registration has played a significant role in the data fusion of anatomical images captured using different imaging modalities, such as Computerized Tomography (CT), Magnetic Resonance Image (MRI), Single Photon Emission Computed Tomography (SPECT), Positron Emission Tomography (PET), or Magnetic Resonance Spectroscopy (MRS) which has increasingly improved the processes of clinical diagnosis, guiding treatment, and controlling disease progression (Oliveira and Tavares, 2014). In this work, an automatic corneal sub-basal nerve registration system is

proposed. The main aim of the proposed system is to produce a new informative corneal image that contains structural and functional information, which can help ophthalmologists to accurately extract meaningful clinical features using an improved visibility of corneal sub-basal nerves structures instead of using discontinuous nerves. In addition, a colour coded corneal image map is produced by overlaying a sequence of CCM images that differ in their displacement, scaling, and rotation to each other. The proposed method is based on combining the advantages of Fast Fourier Transform (FFT) and phase correlation techniques. The proposed registration algorithm searches for the best common features between sequenced CCM images in the frequency domain to produce the informative image map. In this image map, each colour represents the severity level of a specific clinical feature that can be used to give the ophthalmologist a clear representation of the extracted clinical features from each nerve in the image map. Moreover, the successful implementation of the proposed system and the availability of the required databases open the door for other interesting ideas; for instance, it can be used to give ophthalmologists a summarized and objective description about a diabetic patient's health status using a sequence of CCM images that have been captured from different imaging devices and/or at different times.

This chapter is organized as follows: Section 4.2 provides an overview of the proposed approaches for registering two images. Section 4.3 includes descriptions of the proposed methodology of corneal sub-basal nerve registration system and produce colour coded corneal nerve image map. Experimental results are presented in Section 4.4. Finally, a summary is stated in the last section.



## 4.2 The Proposed Methodology

In this section, the theoretical approach for registering two images that differ by rotation, translation and scale to each other based on the FFT properties (e.g. translation, rotation, and scaling), is explained. Image registration is an essential image processing operation, given the task to overlay two or more images and produce a more informative image than the originals (Madhuri, 2014). In this work, FFT is applied to the sequence of corneal sub-basal nerves images so rotation and scaling can be detected using a phase correlation technique. This is followed by applying the transformation module for the magnitude spectrum to one of the input images, and then the output image with the second image are used to recover the translation information using phase correlation technique in the log-polar space.

Phase correlation technique is well-known registration method that depends on the Fourier shift property to estimate the translation offset between two images (Yan and Liu, 2008). Given two images  $h_1(x, y)$  and  $h_2(x, y)$  that differ by a simple translational shift  $x_0$  in horizontal and  $y_0$  in the vertical directions, their corresponding Fourier transforms  $H_1(u, v)$  and  $H_2(u, v)$  are related as follows:

$$H_2(u, v) = e^{-j2\pi(ux_0 + vy_0)} * H_1(u, v) \quad (4.1)$$

Then, the normalized cross-power spectrum  $R$  between  $H_1$  and  $H_2$  is computed using the phase correlation technique as follows:

$$R = \frac{H_2(u, v)H_1^*(u, v)}{|H_2(u, v)H_1^*(u, v)|} = e^{-j2\pi(ux_0 + vy_0)} \quad (4.2)$$

where  $H^*$  is the complex conjugate of  $H$ . The Fourier shift theorem ensures that the cross-power spectrum phase is equivalent to the difference between the two images. The translation offsets  $(x_0, y_0)$  can be acquired by detecting the location of the peak in the Inverse-FFT of  $R$ .

The FFT based phase correlation registration algorithm to detect translation, rotation and scale differences is described in detail in (Srinivasa Reddy and Chatterji, 1996). If  $f_s(x, y)$  is a translated, rotated and scaled replica of the reference image  $f_r(x, y)$ , with translation offsets  $(x_0, y_0)$ , rotation angle  $\theta_0$  and scale factor  $k$ , then,

$$f_s(x, y) = f_r[k(x \cos \theta_0 - y \sin \theta_0) - x_0, k(x \sin \theta_0 + y \cos \theta_0) - y_0] \quad (4.3)$$

Their corresponding Fourier transforms  $F_s$  and  $F_r$  and magnitudes are defined using the Fourier shift theorem as follows:

$$F_s(u, v) = \frac{1}{k^2} e^{-j2\pi((ux_0/k) + (vy_0/k))} * F_r\left(\frac{u \cos \theta_0 - v \sin \theta_0}{k}, \frac{u \sin \theta_0 + v \cos \theta_0}{k}\right) \quad (4.4)$$

$$|F_s(u, v)| = \frac{1}{k^2} |F_r\left(\frac{u \cos \theta_0 - v \sin \theta_0}{k}, \frac{u \sin \theta_0 + v \cos \theta_0}{k}\right)| \quad (4.5)$$

Let  $M_s$  and  $M_r$  denote the magnitude spectra of  $F_s$  and  $F_r$ , respectively, they are defined as follows:

$$M_s(u, v) = \frac{1}{k^2} M_r\left(\frac{u \cos \theta_0 - v \sin \theta_0}{k}, \frac{u \sin \theta_0 + v \cos \theta_0}{k}\right) \quad (4.6)$$

if  $G_s$  and  $G_r$  are the transforms of  $M_s$  and  $M_r$ , expressed in polar coordinates, i.e.

$$\begin{cases} \rho = (u^2 + v^2)^{1/2} \\ \theta = \tan^{-1}(u/v) \end{cases} \quad (4.7)$$

Then:

$$G_s(\rho, \theta) = \frac{1}{k^2} G_r(\rho/k, \theta + \theta_0) \quad (4.8)$$

$$G_s(\log \rho, \theta) = \frac{1}{k^2} G_r(\log \rho - \log k, \theta + \theta_0) \quad (4.9)$$

Next, the scaling factor  $k$  and rotation angle  $\theta_0$  are acquired using the phase correlation technique. Once, the scaling and rotation parameters are acquired, the  $f_r(x, y)$  image is scaled and rotated using the obtained parameters. Finally, the phase correlation technique is applied again to find out the translation offsets  $(x_0, y_0)$ . Once, all parameters  $(x_0, y_0, \theta_0, k)$  have been obtained, the 2D image registration process between the two images has been completed.

### 4.3 Corneal Nerve Registration System

The main steps of the proposed automatic corneal sub-basal nerve registration system to produce a new informative corneal image map that contains both structural and functional information are illustrated in Figure 4.1. The generated corneal image map can play a significant role by improving the nerve visibility and acquiring more precise clinical features with less processing time instead of searching manually through a sequence of CCM images to extract these features from each image individually. Firstly, a sequence of corneal nerve images  $(f_1, f_2, \dots, f_n)$  are used that may differ in their displacement (viewpoint) because they are captured using different sensors and/or at different times. Moreover, they can be captured with non-uniform distribution of the lighting in different areas of the corneal layer due to the spherical shape of the cornea and may have some observed artefacts as a result of eye movement during the acquisition process. Secondly, an automatic image registration algorithm is employed to align this sequence of corneal

images where the first image is aligned with the second image and the generated registered image will be aligned with the next corneal image in the sequence and so on. After that, a fully automatic nerve segmentation algorithm (as explained in Chapter 3) is applied to the generated image map from the previous step. This is followed by producing a colour coded map of the corneal nerve image that represents the magnitude of a specific clinical feature.

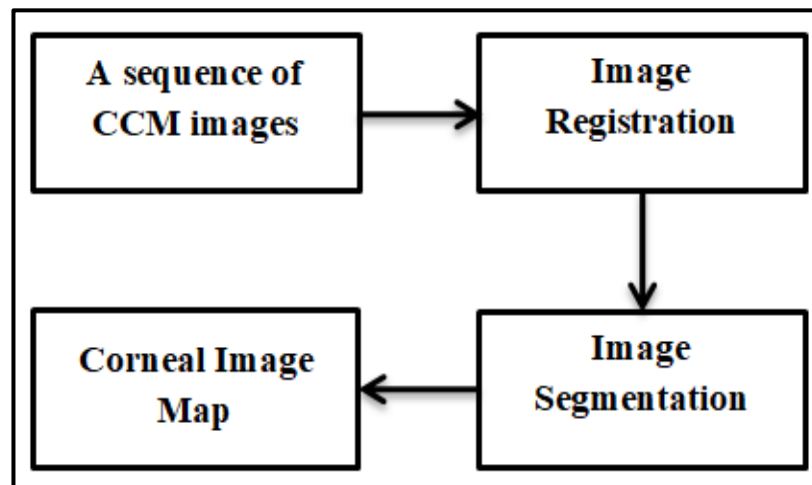


**Figure 4.1:** The main steps of the proposed corneal sub-basal nerve registration system to generate a colour coded corneal nerve image map.

#### 4.3.1 Image Registration

The proposed registration algorithm searches for an optimal match using information in the frequency domain in order to align a sequence of corneal sub-basal images that differ in their displacement, scaling, and rotation. The major steps of the implemented image registration algorithm to align two corneal images  $f_1(x, y)$  and  $f_2(x, y)$  can be summarized as follows:

1. Apply the 2D-FFT to the input images  $f_1(x, y)$  and  $f_2(x, y)$  to obtain the Fourier magnitude spectra  $F_1(u, v)$  and  $F_2(u, v)$ , as described in Eq.4.4.

2. The Fourier magnitude spectra of the input images are multiplied with a high-pass emphasis filter to make an image appear sharper and emphasize fine details in the image. A simple high-pass filter is used as follows:

$$H(x, y) = (1.0 - (\cos(\pi x) \cos(\pi y))) * (2.0 - (\cos(\pi x) \cos(\pi y))) \quad (4.10)$$

where  $(-0.5 \leq (x, y) \leq 0.5)$ .

3. The Fourier log-magnitude spectra is used for mapping from the Cartesian coordinates to log-polar coordinates rather than the Fourier magnitude spectra, as described in Eq.4.9. This conversion is known as a Mellin transform conversion.
4. In log-polar coordinates, the cross power spectrum (cross-correlation between two signals) is computed by applying the phase correlation technique to both images, as described in Eq.4.2. Followed by detecting the location of the peak of Inverse-FFT of the cross-power spectrum to obtain the scaling factor and rotation angle.
5. A transformed image is acquired from  $f_1(x, y)$  using acquired scaling and rotation information as affine transformation parameters. In this work, the transformation is implemented using “nearest” interpolation of the  $f_1(x, y)$  image. Finally, the phase correlation technique is applied again to compute the cross power spectrum phase from the transformed image and  $f_2(x, y)$  to find out the translation offsets  $(x_0, y_0)$ . A block diagram of the proposed system is shown in Figure 4.2.
6. Once, all parameters  $(x_0, y_0, \theta_0, k)$  have been obtained, image registration is performed and the generated image map is used as a reference image

with the next image in the sequence of CCM images, as shown in Figure 4.3.

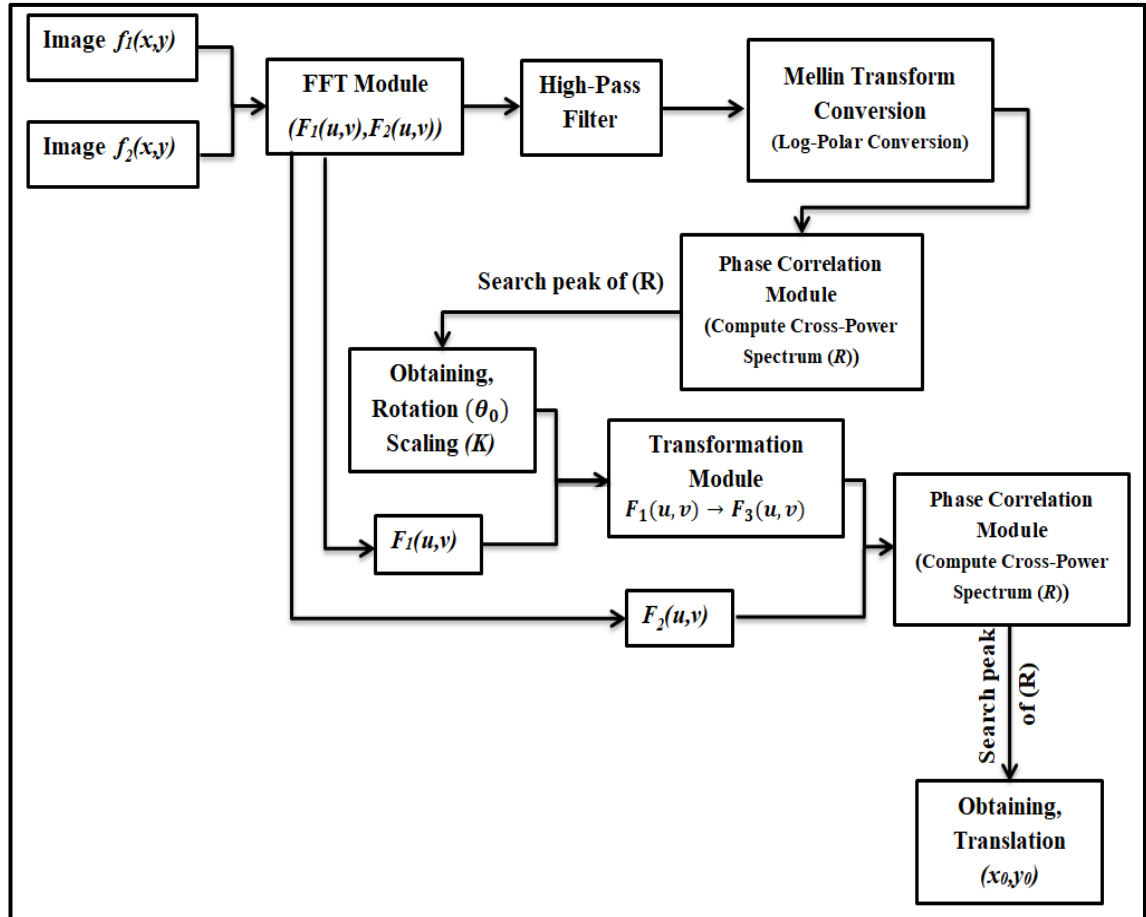


**Figure 4.2:** Overview of the automatic Fourier and phase correlation based image registration algorithm.

### 4.3.2 Image Segmentation

The nerve tracing task is performed using a fully automatic corneal sub-basal nerve segmentation system, as described in Chapter 3. This system consists of two main stages: nerve segmentation and a morphometric parameters quantification stage. Nerve segmentation stage consists of three steps: pre-processing, morphological operations and edge detection. In the morphometric parameters quantification stage, a number of clinically useful

features are calculated including density, length, thickness, tortuosity of the nerve that can be used for the early diagnosis and follow up of DPN using CCM images.

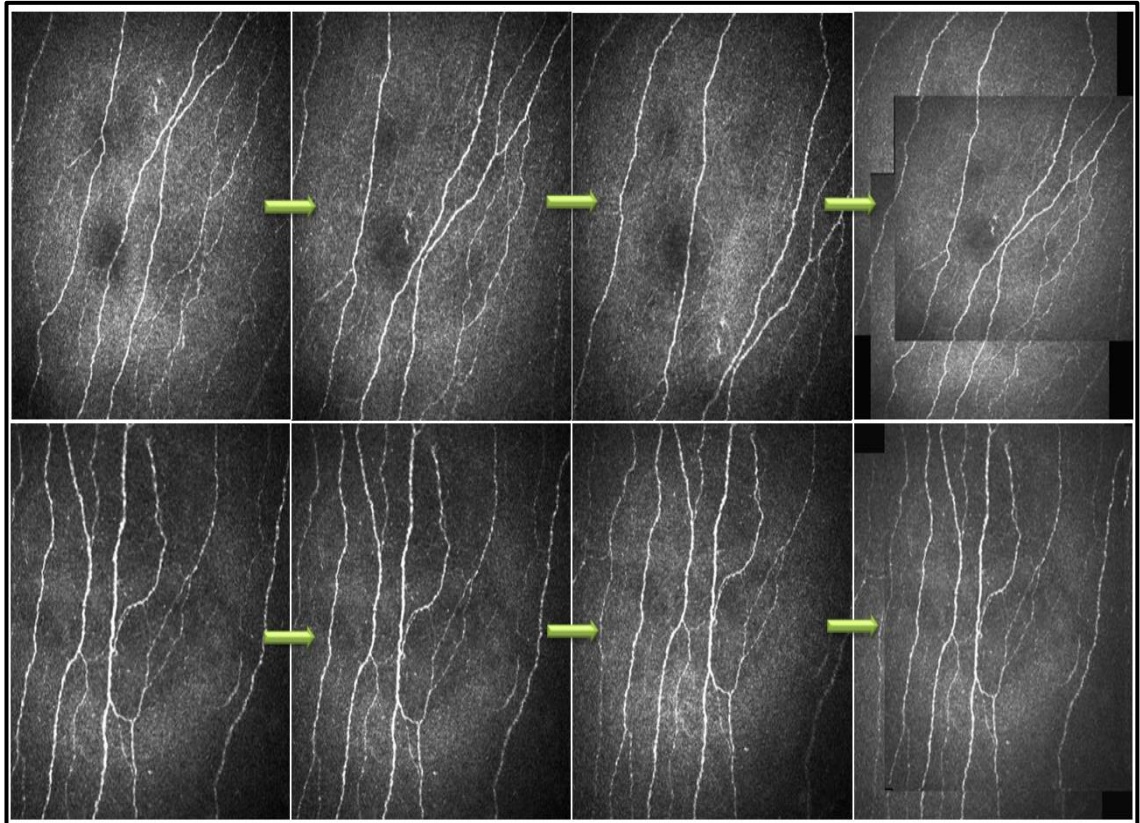


**Figure 4.3:** Applying image registration algorithm on three sequenced CCM images where the last column represents the output.

As mentioned in Chapter 3, the performance of the cornea sub-basal nerve segmentation system has been tested and evaluated against manually traced ground-truth images in a database consisting of 498 corneal sub-basal nerve images (238 are normal and 260 are abnormal) (Otel *et al.*, 2013). In addition, the efficiency of the proposed cornea sub-basal nerve segmentation system in extracting useful and meaningful clinical features has also been evaluated using a database of a total of 919 images taken from 172 healthy

subjects and diabetic patients with and without neuropathy (Chen *et al.*, 2015b). Some examples of applying cornea sub-basal nerve segmentation system on the corneal image map generated from the proposed corneal sub-basal nerve registration system are shown in Figure 4.4.

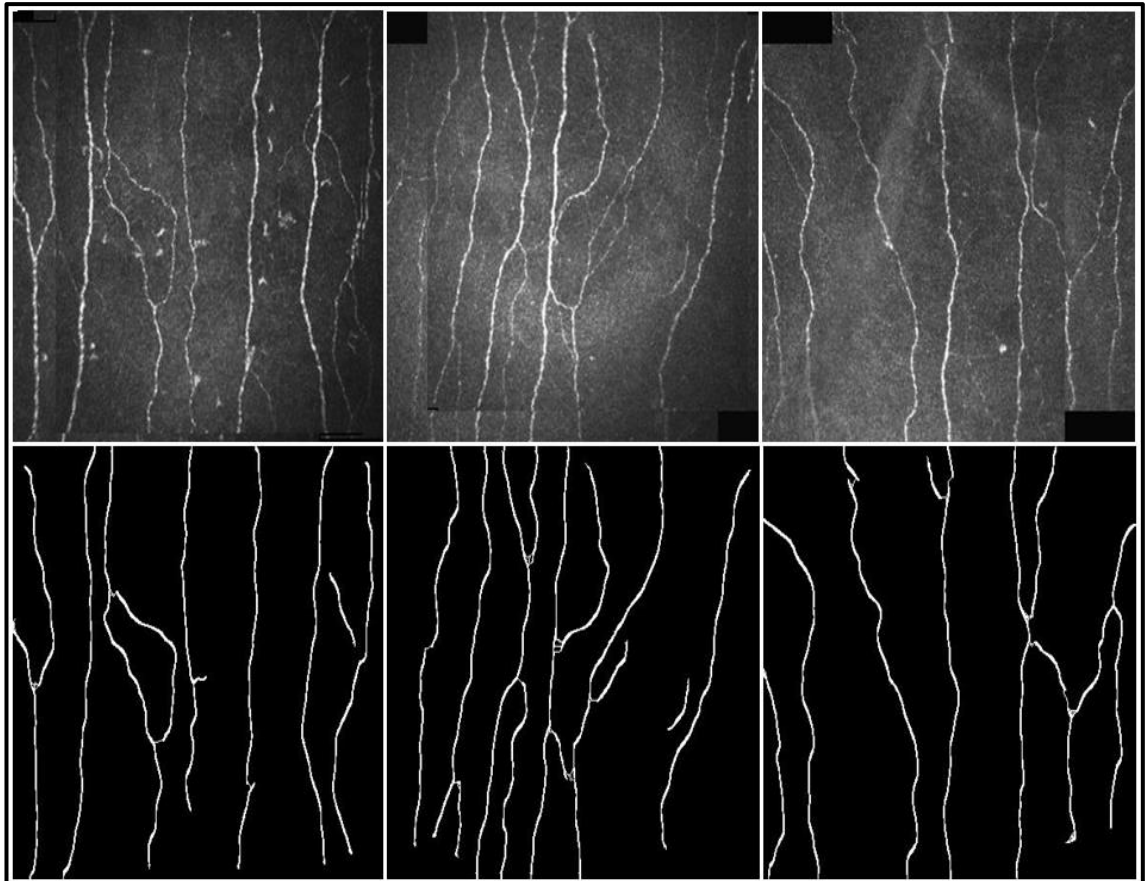


**Figure 4.4:** Corneal nerve segmentation system outputs: Top row is the original corneal images and bottom row is binary segmented images.

### 4.3.3 Corneal Image Map

The final output of the proposed corneal sub-basal nerve registration system produces a colour coded corneal nerve image map that can be used to give ophthalmologists an efficient and clear representation of the extracted clinical features from each nerve in the image with less running time required as



will be explained later. As shown in Figure 4.5, a specific colour can refer to the severity level of a specific clinical feature (e.g., nerve tortuosity). This colour coded corneal nerve image map could be used to help ophthalmologists in efficiently monitoring the patient's treatment planning and diagnosis by giving a summarized and objective description about the health status of each nerve throughout a sequence of CCM images.

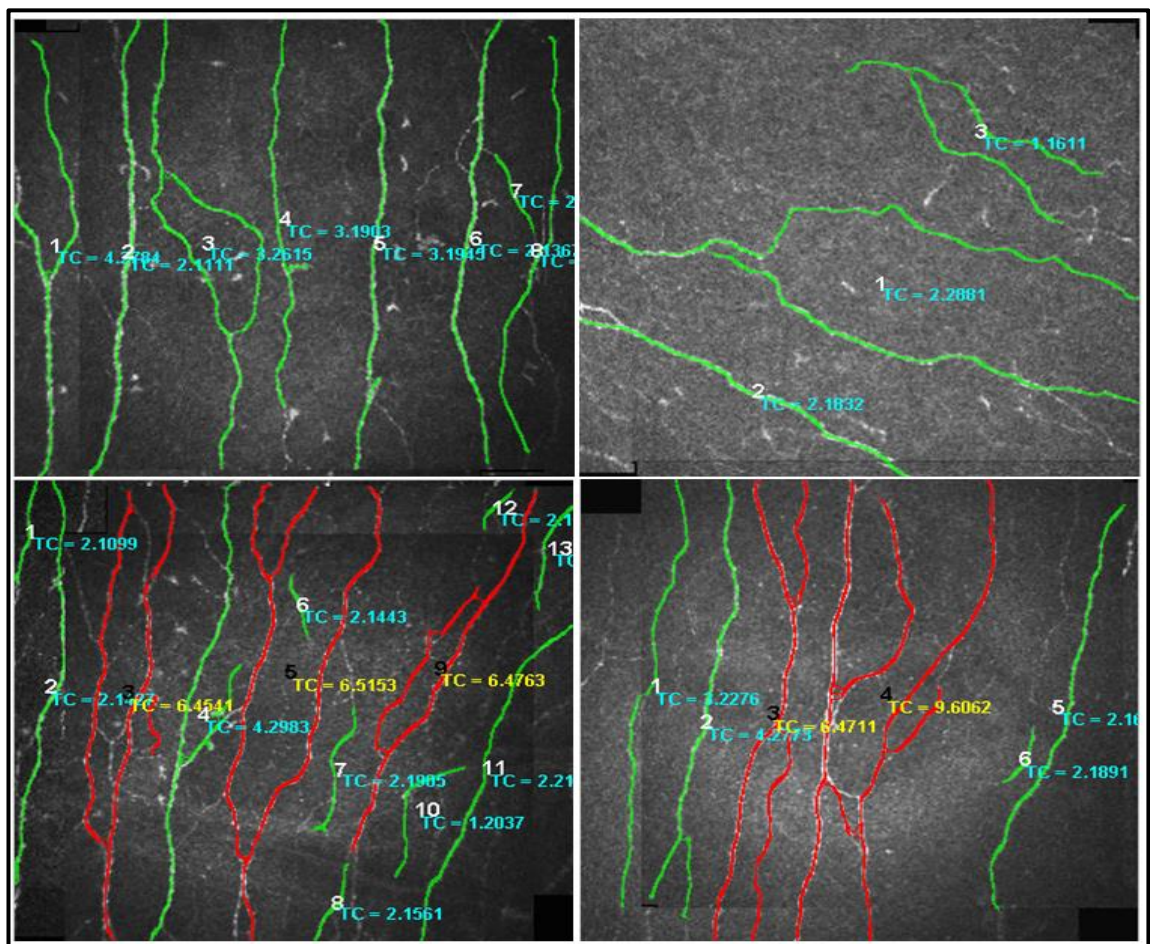


**Figure 4.5:** The colour coded corneal nerve image map of the nerve tortuosity: Top row represents the control group, while bottom row represents the patient's group.

## 4.4 Experimental Results

Due to unavailability of a database that contains a large sequence of CCM images, the performance of the proposed system is evaluated and tested on a database of 30 subjects (18 controls and 12 diabetic patients) with a sequence of CCM images that varies between 3 and 4 images per subject (Otel *et al.*, 2013). These sequenced CCM images are collected as a subset of the first database described in (Chapter 3, Section 3.2.1). In this database, the CCM images were captured using a Heidelberg Retinal Tomograph equipped with a Cornea Rostock Module (HRT-CRM: Heidelberg Engineering, Heidelberg, Germany). The images are stored in JPEG format with a size of (384×384) pixels covering (400×400)  $\mu\text{m}^2$  of the cornea at an optical magnification of 63X. In this work, all the clinical features of the corneal sub-basal nerve are extracted from the generated image map, including nerve tortuosity, nerve thickness, nerve length, and nerve density. Then, the ophthalmologist will be able to present the severity of each clinical feature as a colour coded map, where the red coloured nerves refer to the highest level of that clinical feature while the green coloured nerves refer to the lowest or normal level of this parameter, as shown previously in Figure 4.5. The severity of each clinical feature is determined using a pre-defined threshold, which is determined empirically. This pre-defined threshold can be adjusted manually by the ophthalmologist, to ensure that the performance of the proposed system can meet the requirements of the clinical domain and provides meaningful information relating to the DPN severity.

The results obtained have demonstrated that the reliability and efficiency of the proposed corneal sub-basal nerve registration system in generating the

colour coded corneal image map in real-time, where the execution time for the complete process is about 10 seconds. The execution time without image registration is about 7 seconds, which means for three CCM images it takes about 21 seconds. This means the execution time has been reduced by more than half to analyse a more informative CCM image. The running time was measured by implementing the proposed system on a PC with the Windows 8.1 OS, 6 GB of RAM and a 1.80 GHz Core i5-3337U CPU. The system code was written in MATLAB R2010a. In addition, useful clinical features (e.g. nerve tortuosity, nerve thickness, nerve length and nerve density) are extracted from the generated map for each group in the database. The clinical features using the proposed automated system are shown in Figure 4.6. From this figure, one can see that both nerve tortuosity and thickness are higher in the diabetic patient's group than in the controls group. It is also found that the nerve length and density are lower in the diabetic patient's group than in the controls group. As summarized in Table 4.1, the overall average of each parameter of these clinical features (e.g., Average Nerve Tortuosity (ANT), Average Nerve Thickness (ANTh), Average Nerve Length (ANL) and Average Nerve Density (AND)) before and after applying the proposed corneal sub-basal nerve registration system is computed for each group in the database after deriving the average for the whole image. From this Table, one can see that better meaningful clinical features are obtained using the generated image map. For instance, an average difference value of each parameter of the extracted clinical features between the controls and patients groups has increased from 0.75, 0.01, 1.3 and 0.002 to 3.31, 0.24, 16.3 and 0.014 for ANT, ANTh, ANL and AND respectively before and after applying the proposed corneal sub-basal

nerve registration system, respectively. The obtained results have further strengthened the proposed hypothesis that using the generated image map as a more informative corneal image can provide better structural and functional information about the corneal sub-basal nerves.

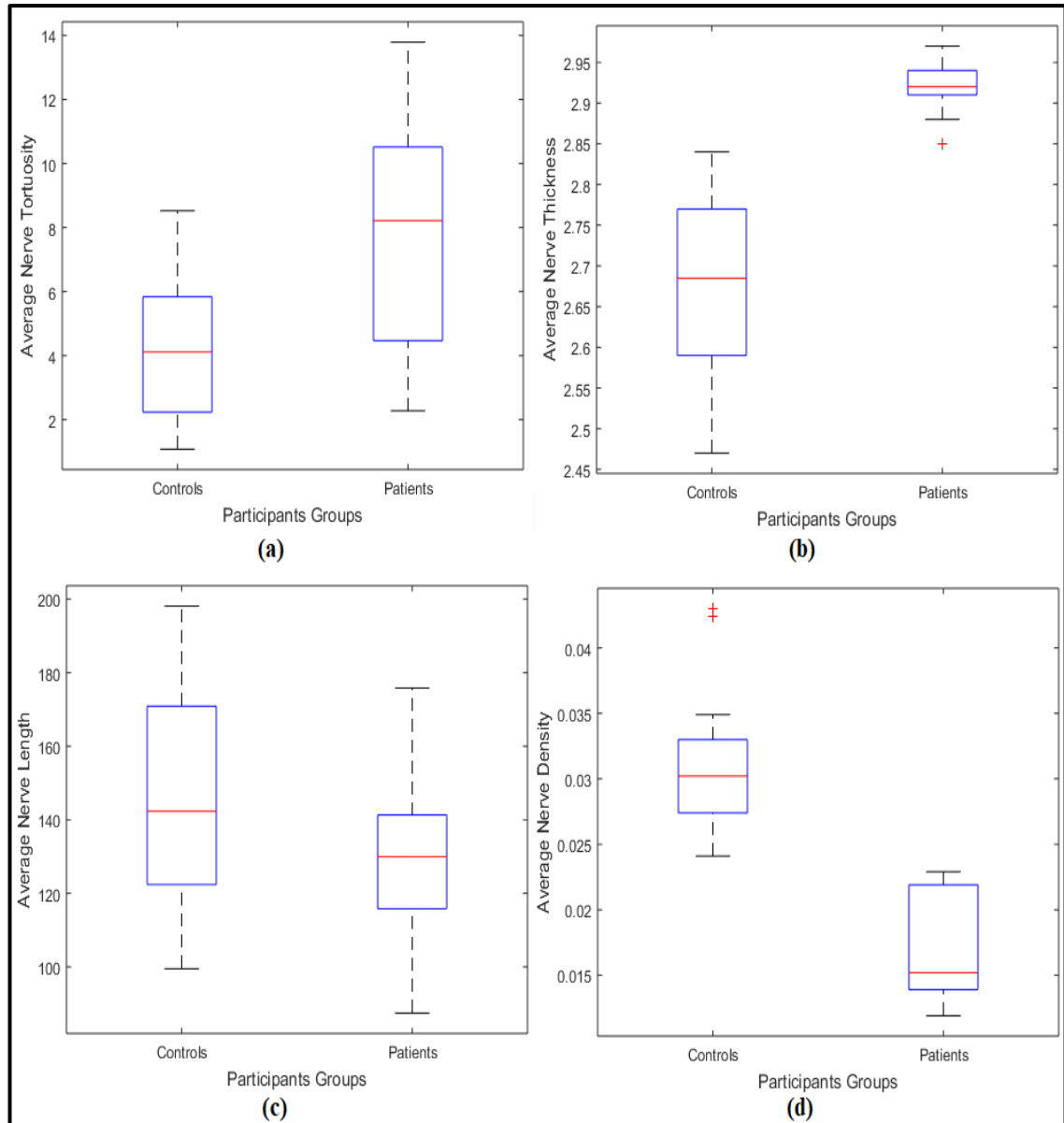


**Figure 4.6:** Representative box-plots with (median, inter-quartile range, outliers, and extreme cases of each parameter) illustrating the extracted clinical features from the controls and patients group: (a) ANT (b) ANTh, (c) ANL and (d) AND.

**Table 4.1:** The descriptive summary of the clinical features before and after applying the proposed corneal sub-basal nerve registration system.

Groups	Before Image Registration				After Image Registration			
	ANT	ANTh ( $\mu\text{m}$ )	ANL (mm)	AND (Pixel/mm <sup>2</sup> )	ANT	ANTh ( $\mu\text{m}$ )	ANL (mm)	AND (Pixel/mm <sup>2</sup> )
Controls	5.68	2.80	60.5	0.0221	4.30	2.68	146.5	0.0311
Patients	6.43	2.81	59.2	0.0201	7.61	2.92	130.2	0.0170

## 4.5 Summary

In this work, an automatic corneal sub-basal nerve registration system is proposed using FFT based phase correlation technique. The main part of the proposed system is the image registration method that is based on finding the best common features between a number of sequenced CCM images in order to produce a more informative corneal image than the original images. Then, a colour coded corneal image map is generated from the latest registered corneal image, which can be used to help ophthalmologists produce faster and more meaningful information relating to the DPN severity. In this work, the efficiency of using the generated corneal image map has been investigated by calculating four useful clinical features, which are nerve tortuosity, nerve thickness, nerve length and nerve density in order to distinguish between the health of different patient groups. The results obtained have demonstrated the reliability and efficiency of the proposed corneal sub-basal nerve registration system in generating a more informative and colour coded corneal image map with shorter execution time compared to the original images.

# Chapter 5

## Cornea Endothelium Analysis

### 5.1 Introduction

In Vivo CCM is a fast non-invasive clinical technique for acquiring images and quantifying morphological changes in the cornea to provide insights into a range of endothelial pathologies and infections (Zheng *et al.*, 2016). Corneal transparency is primarily dependent on corneal stromal hydration, which is maintained by an active transport mechanism in the corneal endothelium (Foracchia and Ruggeri, 2007). The corneal endothelium is a connected single-layer of hexagonal uniformly sized cells on the posterior surface of the human cornea (Scarpa and Ruggeri, 2015). Several factors can damage this regular tessellation and cause cell loss, including aging, intraocular surgery, inflammation or other ocular or systemic pathologies (Hatipoglu *et al.*, 2014). Damage to the endothelial cells can lead to altered hydration of the corneal stroma and visual loss, which may be associated with irreversible endothelial cell pathology requiring corneal transplantation (Keratoplasty) (Navaratnam *et al.*, 2015). The corneal endothelial loss is compensated by an enlargement and migration of neighbouring cells due to a lack of regenerative capacity of the corneal endothelium. This results in a decrease in cell density, increase in the variation of the cell surface area and deformation of the hexagonal pattern of endothelial cells, which can cause disruption of endothelial layer function as a fluid barrier (McCarey, Edelhauser and Lynn, 2008).

In vitro quantitative analysis of the corneal endothelium is currently undertaken at eye hospitals to assess the functional capacity of the corneal endothelium, and hence the quality of the cornea prior to transplantation (Ruggeri, Grisan and Jaroszewski, 2005). A minimum Endothelial Cell Density (ECD) of 400 to 600 (cells/mm<sup>2</sup>) is an indicator of corneal endothelial health and most donor corneas should have an ECD of at least 2000 (cells/mm<sup>2</sup>) to be authorized for keratoplasty (Hatipoglu *et al.*, 2014; Gain *et al.*, 2002). The corneal endothelium should also ideally have 100% Hexagonality, with 60% being accepted as an indicator of a healthy corneal endothelium (McCarey, Edelhauser and Lynn, 2008). The most commonly used features to quantify endothelial cell health are: Endothelial Cell Density (ECD) (cell/mm<sup>2</sup>), polymegathism (Coefficient of Variation in cell size), pleomorphism (Percentage of Hexagonality Coefficient), Mean Cell Area (MCA) (μm<sup>2</sup>) and Mean Cell Perimeter (MCP). However, these features are not frequently used in the clinical setting due to the considerably errors of cell boundary detection (Doughty and Aakre, 2008). Recently, even healthy control subjects have been shown to have significant differences in ECD and pleomorphism in central and peripheral areas of the cornea (Zheng *et al.*, 2016). To date, the quantitative analysis of the corneal endothelium has been manually performed by visual inspection of images by ophthalmologists. ECD is derived by experts counting all the endothelial cells inside a selected Region of Interest (ROI) aided using a digital image tool that allows them to place a mark on each endothelial cell (Ruggeri, Grisan and Jaroszewski, 2005). This manual procedure is tedious, time-consuming, highly subjective, and error-prone, and does not allow the geometric analysis of endothelial cell shape (Foracchia and Ruggeri, 2007).

This limits the quantification of the additional morphometric features to clinical research and does not allow adoption for routine clinical use. Currently, an ophthalmologist needs at least 4 minutes to simply calculate only the cell density. Furthermore, morphometric parameters other than cell density (e.g., polymegathism and pleomorphism) have not been practical in clinical setting up to date (Selig *et al.*, 2015). However, the additional morphometric features can be easily measured if the endothelial cell boundaries are correctly identified (Scarpa and Ruggeri, 2015). An objective and fully-automated segmentation and quantification system enabling rapid quantitative analysis of the corneal endothelium would facilitate translation to the clinical setting. In other words, to enable and make the estimation of the clinical morphometric parameters practical in clinical settings, a computerized system that can accurately and automatically detects the endothelial cell boundaries in the field of view would be needed. Whilst several prototype systems have been proposed to automatically detect endothelial cell boundaries, the quality of the captured images (e.g., images are often blurred and noisy) can result in significant issues in the detection of cell boundaries requiring operator interaction to guide the detection process and hence reducing the speed of analysis.

In this research, a totally automatic, robust and real-time system is proposed, termed the Corneal Endothelium Analysis System (CEAS) for the segmentation and computation of the different morphological parameters of endothelial cells in the human cornea obtained by In Vivo corneal confocal microscopy. First, an FFT-Band-pass filter is applied to reduce noise and enhance the image quality to make the cells more visible. Secondly, a watershed transform and a Voronoi tessellation are applied to detect all the



endothelial cells in the image, which facilitates the robust and accurate extraction of the endothelial cell contour. This chapter is organized as follows: Section 5.2 includes descriptions of the proposed methodology of corneal cells segmentation and quantification system with the data used. The experimental results are presented in Section 5.3. Finally, a summary is stated in the last section.

## 5.2 The Proposed Methodology

The proposed CEAS system is a completely fully-automated system which requires no user intervention to accurately detect cell contours. Unlike other supervised segmentation approaches (Katafuchi and Yoshimura, 2017; Fabijańska, 2017), which require long time to train the neural network to detect the cell contours, no training procedure is required for the proposed CEAS system. It also quantifies the additional morphometric features (e.g., Polymegathism, Pleomorphism, etc.), which is an inherent limitation in many the built-in tools. For example, the built-in software included in the HRT Rostock Cornea Module (Heidelberg Engineering GmbH; Heidelberg; Germany) can only measure cell density. As depicted in Figure 5.1, the proposed CEAS system consists of two essential stages: a cell segmentation stage and a morphometric parameter quantification stage. The former stage can be further divided into two steps: a pre-processing step to enhance image quality and a cell contour detection step to accurately detect cell boundaries. In the latter stage, a number of useful clinical parameters are calculated, including: Mean Cell Density (ECD), Polymegathism, Pleomorphism, Mean Cell Area (MCA) and Mean Cell Perimeter (MCP). These additional morphologic parameters may

play a significant role in early diagnosis of corneal pathology and in determining health status of corneas for transplantation.

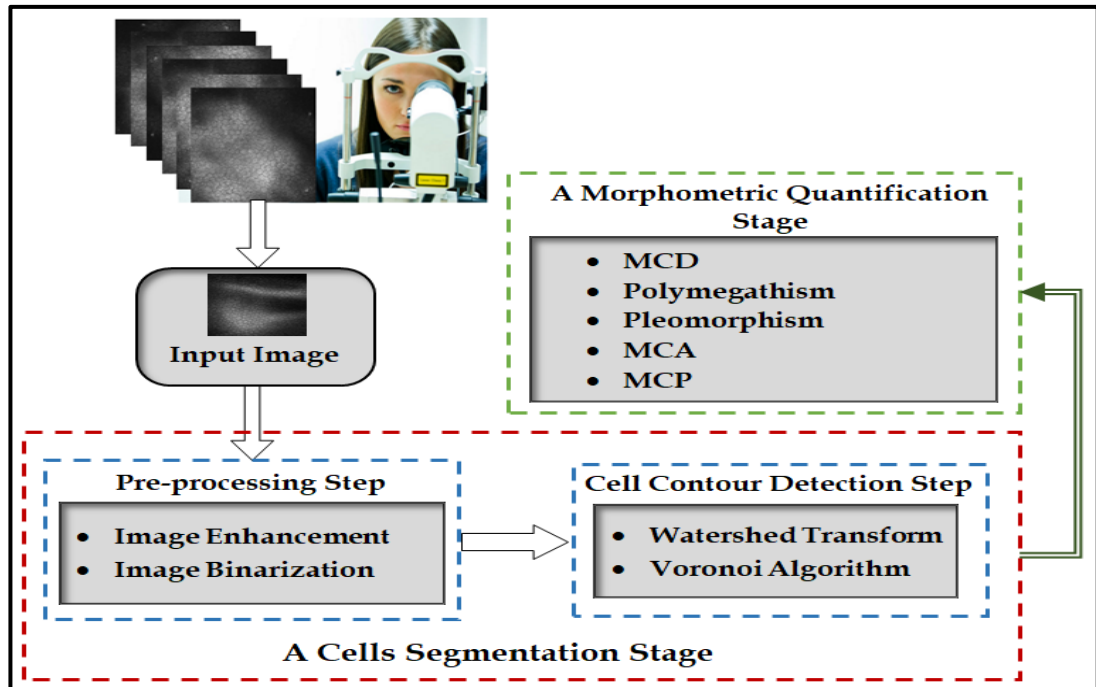


**Figure 5.1:** An illustration of the process for the automated corneal cell segmentation and quantification system (CEAS).

### 5.2.1 Data Used

In this work, a total of 80 images of corneal endothelial cells were acquired using a laser CCM (Heidelberg Retinal Tomograph III Rostock Cornea Module HRT III RCM; Heidelberg Engineering GmbH; Heidelberg; Germany) according to an established protocol (Tavakoli and Malik, 2011). The images were taken from the central cornea using the section mode and saved in BMP format with 8-bit grey levels and size (384×384) pixels (400×400)  $\mu\text{m}^2$ , corresponding to a square pixel of size 1.0417 $\mu\text{m}$ . It is important to note that the images used in this work were extremely challenging with the very low quality compared to those in literature, due to the non-uniform illumination and presence of different types of noise and artifacts caused by high amounts of

distortion. Examples of original and unprocessed images of the endothelial cell layer with different types of noise and artifacts are shown in Figure 5.2. These images were divided into two databases, each containing 40 images.

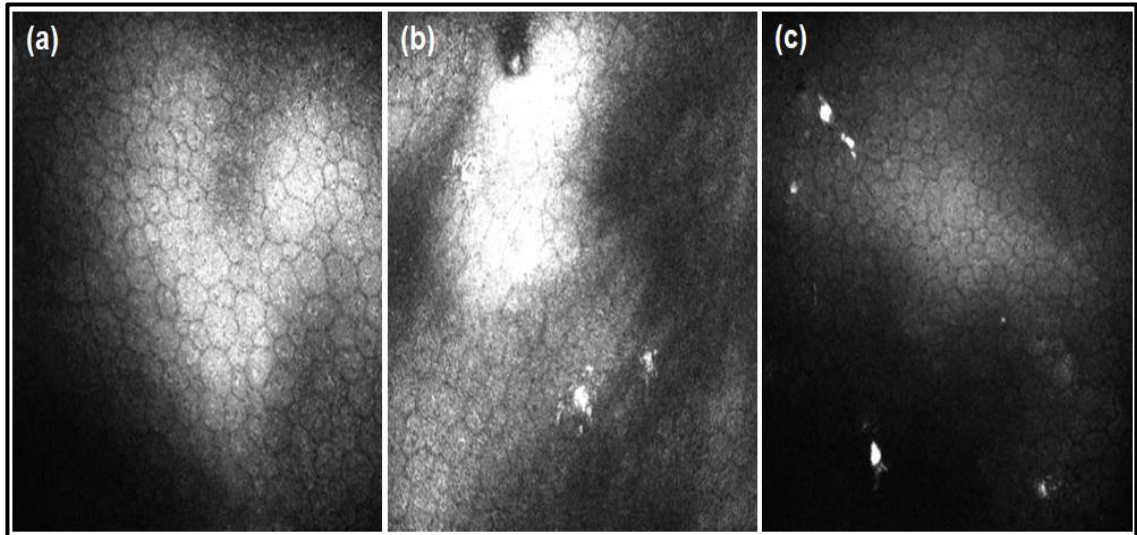


**Figure 5.2:** Examples of original corneal endothelial cell images with different types of noise and artifacts: (a) Darker areas in the peripheral regions, (b) Non-uniform illumination with blurring effect due to saccadic eye movement, and (c) Darker areas with unwanted bright objects.

### 5.2.2 Pre-processing Step

The images acquired using CCM usually suffer from several types of artefacts (e.g., blurring, noise, specular reflections, low contrast and non-uniform illumination) that make detection of the correct contour of the cells a challenging task (Figure 5.2). The main reasons for the poor quality images in the acquisition process (Sharif *et al.*, 2014) include: (i) saccadic eye movement during image acquisition resulting in blurred images, (ii) differences in the pressure applied between the CCM Tomocap and cornea, (iii) the spherical shape of the cornea leads to non-regular distribution of the lighting in different corneal areas.

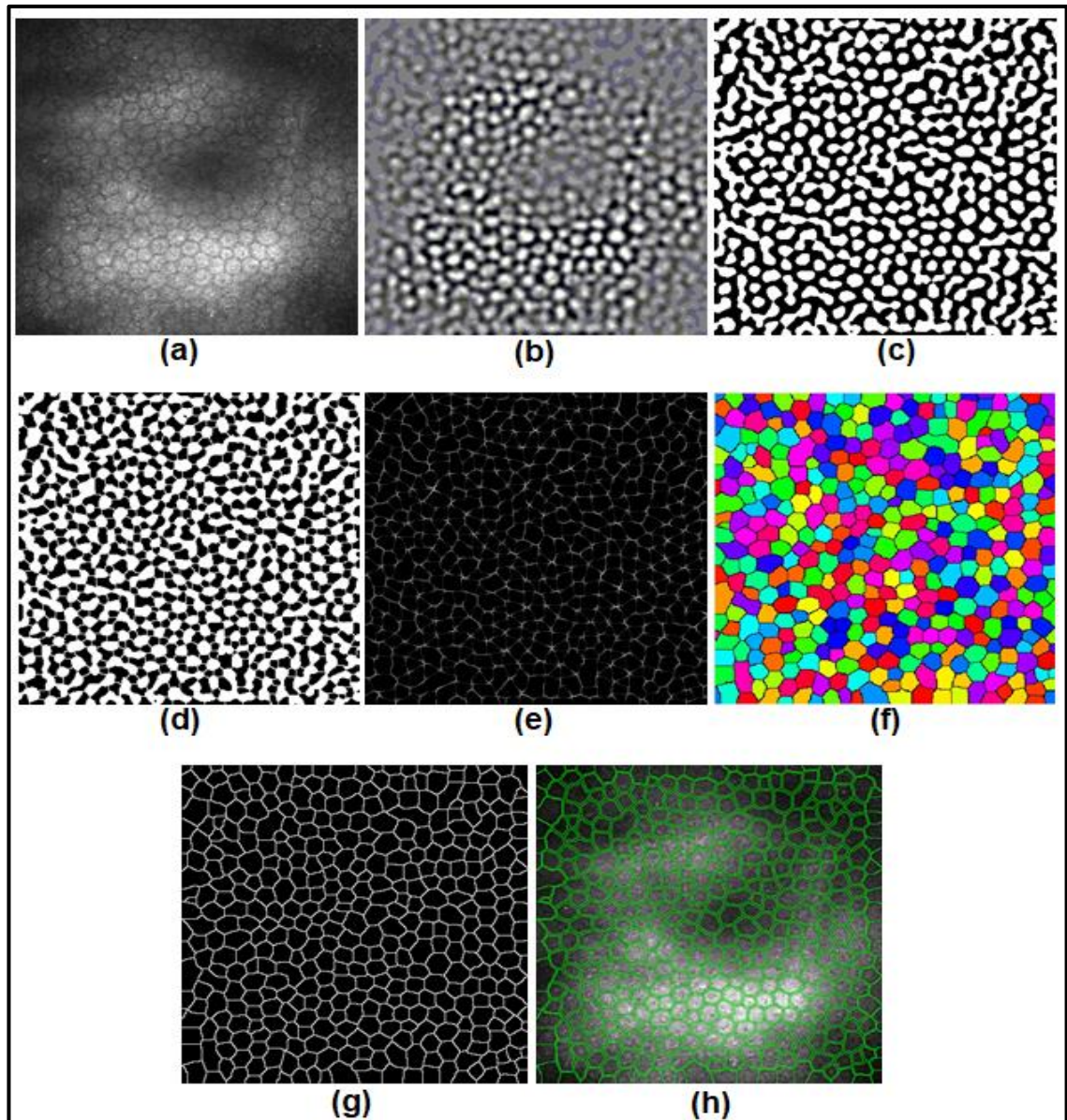
The pre-processing stage aims at addressing these problems. A FFT based band-pass filter is applied for noise reduction to enhance image quality and make cell borders more visible, especially when there is a significant difference in pixel intensity between the inner cell bodies and intercellular space (J.W. Cooley and J.W. Tukey, 1965; Gonzalez and Woods, 2002). Firstly, an input image is transformed into a 2D representation of FFT's frequencies, and then a simple band-pass filter is applied to suppress the frequency coefficients below and above a low and high threshold, respectively. The band-pass filter can be obtained by multiplying the filter functions of a low-pass and of a high-pass in the frequency domain, where the low-pass filter has a higher cut-off frequency than that of the high-pass filter. In this work, band-pass high and low cut-off frequencies are set empirically to be 20 and 3, respectively. These cut-off frequencies are attenuating all frequencies smaller than the low frequency and higher than the high frequency, while the frequencies in between remain in the resulting output image. Thus, the noise and slow variations in illumination are eliminated (Smith, 1999; Haque and Uddin, 2011). This is followed by applying the Inverse Fast Fourier Transform (IFFT) to transfer the image back into the spatial domain. In this work, the FFT-Band-pass filter is applied six times, and each time it has observed that cell boundaries are significantly enhanced, especially in the dark regions at the corner of the images. The output of this step is shown in Figure 5.3 (b). Next, an image binarization process is applied using a mean value threshold, which is automatically determined using a grey level histogram of the input image. In this process, all pixels in an endothelial image having intensity values less than the pre-defined threshold, are set to 0 (black pixels), while the rest are set to 1 (white pixels). As shown in

Figure 5.3 (c), the binarized image consists of circular cell markers which are sometimes linked with each other. In this work, these linked markers are separated by applying the watershed approach on top of the Euclidian distance map which is computed from the binarized image, explained in the next subsection.

### 5.2.3 Cell Contour Detection Step

In this stage, an efficient segmentation algorithm based on watershed transformation and Voronoi Tessellation approach is employed to efficiently and automatically detect the endothelial cell boundaries. The watershed transformation approach is applied to the pre-processed image after calculating its Euclidean distance map to automatically separate merged markers obtained from the pre-processed image. The Euclidean distance map has each original black pixel replaced by the value of its distance to the nearest edge pixel to generate a clearer grey level image. Therefore, the centre of each cell is represented by the highest value, as it represents the farthest point from cell borders. This generated Euclidean distance map is then reinterpreted as a topographic map with its pixel values representing altitude which can be easily identified, with mountains, valleys and water catchment regions using the watershed approach, as water flows downhill in any direction from mountains (peaks and ridges) to valleys (lowest points) (Beucher and Lantuejoul, 1979; Beucher and Meyer, 1993). Here, the main aim of the watershed approach is to find the frontiers between the water catchment regions, and then the linked rosary markers in the binarized image are separated using these frontiers

Figure 5.3 (d). In this study, the watershed approach works best with smooth convex objects with less overlapping between them (Meyer, 2012).



**Figure 5.3:** Corneal cell segmentation system outputs: (a) Original corneal image, (b) Applying FFT-Band-pass filtering, (c) Binarized image, (d) Applying watershed approach, (e) Applying Voronoi tessellation, (f) Labeling of endothelial cells (g) Final endothelial cells segmentation result, and (h) Automatically traced endothelial cells boundaries.

The Voronoi Tessellation approach is the second step of the proposed segmentation algorithm, which is applied to the output of the watershed approach in order to produce the final polygonal borders map using the coordinates of the cell centres as an input. Several studies demonstrated the efficiency of the Voronoi Tessellation approach for morphometric cell analysis including corneal endothelium, as in (Kim *et al.*, 2006)(Brookes, 2017). Suppose that an image with a set of circular markers  $M = \{m_1, \dots, m_n\}$ , a Voronoi Tessellation approach divides this image into  $n$  cells, one for each circular marker in  $M$  where each point  $p$  lies in the cell corresponding to a circular marker  $m_i$  if  $\text{dist}(m_i, p) < \text{dist}(m_j, p)$  for  $i$  distinct<sup>2</sup> from  $j$ . The borders of endothelial cells are found by drawing lines of equidistant points between each two nearest circular markers' centres. In other words, these polygons produced from drawing lines around every center marker represent the borders of endothelial cells. In the image produced, the pixel value inside each endothelial cell is set to zero, while the pixel values on the borders of the cells are equal to the distance between the two nearest marked centres, as shown in Figure 5.3 (e-f).

#### 5.2.4 Morphometric Parameters Quantification Stage

At this stage, a number of clinically useful features are extracted from the segmented endothelial cell images in an automated and objective manner to accurately describe the health of the corneal endothelial cells based on quantifying MCD (cell/mm<sup>2</sup>), polymegathism, pleomorphism, MCA ( $\mu\text{m}^2$ ) and MCP ( $\mu\text{m}$ ). These extracted morphological features obtained with the proposed CEAS system are reported as a readable text file (Figure 5.4). Due to the poor

<sup>2</sup> The distance between points is calculated using the Euclidean distance.

quality of the captured images (e.g., some regions are high reflectivity or they are extremely dark and blurred), accurate cell segmentation and estimation of the morphological features in these regions is very challenging, as shown in Figure 5.5 (a). To address this issue and make the analysis more applicable clinically, the proposed system allows an ophthalmologist to choose and crop the clearest ROI in the segmented image. The morphological features are then calculated automatically only for the cropped region, by including cells that intersect only with two adjacent borders of the frame, and excluding those intersecting with other borders. However, if the whole image is used, all the outermost cells are excluded from the statistical calculation to avoid any inaccurately segmented cells on the edge of the input image.

- a) **Mean Cell Density (MCD)** is calculated as the number of endothelial cells ( $C_{number}$ ) in the cropped ROI (or whole image) divided by the total size ( $A$ ) of the cropped ROI (or whole image), as follows:

$$MCD = \frac{C_{number}}{A} \quad (5.1)$$

- b) **Polymegathism (Coefficient of Variation (CV))** is used to describe the variation in the area of the endothelial cells. An increase in the standard deviation ( $SD$ ) of the MCA leads to an inaccurate estimation for the MCD. Hence, an increase in polymegathism leads to a decrease in the accuracy of the estimated MCA (McCarey, Edelhauser and Lynn, 2008). Polymegathism is calculated as follows:

$$Polymegathism = \frac{SD_{cell\ area}}{MCA} * 100 \quad (5.2)$$

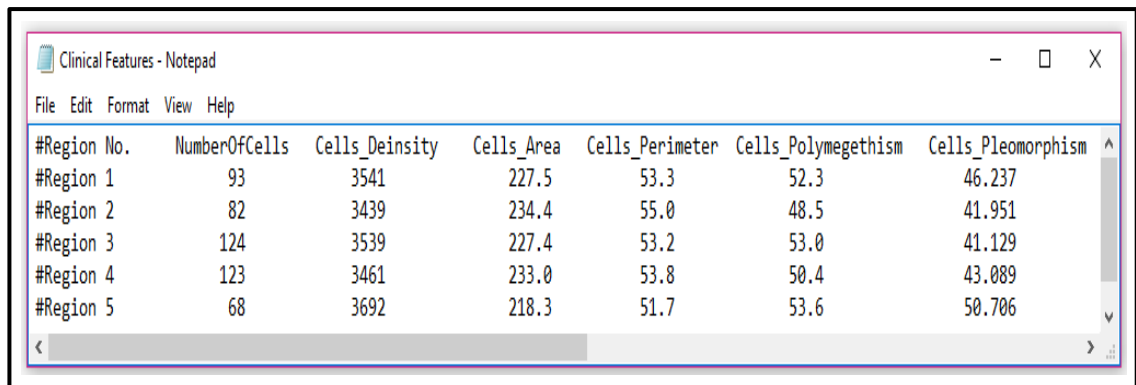
Here,  $SD_{cell\ area}$  is the standard deviation of cell area divided by the MCA.



c) **Pleomorphism (Hexagonality Coefficient (HC))** is calculated as the number of cells with an approximately hexagonal shape (Six-sided)  $C_{hexagonal}$  divided by the total number of cells in the cropped ROI (or whole image)  $C_{image}$ , as follows:

$$Pleomorphism = \frac{C_{hexagonal}}{C_{image}} * 100 \quad (5.3)$$

The endothelial segmented cells image is shown in Figure 5.6 (a). In Figure 5.6 (b) they are shown color coded with all cells with the same number of neighbors filled with the same color. Cells with six sides (roughly hexagonal in shape) are shown in sky blue.



#Region No.	NumberOfCells	Cells_Deinsity	Cells_Area	Cells_Perimeter	Cells_Polymegethism	Cells_Pleomorphism
#Region 1	93	3541	227.5	53.3	52.3	46.237
#Region 2	82	3439	234.4	55.0	48.5	41.951
#Region 3	124	3539	227.4	53.2	53.0	41.129
#Region 4	123	3461	233.0	53.8	50.4	43.089
#Region 5	68	3692	218.3	51.7	53.6	50.706

**Figure 5.4:** A readable text file format showing morphological features associated with the health state of the corneal endothelium.

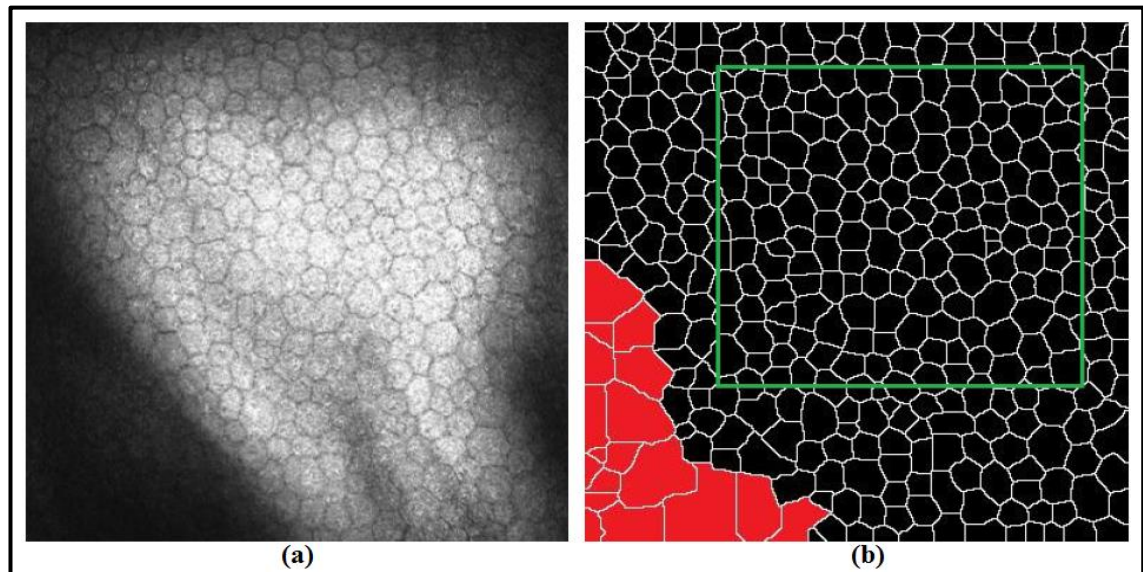


**Figure 5.5:** (a) Original corneal endothelial image and (b) Endothelial cell segmentation results with red color indicating the cells that have been ignored.

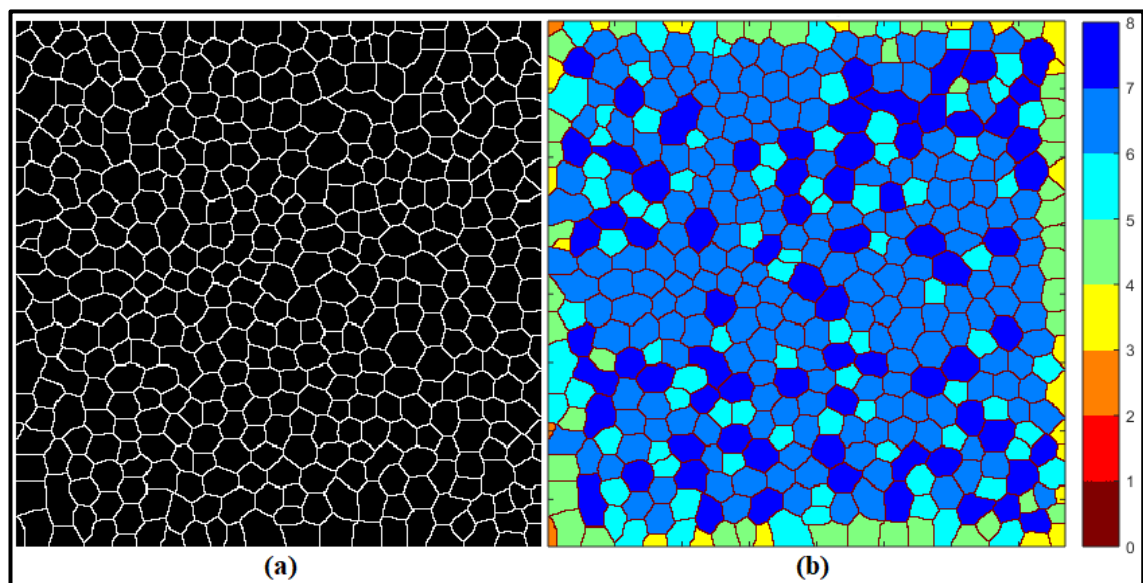


**Figure 5.6:** (a) Final endothelial cells segmentation result and (b) Using the color of a cell to indicate its number of neighbors using the color code given on the right. The most common color is sky blue corresponding to six neighbors.

### 5.3 Experimental Results

A total of 80 images of corneal endothelial cells were acquired using a laser In Vivo CCM to assess the performance of the proposed CEAS system. These images were divided into two databases, named *Database\_1* and *Database\_2*, each one consisting of 40 images. However, due to the lack of availability of a dataset containing manual measurements for all the morphologic parameters obtained from these images, a manual version from each database was obtained by a cornea imaging expert from the University of Manchester using two different programs. In this work, using only *Database\_1*, the performance of the proposed CEAS system was evaluated against an automated system based on KH algorithm (Habrat *et al.*, 2015; Piorkowski *et al.*, 2017). This algorithm is already included in the BestFit<sup>3</sup> system. The KH algorithm starts by reducing the effects of the noise and non-uniform illumination in endothelial images using a binary filter of size (5×5) pixels. This is followed by applying the binarization process using four morphological operators of size (9×9) pixels; two of them were rotated by 45° and the remaining two by 90°. As a result, four different binary images were obtained by convolving the original image with these four filters. Finally, these four images were fused together to produce the final output after removing all the objects smaller than 40 pixels, which probably correspond to cell nuclei. For a fair comparison, the same parameters of the KH algorithm described in (Piorkowski *et al.*, 2017) are used in this study. Initially, the performance of the proposed CEAS system was evaluated on *Database\_1*, where an open-source GNU

---

<sup>3</sup> [home.agh.edu.pl/~pioro/bestfit](http://home.agh.edu.pl/~pioro/bestfit)

Image Manipulation Program (GIMP)<sup>4</sup> was used to manually trace cell contours and create a binary image from selected ROIs with a manual estimation of the morphometric parameters, as shown in Figure 5.7. Using *Database\_1*, two experiments were conducted to assess the accuracy of the proposed CEAS system. In the first experiment, the performance of the proposed segmentation algorithms were evaluated against the ground-truth reference images (binary images) generated using GIMP software Figure 5.7 (c). The evaluation procedure is based on the computation of the seven quantitative performance measures: Probabilistic Rand Index (PRI) (Kaur, Agrawal and Vig, 2012), Structural SIMilarity (SSIM) Index (Wang *et al.*, 2004), Variation of Information (Vol) (Meilă, 2007), Global Consistency Error (GCE) (Martin *et al.*, 2001), Gradient Magnitude Similarity Deviation (GMSD) (Xue *et al.*, 2014), Mean Square Error (MSE), and Normalized Absolute Error (NAE) (Mallikarjuna, Satya Prasad and Venkata Subramanyam, 2016). Four of these measures (PRI, SSIM, Vol, and GCE) have been explained in chapter 3. These full-reference quantitative metrics are widely employed in literature for assessing the efficiency and accuracy of segmentation systems and are defined as follows:

1. **The GMSD** is an image quality assessment method which computes the Local Quality Map (LQM) by locally comparing the gradient magnitude maps of segmented image  $X$  and ground-truth image  $Y$ . This is followed by applying the standard deviation of LQM as the pooling strategy to produce the final quality score, as follows:

$$GMSD = \sqrt{\frac{1}{N} \sum_{i=1}^N (GMS(i) - GMSM(i))^2} \quad (5.4)$$

<sup>4</sup> <https://www.gimp.org/> .

where,  $\mathbf{N}$  is the total number of pixels in the image, GSM represents the mean of the GMS map, which is computed in a pixel-wise manner using the gradient magnitude images  $\mathbf{m}_x$  and  $\mathbf{m}_y$ , as follows:

$$GMS(\mathbf{i}) = \frac{2\mathbf{m}_x(\mathbf{i}) * \mathbf{m}_y(\mathbf{i}) + \mathbf{c}}{\mathbf{m}_x^2(\mathbf{i}) + \mathbf{m}_y^2(\mathbf{i}) + \mathbf{c}} \quad (5.5)$$

Here,  $\mathbf{c}$  is a small constant that provides numerical stability. The GSM value represents a distortion index, thus a lower GSM value indicates higher quality.

**2. The MSE** is one of the most widely used image quality measurement metric, defined as the sum over all squared value pixel differences divided by the size of the image, where a lower value of MSE indicates a higher similarity. The MSE between the segmented image  $\mathbf{X}$  and the ground-truth image  $\mathbf{Y}$  of equal size ( $\mathbf{M} \times \mathbf{N}$ ) pixel is defined as follows:

$$MSE = \frac{1}{MN} \sum_{m=1}^M \sum_{n=1}^N (X(m, n) - Y(m, n))^2 \quad (5.6)$$

**3. The NAE** between the segmented image  $\mathbf{X}$  and the ground-truth image  $\mathbf{Y}$  both of size ( $\mathbf{M} \times \mathbf{N}$ ) pixel is given in Eq.5.7, where a lower NAE points to a higher similarity.

$$NAE = \frac{\sum_{m=1}^M \sum_{n=1}^N |(X(m, n) - Y(m, n))|}{\sum_{m=1}^M \sum_{n=1}^N |X(m, n)|} \quad (5.7)$$

The overall average of the seven quantitative metrics is computed for 40 images in this database, as shown in Figure 5.8. Although the KH algorithm has achieved a better result in terms of GSM measure compared to the proposed CEAS system, it obtained inferior results on the other six quantitative measures.

Figure 5.9 shows a comparison between manual and automated segmentation output images obtained from both the proposed CEAS and KH algorithm. A better result was obtained using the proposed CEAS system. The KH algorithm suffers from over-segmentation, due to low quality input image and the presence of noise. Significantly, the results obtained demonstrate the efficiency and reliability of the proposed CEAS system and the potential for using it as a fully-automatic system to accurately trace cell contours and measure the morphometric parameters for clinical diagnostic purposes. This is made the possibility of using it as a diagnostic tool because of the high similarity rates obtained between the automatically segmented images and the manually traced images.

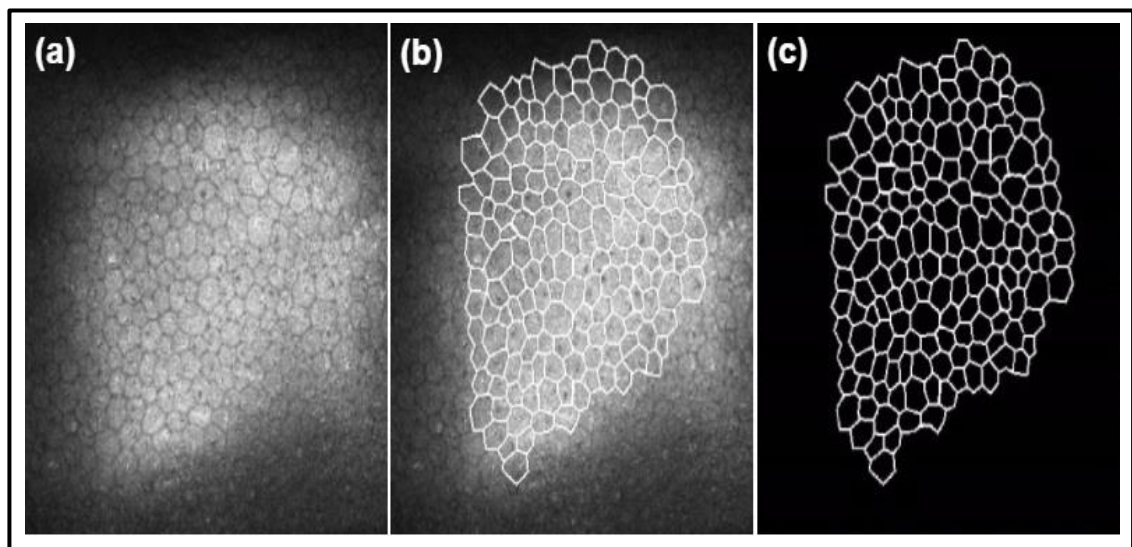


**Figure 5.7:** GIMP program outputs: (a) Original image, (b) A representative example of manually traced cells contours, (c) Generated binary image used as a ground-truth manual segmentation inside the ROI.

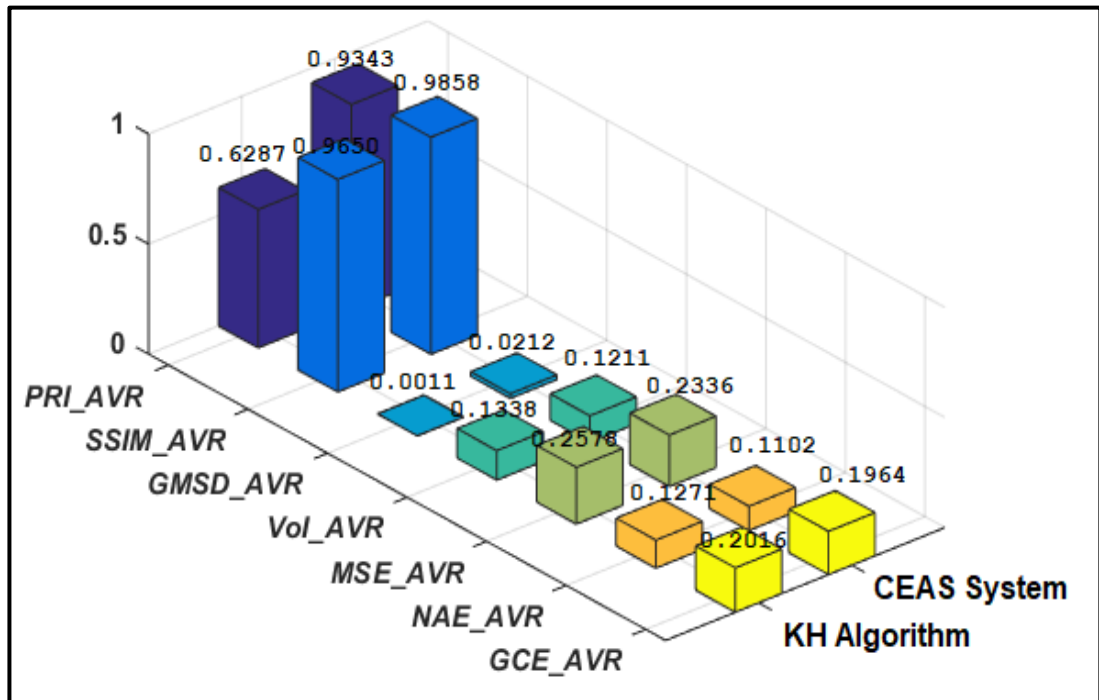


**Figure 5.8:** Performance comparison of the CEAS segmentation system and the KH algorithm on *Database\_1*, where a higher value of PRI and SSIM is better and a lower value of GMSD, Vol MSE, NAE and GCE are better.

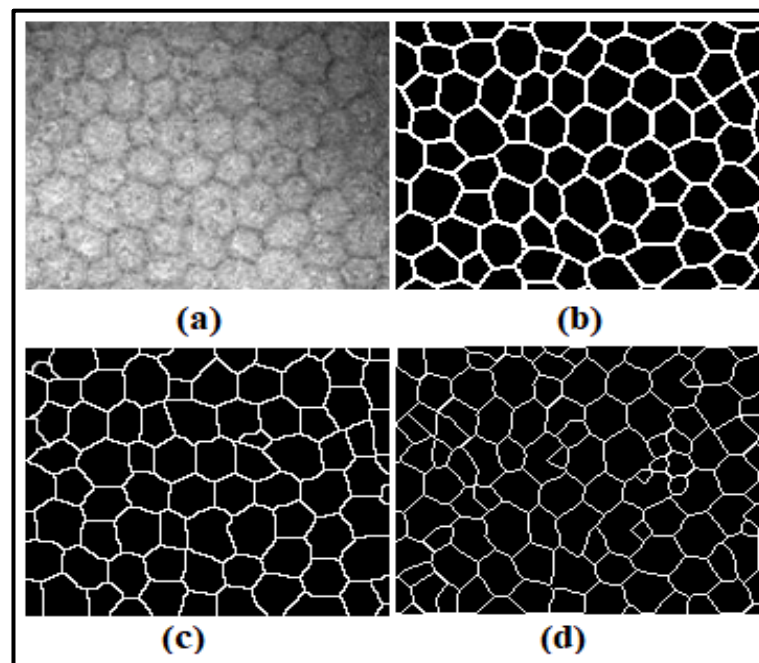


**Figure 5.9:** A comparison example of an image taken from the *Database\_1*: (a) Original image, (b) A manually traced cell contours, (c) The output of the proposed CEAS system, and (d) The output of the KH algorithm.

Here, it is important to note that most of the segmentation approaches and commercially available image software systems (e.g., GIMP) are edge-based segmentation approaches, whereas in this study an alternative region-based segmentation approach based on the Voronoi Tessellation is employed to accurately extract size and shape data of the endothelial cells. In this work, using the Voronoi Tessellation, as a region-based segmentation approach ensures that a wider range of corneal endothelial parameters can be derived and analyzed than edge-based segmentation approaches, by dividing the surface of the endothelial image into different regions (Voronoi cells) based on the distance to the cell markers' centres. In addition, the Voronoi Tessellation approach produces straight-borders of cells of optimum size and shape compared to the edge-based segmentation approaches, which produce cell shapes composed of non-uniform curves. This enhances the reliability of the proposed CEAS system in calculating polymegathism and pleomorphism data of the endothelial cells (Reem, 2011). Finally, as reported by (Reem, 2011), the Voronoi Tessellation approach provides a high degree of geometric stability with respect to small changes in the position of the cell markers' centres, with only a small change in the corresponding Voronoi cells.

In the second experiment, a clinical evaluation procedure was performed to assess the robustness and effectiveness of the CEAS system in term of extracting useful morphometric parameters. This clinical-based evaluation procedure has been done by ophthalmologists from Division of Medicine, Weill Cornell Medicine-Qatar, Doha, Qatar and the Manchester Royal Eye Hospital, Centre for Endocrinology and Diabetes, UK. Automatic estimations of five morphometric parameters (e.g., MCD, MCA, MCP, Polymegathism, and



Pleomorphism) were compared with reference values, which were calculated by simply applying the definition of these parameters on 40 binary images generated using GIMP software, as shown in Figure 5.7 (c).

The proposed CEAS system and KH algorithm were applied to every corneal endothelial image, and then the same ROI with the largest area of clearly visible cells was selected. Next, automatic estimations of morphometric parameters were computed for the ROI from both images and directly compared with the reference values. The overall average, standard deviation, maximum and minimum of each parameter for both manual and automated images, along with the difference and the percentage difference between them are reported in Table 5.1. From this table, it can be seen that the proposed CEAS system has achieved noticeably a higher agreement with reference values compared to the KH algorithm. The average difference between manual and automatic estimations computed by the KH algorithm was less than 3.5%, 11%, 9.5%, 6.5%, and 11% for MCD, MCA, MCP, polymegathism, and pleomorphism, respectively. In contrast, no significant differences were found between manual and automatic estimations of morphometric parameters computed by the proposed CEAS system. The average differences between manual and automatic estimations were less than 2%, 3.5%, 1%, 1.5%, and 8.5% for MCD, MCA, MCP, polymegathism, and pleomorphism, respectively, with no morphometric parameter with a relative difference ( $>10\%$ ) between the manual and automatic estimations.

Pearson correlation tests were used to confirm clinical validity and usefulness of the proposed CEAS system as an effective tool to provide an accurate and automatic estimation of the endothelial cell parameters. There

were statistically significant correlations between the automated and manual estimations of morphometric parameters with Pearson's correlation  $r$  and  $p$  coefficient of: ( $r = 0.91$ ,  $p < 0.0001$ ) for MCD, ( $r = 0.91$ ,  $p < 0.0001$ ) for MCA, ( $r = 0.82$ ,  $p < 0.0001$ ) for MCP, ( $r = 0.85$ ,  $p < 0.0001$ ) for polymegathism, and ( $r = 0.74$ ,  $p < 0.0001$ ) for pleomorphism, as shown in Figure 5.10. Bland–Altman plots of differences versus means for all the morphometric parameters were generated to assess agreement between the automated analysis and manual analysis (Figure 5.11).

**Table 5.1:** Performance comparison made between the manual and automated estimations of five morphometric parameters using the CEAS system and KH algorithm on 40 corneal images of *Database\_1*. The differences between the manual and automatic estimates are listed and also as a percentage.

	Manual	Auto. CEAS System		Auto. KH algorithm			
	MCD (cells/mm <sup>2</sup> )	MCD (cells/mm <sup>2</sup> )	Diff	Diff %	MCD (cells/mm <sup>2</sup> )	Diff	Diff %
<b>Average</b>	3103.52	3047.25	56.27	1.83	2997.89	105.6	3.46
<b>STD</b>	389.54	308	81.54	23.35	299.32	90.22	26.19
<b>Max</b>	3760	3640	120	3.24	3574	186	5.07
<b>Min</b>	2243	2482	-239	-10.1	2298	-55	-2.42
	MCA (μm <sup>2</sup> )	MCA (μm <sup>2</sup> )	Diff	Diff %	MCA (μm <sup>2</sup> )	Diff	Diff %
<b>Average</b>	292.3	282.43	9.87	3.43	263	29.3	10.55
<b>STD</b>	41.77	34.57	7.2	18.87	33.78	7.99	21.15
<b>Max</b>	395	386	9	2.3	373	22	5.72
<b>Min</b>	229	220	9	4	200	29	13.52
	MCP (μm)	MCP (μm)	Diff	Diff %	MCP (μm)	Diff	Diff %
<b>Average</b>	61.5	61	0.5	0.78	56	5.5	9.36
<b>STD</b>	4.61	3.52	1.09	26.8	2.98	1.63	42.95
<b>Max</b>	74	70	4	5.56	65	9	12.94
<b>Min</b>	55	54	1	1.83	48	7	13.59
	Polymegathism %	Polymegathism %	Diff	Diff %	Polymegathism %	Diff	Diff %
<b>Average</b>	46.5	45.95	0.55	1.02	43.7	2.80	6.20
<b>STD</b>	5.96	4.68	1.28	24.09	3.71	2.25	46.53
<b>Max</b>	61	59	2	3.33	53	8	14.84
<b>Min</b>	36	37	-1	-2.74	31	5	14.92
	Pleomorphism %	Pleomorphism %	Diff	Diff %	Pleomorphism %	Diff	Diff %
<b>Average</b>	37.45	34.5	2.95	8.21	33.7	3.75	10.54
<b>STD</b>	5.84	4.83	1.01	18.84	4.47	1.5	26.57
<b>Max</b>	50	47	3	6.2	44	6	12.76
<b>Min</b>	24	25	-1	-4.1	22	2	8.69

The proposed CEAS system produces an accurate estimation for detecting endothelial cells with more than 95% of the data presented between 2SD agreement lines, and cell densities ranging from 2400 to 3700 (cell/mm<sup>2</sup>), cell area ranging from 230 to 400 (μm<sup>2</sup>), cell perimeter ranging from 50 to 75 (μm), polymegathism ranging from 35 to 40%, and pleomorphism ranging from 25 to 50%. Figure 5.12 shows a comparison between manual and automated segmentation output images, where the incorrectly detected cell boundaries are marked in red color.

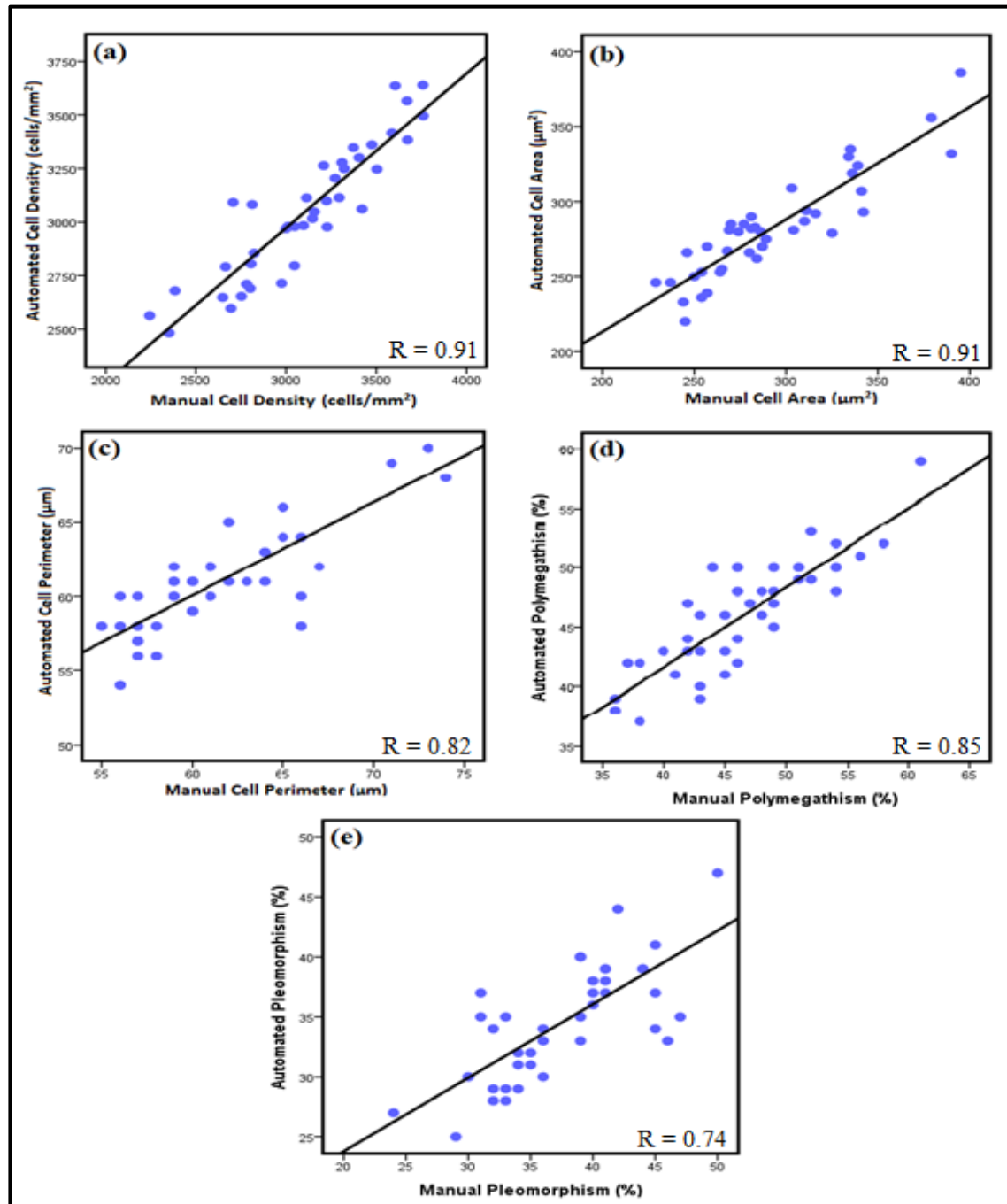


**Figure 5.10:** Correlation plots for each pair of manual and automatic morphometric parameters from *Database\_1*, showing significant correlations. The solid lines are the linear regression lines: (a) Cell density, (b) Cell area, (c) Cell perimeter, (d) Polymegathism, and (e) Pleomorphism.

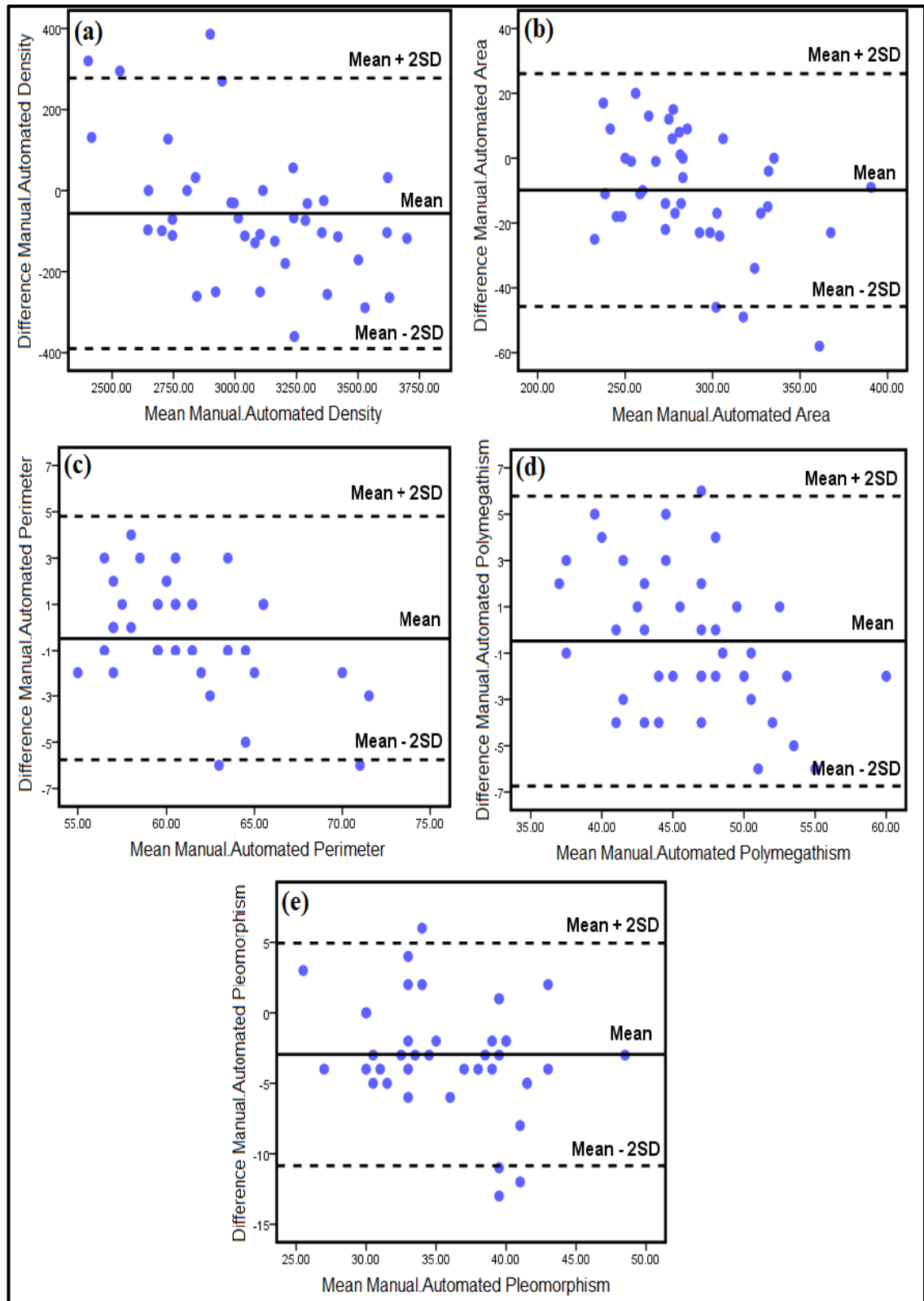


**Figure 5.11:** Bland-Altman plots showing difference versus average for each pair of manual and automatic estimations of: (a) Cell density, (b) Cell area, (c) Cell perimeter, (d) Polymegathism, and (e) Pleomorphism from *Database\_1*. Solid lines (mean differences), dashed lines (95% limits of agreement).

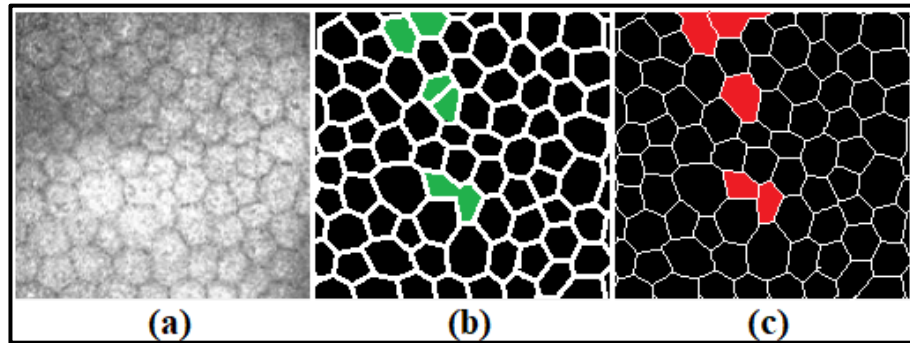


**Figure 5.12:** Comparison between manual and automated segmentation outputs: (a) Original image, (b) Manually traced cells, (c) Automatically segmented cells.

Further evaluation was performed on an independent database, named Database\_2 in which a manual database containing 40 images (11 from control subjects, 16 from obese subjects and 13 from patients with diabetes) was constructed to efficiently validate the performance of the proposed corneal cell segmentation and quantification system. The cell densities were manually counted by experts from (Division of Medicine, Weill Cornell Medicine-Qatar, Doha, Qatar and the Manchester Royal Eye Hospital, Centre for Endocrinology and Diabetes, UK) using a semi-automatic system (cell count feature) offered by the HRT Rostock Cornea Module (Heidelberg Engineering GmbH; Heidelberg; Germany). In the manual measurements, the user selects the clearest ROI from the original corneal endothelial image and then crops it. After magnifying the cropped region to make it easier to view, the user picks the cells using the count function and the MCD is calculated according to the number of cells within the given ROI. A snapshot of this semi-automatic system is shown in Figure 5.13.

These manual cell densities were compared with automatically computed cell densities using the CEAS system for the same ROI. The results demonstrate the ability of the proposed CEAS system to detect corneal endothelial cells effectively in clinical real-time, with an execution time of about 6 seconds per image using a PC with a Windows 8.1 operating system, a 1.80 GHz Core i5-3337U CPU and 6 GB of RAM. The system code was written in MATLAB R2015a. The main reason for differences between the manual and automated cell densities is the loss of image quality at the borders of the images, and there may be some cells in the cropped ROI, which are over selected in the manual image or are not picked at all Figure 5.14.

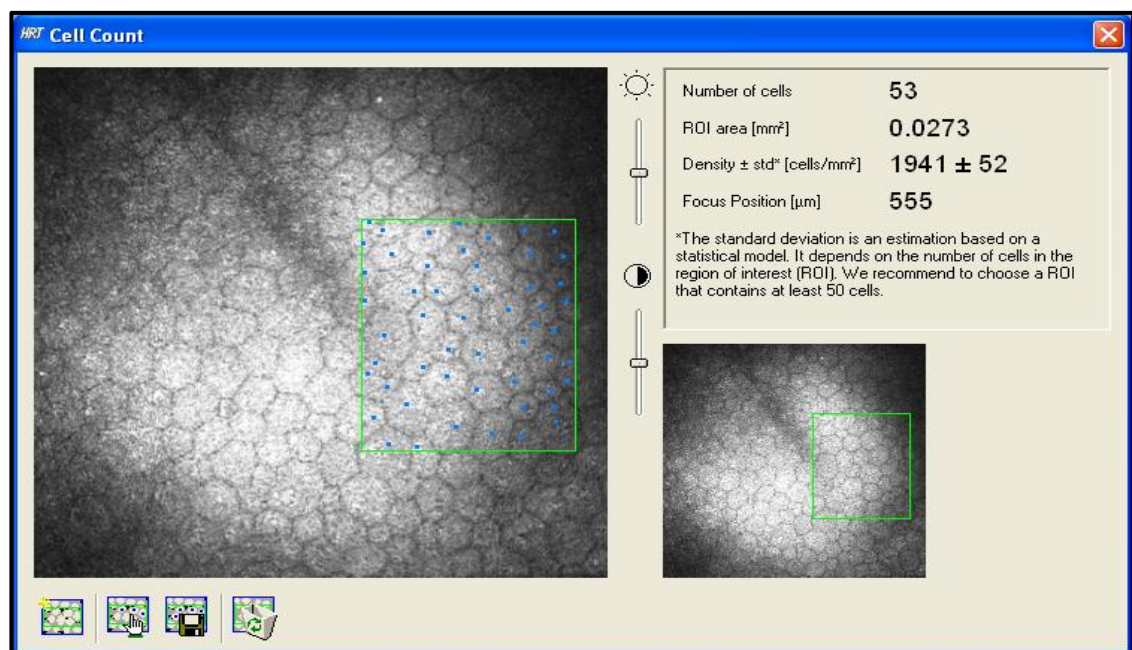


**Figure 5.13:** An illustration of the semi-automatic corneal endothelium system used in the HRT Rostock Cornea Module (Heidelberg Engineering GmbH; Heidelberg; Germany) for cell density estimation.

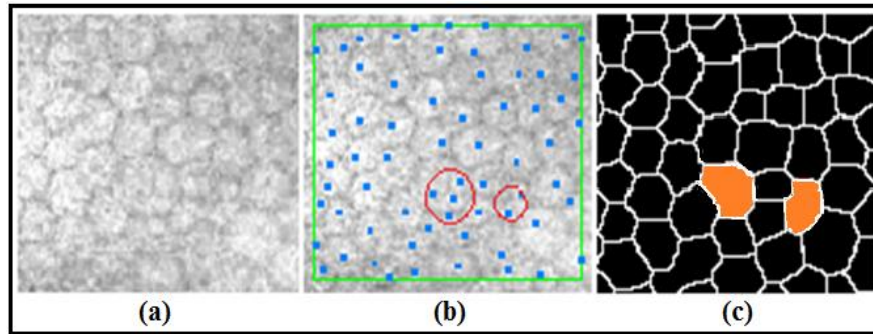


**Figure 5.14:** (a) Original image, (b) Manually over picked cells as shown in the red circle, (c) Automatically segmented cells.

As shown in Table 5.2, there was no significant difference in manual compared with automated endothelial cell density and the average difference was less than 2%. There was a highly significant correlation between automated and manual densities ( $r = 0.9$ ,  $p < 0.0001$ ), as shown in Figure 5.15. The proposed segmented endothelial cell detection algorithm provides a precise estimation for detecting endothelial cells with cell densities ranging from 2000 to 5000 (cells/mm<sup>2</sup>) and the Bland-Altman method shows that 95% of data are presented between 2SD agreement lines. Based on the agreement plot the difference between the two methods is larger when the density is higher (Figure 5.16).

The results obtained demonstrate the effectiveness and robustness of the proposed CEAS system, and its suitability to be used as a fully automatic cell segmentation system to provide useful clinical information for early diagnosis and monitoring of the corneal endothelium over time and in relation to the effect of therapies, by achieving a high similarity between the cell density obtained automatically and the cell density obtained manually. The GUI of the proposed CEAS system is shown in Appendix C.



**Table 5.2:** Performance comparison between the manual and automated cell density estimates using *Database\_2*.

	<b>Manual MCD (cells/mm<sup>2</sup>)</b>	<b>Auto. MCD (cells/mm<sup>2</sup>)</b>	<b>Diff</b>	<b>Diff %</b>
<b>Average</b>	3390.18	3343.65	46.53	1.38
<b>STD</b>	715	415	300	53.01
<b>Max</b>	4960	4247	713	15.49
<b>Min</b>	1941	2473	-532	-24.1

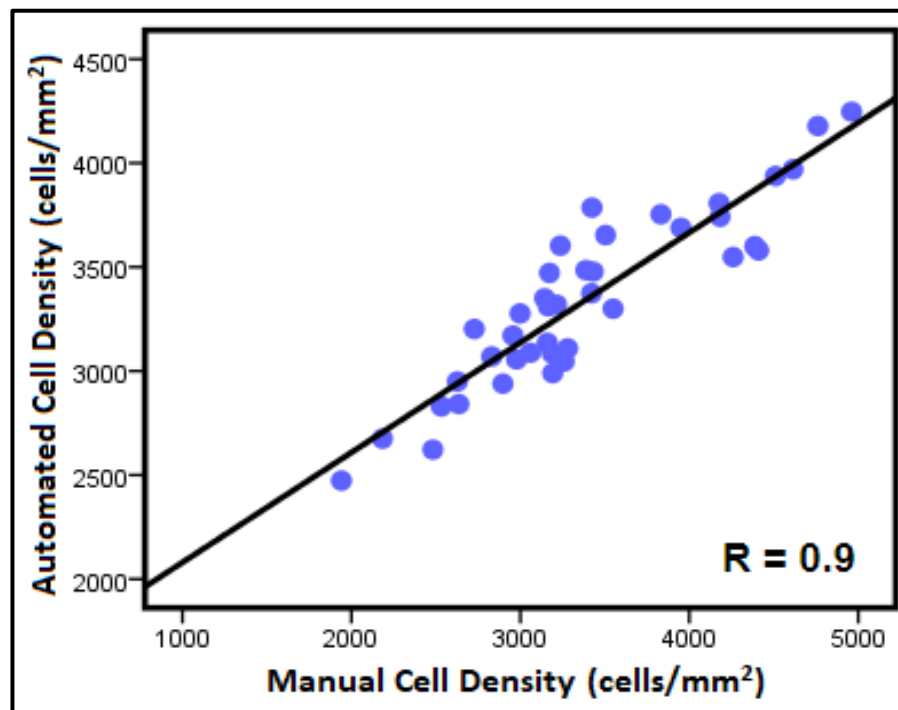


**Figure 5.15:** Correlation plot of automated and manual cell densities with a significant correlation on *Database\_2*.

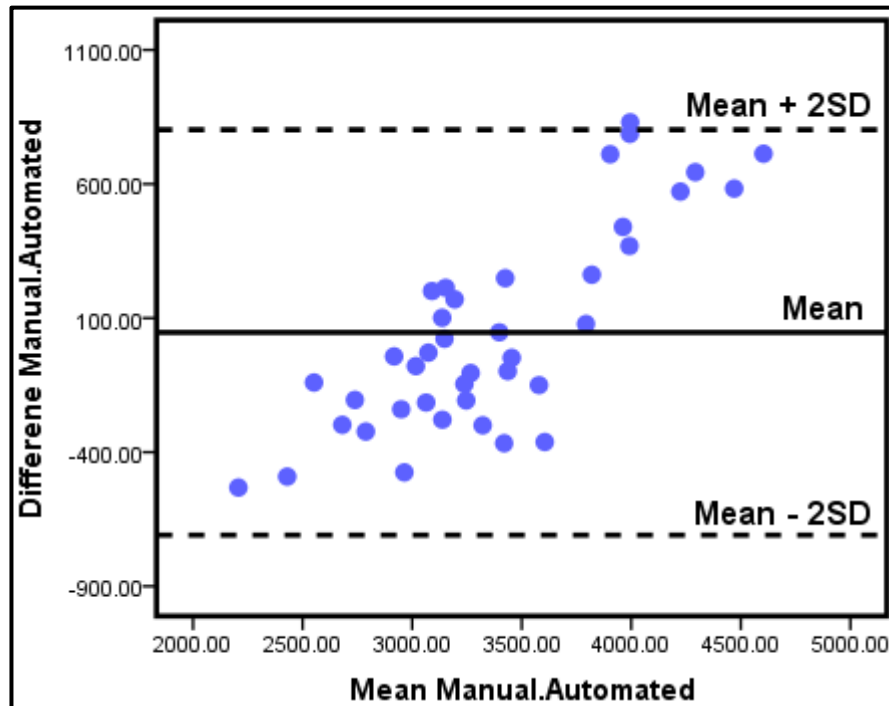


**Figure 5.16:** Bland-Altman plot showing mean difference and limits of agreement between manual and automated cell densities on *Database\_2*.

## 5.4 Summary

In this study, a real-time and fully-automated endothelial cell segmentation and morphological parameter quantification system is proposed, named the Corneal Endothelium Analysis System (CEAS) which requires no user intervention. In the CEAS system, band-pass filter was applied for noise reduction to enhance image quality and endothelial cell boundaries were detected using the watershed approach and Voronoi tessellations enabling quantification of endothelial cell density and additionally cell area, cell perimeter, polymegathism and pleomorphism. In this work, an alternative region-based segmentation approach, namely the Voronoi Tessellation approach is employed to accurately extract meaningful information from the endothelial cells (e.g., size and shape data), and enable the proposed CEAS

system to produce a wider range of corneal endothelial parameters. Unlike other edge-based segmentation approaches, the Voronoi Tessellation approach has the ability to produce straight-borders of cells with an optimum size and shape. Furthermore, it ensures a high degree of geometric stability with respect to small changes in the position of the cell markers' centres.

The performance of the proposed CEAS system was evaluated and tested against manually traced ground-truth images of two databases; each one contains a total of 40 images. The results obtained demonstrate the effectiveness and robustness of the proposed CEAS system, and its suitability to be used as a fully automatic cell segmentation system to provide useful and helpful clinical information for early diagnostic purposes and monitoring the corneal endothelium health status, by achieving a high similarity between automatically and manually clinical features.

## Chapter 6

# Conclusions and Future Work

In this PhD research, robust and fully-automated systems for segmenting corneal sub-basal nerves and corneal endothelial cells in human CCM images have been proposed. After reviewing and analyzing the current state-of-the-art works on tracing the epithelium nerves and detecting endothelial cells boundaries, a number of efficient and robust algorithms have been proposed. This includes proposing practical algorithms to improve the quality of the CCM images, novel and fully-automated tracing algorithms for the epithelium nerves and endothelial cells as well as extracting useful morphometric parameters of these two corneal layers. This chapter briefly summarizes the research work presented in chapters 3, 4 and 5, draws conclusions and emphasizes the main contributions made by the research presented in this thesis. Then, some of the suggestions and recommendations to be addressed in future work are outlined in order to further enhance the performance and increase the reliability of the proposed systems in analysing the CCM images, and the intention of further extending the functionality and efficiency of the proposed algorithms.

### 6.1 Conclusions

The main motivation to the research presented in this thesis originated from a number of requests that were made by medical practitioners working in the areas of Ophthalmology and diagnosis of peripheral neuropathy and other pathological changes in human corneas. Therefore, the main aim of this PhD research was to develop a system for the automatic processing and analysis of

CCM images of the various layers of the cornea. This aim has been achieved by developing effective and efficient systems for segmenting sub-basal epithelium nerves and endothelial cells in human corneal confocal microscopy images were proposed to help ophthalmologists in monitoring and treating the different corneal diseases early and efficiently. Setting off from the aims and objectives stated in chapter one, this research has addressed the following:

1. The quality of the CCM images has been improved significantly by enhancing these images and reducing the effect of non-uniform illumination. For corneal sub-basal nerves images, the visibility of the corneal sub-basal nerve has been improved and the amount of the noise in the corneal image has been reduced using anisotropic diffusion filtering, specifically a Coherence filter followed by Gaussian filtering. Here, it is worth mentioning that the output of the Coherence filter is affected by the value set to the Diffusion Time parameter. Although this pre-processing procedure has significantly enhanced the structure of the corneal nerve without losing important information, the produced image still has some false artefacts due to non-uniform illumination in corneal images and the presence of unwanted segments (e.g. small cells). In this work, this issue has been addressed by applying an efficient post-processing procedure mainly based on morphological operations to accurately describe nerve structure by removing imperfections without affecting the overall shape of the nerve. In contrast, the quality of the endothelial cell images has been improved and the amount of the noise has been reduced using an band-pass filter. In this work, the band-pass filter has attenuated very low and very high frequencies by employing two cut-off frequencies, and retained

middle range frequency band. Thus, band-pass filtering has enhanced the visibility of the cell borders and reduced the amount of the noise at the same time by suppressing low frequencies and attenuating high frequencies, respectively.

2. The second and third objectives were to develop a fully automatic, efficient, real-time corneal sub-basal epithelium nerve segmentation and morphological parameter quantification system. In this segmentation stage, an efficient nerve connection procedure was proposed in order to connect the discontinuous nerves, caused by the low visibility of parts of the nerves or noise introduced into the corneal images. Although in some cases, corneal nerves have been incorrectly connected with each other due to the detection of more than one endpoint inside the circular region, this procedure has significantly improved the accuracy of extracting helpful and meaningful clinical features that mainly depend on the whole structure of the nerve in their calculations, such as nerve tortuosity and nerve length. In the morphometric parameters quantification stage, a number of useful clinical features, such as nerve tortuosity, thickness, length, density as well as nerve perimeter, nerve area and the image intensity were also calculated for internal use. In this part, a new algorithm based on applying the distance transform on the binary segmented image to efficiently and accurately compute the nerve thickness parameter, without any manual intervention, is also proposed. The performance of the proposed system was evaluated using two databases of CCM images taken from different groups of subjects (e.g., healthy subjects and diabetic patients). The results obtained have demonstrated the reliability and efficiency of the

proposed segmentation system and the potential to use it as a real-time and a fully automatic nerve tracing system in patients with DPN as an early diagnostic and for follow-up. The limitation of the proposed corneal nerve segmentation system is that its performance has been evaluated using CCM images taken from just the healthy and diabetic patients with and without neuropathy. Therefore, the efficiency of the proposed corneal nerve segmentation system in extracting usefulness clinical features should also be validated on a database contains CCM images with other corneal disease, such as acute ischemic stroke. Recently, a number of studies have shown that patients with acute ischemic stroke also had a reduction in corneal nerve fibres, as found in (Khan et al. 2017). Furthermore, the proposed nerve segmentation algorithm has the potential to be successfully used in the detection and analysis of the retinal blood vessels. However, investigations carried out within the research context of this PhD research have shown that CCM images are extremely different and very lower quality compared to retinal images, which are captured under more controlled environmental conditions, using high-resolution cameras.

3. The author has also proposed an automatic corneal sub-basal nerve registration system using an FFT based phase correlation technique. In this system, the best common features between a number of sequenced CCM images in the frequency domain were found using the proposed image registration method to produce a more informative corneal image than the original images. This is followed by generating a colour coded corneal image map from the latest registered corneal image. In this

coloured map, the severity level of a specific clinical feature is represented by a specific colour code that can be used to give the ophthalmologist a clear representation of the extracted clinical features from each nerve in the image map. Furthermore, it can also help them to produce faster and more meaningful information relating to the DPN severity. The main limitation was the lack of an available large-scale database that contains a higher number of CCM image sequences to validate the performance of the proposed corneal nerve image registration system. However, we believe that our findings confirm and validate the usefulness of the generated corneal image map as a more informative corneal image that contains better structural and functional information compared to the original images. We have also managed to significantly reduce the time required for an ophthalmologist to accurately compute useful clinical features where the execution time starting from the image registration stage to generating the colour coded map is about 10 seconds, as demonstrated in Chapter 4.

4. Regarding the fifth objective, a real-time and fully-automated corneal endothelium cells segmentation and morphological parameter quantification system named the Corneal Endothelium Analysis System (CEAS) which requires no user intervention has been proposed. In this PhD Thesis, the watershed approach and Voronoi tessellations are applied to efficiently detect endothelial cell boundaries and enable the quantification of some helpful and meaningful morphometric parameters, including endothelial cell density, endothelial cell area, endothelial cell perimeter, polymegathism and pleomorphism. The watershed approach



applied in the present study is different from that applied in the literature. For example, to compute the stochastic watershed, the seeded watershed was applied 100 times to the input image with seeds randomly placed over the image, as in the study presented in (Selig et al. 2015). In contrast, such a procedure is not required in the current study, making the CEAS system simpler to implement. Furthermore, one of the most novel aspects of the proposed system is employing a region-based segmentation approach based on the Voronoi Tessellation approach to accurately extract size and shape data of the endothelial cells. Unlike other previous researches carried out in this area, which are mainly based on edge-based segmentation approaches. In this work, using the Voronoi Tessellation ensures that a wider range of corneal endothelial parameters can be derived and analyzed than edge-based segmentation approaches, as described in Chapter 5. Furthermore, straight-borders of cells of optimum size and shape are produced by employing the Voronoi Tessellation approach compared to cell shapes composed of non-uniform curves that can be produced using the edge-based segmentation approaches. The performance of the proposed CEAS system was evaluated and tested by extracting clinical features from two databases (each one consisting of 40 images), and comparing with 'ground-truth' derived by manually detecting the cell contours aided by two difference programs on the same ROI with an average difference of less than 2%, 4%, 1%, 1.5%, 8% for MCD, MCA, MCP, polymegathism, and pleomorphism, respectively. The findings suggest that the proposed CEAS system could also be useful for ophthalmologists in a real-world clinical

setting to enable rapid diagnosis and patient follow-up. However, the current research has tended to focus only on evaluating the reliability of the proposed CEAS system in automatically detecting endothelial cells boundaries rather than testing its capability for providing meaningful information relating to the different groups (e.g., healthy subjects and diabetic patients), due to the lack of available database that contains subjects with aged-matched. The age factor is a very important factor as it directly affects the cell density. Recently, a number of studies have demonstrated that there exist a statistically significant decrease in MCD and pleomorphism with age, whereas there is a significant increase in MCA with increasing age (Hatipoglu et al. 2014). Therefore, the author believes that the efficiency of the proposed CEAS system in extracting useful clinical feature should also be validated on a database that contains subjects with some medical conditions, such as Type 1 diabetes and subjects with Type 2 diabetes and retinopathy.

5. Finally, to conclude, the proposed work in this PhD research is tackling the real challenges of confocal corneal epithelium and endothelium images and it is done in collaboration with an expert advisory board from the following institutes:

- Division of Medicine, Weill Cornell Medicine-Qatar, Doha, Qatar.
- Manchester Royal Eye Hospital, Centre for Endocrinology and Diabetes, UK.
- Centre for Endocrinology and Diabetes, UK.

## 6.2 Future Work

Although a number of novel contributions in segmenting sub-basal epithelium nerves and endothelium cells in human corneal confocal microscopy images have been proposed in this thesis it is possible to consider further suggestions to be carried out in particular aspects. In this section, several possible directions for future research are discussed as follows:

1. The results derived in the study presented in Chapter 3, are dependent on the successful connection of endpoints with neighbouring endpoints or branching nerves. As a future enhancement will be needed by deploying larger circular regions to search for neighbouring endpoints/nerve regions and use decision-making support (e.g., minimum Euclidean Distance) to tackle situations where more than one endpoint are being detected inside the circular region.
2. In the study presented in Chapter 3, the extracted clinical parameters were compared individually in all subjects to establish the efficiency of the imaging modules developed in this work. However, successful diagnosis requires building general profiles for every subject by combining their available clinical information. Hence, a future research direction should include developing an automated machine learning-based system for diagnosing and differentiating control subjects from diabetic patients with and without neuropathy. To do so, build a learning module from the databases used in this research and feed them with the 4 additional parameters extracted from every subject (e.g., average nerve tortuosity, average nerve thickness, average nerve length and average nerve density) will be needed to create a more comprehensive morphological

phenotype in every subject, which we anticipate could lead to a more reliable diagnosis and stratification of severity of DPN.

3. The performance of the proposed nerve segmentation algorithm presented in Chapter 3 is only limited to detect the nerve structures within the CCM images; it might be interesting to investigate its potential for detecting nerves in other parts of the human body using different types of medical images that contain blood vessels/nerves of similar structures. In this regard, an initial test to the performance of the proposed nerve segmentation algorithm to efficiently detect the retinal nerve fibres within the Indocyanine Green Chorioangiography (ICG) images was conducted and the results obtained are shown in Figure 6.1.
4. The performance of proposed corneal epithelium registration system presented in Chapter 4, should be tested using a larger database that contains a higher number of CCM image sequences to demonstrate the efficiency of the generated image map in providing useful clinical features, such as the nerve tortuosity, nerve thickness, nerve length, etc. Furthermore, the image registration approach proposed in this study could be applied to other medical and biological systems that mainly based on an alignment of a sequence of different type of corneal images. For instance, it has been found recently that detecting *Acanthamoeba* cysts and calculating the depth of each detected cyst in a sequence of confocal microscopy images can help ophthalmologists in the early diagnosis and treatment of the *Acanthamoeba* keratitis, as demonstrated in (Alzubaidi 2017).

5. The results obtained using the proposed CEAS system are promising and encouraging to develop an automated machine learning system for the early diagnosis of endothelial cell abnormalities. To achieve this goal, a larger database needs to be employed in order to construct a learning-based module and feed it with the 5 morphometric parameters extracted from each subject to produce a more comprehensive morphological feature vector for each subject, which we expect could lead to a more reliable diagnosis and confirm our findings.

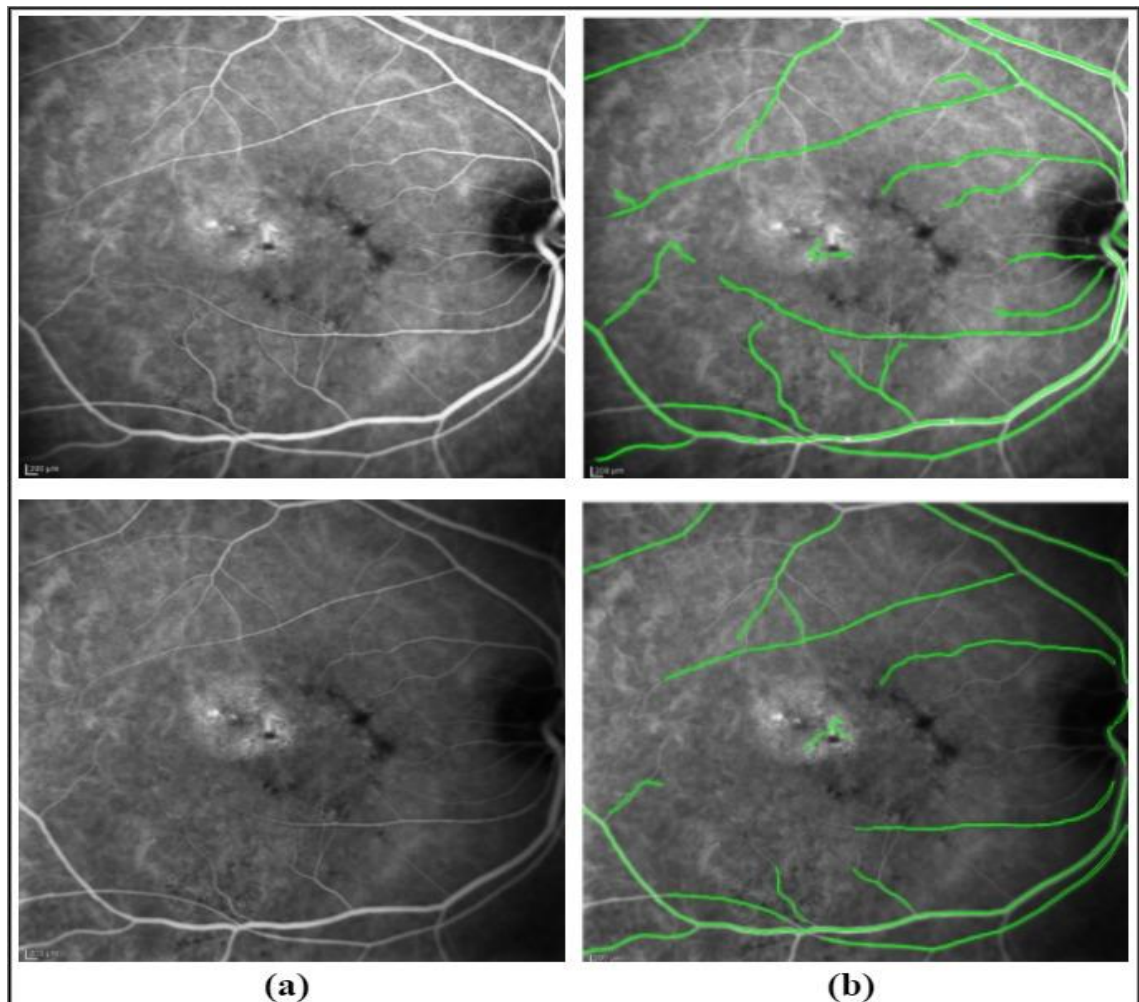


**Figure 6.1:** An initial evaluation of the proposed nerve segmentation algorithm using retinal ICG images: (a) Original retinal image and (b) Automatically traced retinal blood vessels.

## References

- Acharya, R., Ng, Y. K. E. and Suri, J. S. (2008) *Image modeling of the human eye*. Edited by G.Z.Y. Stephen T.C. Wong. Artech House.
- Alam, U., Asghar, O., Petropoulos, I. N., Jeziorska, M., Fadavi, H., Ponirakis, G., Marshall, A., Tavakoli, M., Boulton, A. J. M., Efron, N. and Malik, R. A. (2015) 'Small Fiber Neuropathy in Patients With Latent Autoimmune Diabetes in Adults: Table 1', *Diabetes Care*, 38(7), pp. e102–e103. doi: 10.2337/dc14-2354.
- Alzubaidi, R. S. M. (2017) *Fully automated computer system for diagnosis of corneal diseases Development of image processing technologies for the diagnosis of Acanthamoeba and Fusarium diseases in confocal microscopy images*, PhD Thesis, Univeristy of Bradford, Bradford, UK.
- Annunziata, R., Kheirhah, A., Aggarwal, S., Cavalcanti, B. M., Hamrah, P. and Trucco, E. (2014) 'Tortuosity Classification of Corneal Nerves Images Using a Multiple-Scale-Multiple-Window Approach', 44(0), pp. 113–120.
- Azmi, S., Ferdousi, M., Petropoulos, I. N., Ponirakis, G., Alam, U., Fadavi, H., Asghar, O., Marshall, A., Atkinson, A. J., Jones, W., Boulton, A. J. M., Tavakoli, M., Jeziorska, M. and Malik, R. A. (2015) 'Corneal Confocal Microscopy Identifies Small-Fiber Neuropathy in Subjects With Impaired Glucose Tolerance Who Develop Type 2 Diabetes', *Diabetes Care*, 38(8), pp. 1502–1508. doi: 10.2337/dc14-2733.
- Beucher, S. and Lantuejoul, C. (1979) 'Use of Watersheds in Contour Detection', *International Workshop on Image Processing: Real-time Edge and Motion Detection/Estimation*, (JANUARY 1979), pp. 12–21. doi: citeulike-article-id:4083187.
- Beucher, S. and Meyer, F. (1993) 'The Morphological Approach to Segmentation : The Watershed Transformation', in *Optical Engineering-New York-Marcel Dekker Incorporated- 34*, pp. 433–481.
- Bitirgen, G., Ozkagnici, A., Bozkurt, B. and Malik, R. A. (2015) 'In Vivo corneal confocal microscopic analysis in patients with keratoconus.', *International journal of ophthalmology*, 8(3), pp. 534–9. doi: 10.3980/j.issn.2222-3959.2015.03.17.
- Bitirgen, G., Ozkagnici, A., Malik, R. A. and Oltulu, R. (2013) 'Evaluation of contact lens-induced changes in keratoconic corneas using In Vivo confocal microscopy', *Investigative Ophthalmology and Visual Science*, 54(8), pp. 5385–5391. doi: 10.1167/iovs.13-12437.
- Boulton, A. J. M. (2005) 'Management of Diabetic Peripheral Neuropathy', *Clinical Diabetes*, 23(1), pp. 9–15. doi: 10.2337/diaclin.23.1.9.
- Brookes, N. H. (2017) 'Morphometry of organ cultured corneal endothelium using Voronoi segmentation', *Cell and Tissue Banking*. Springer Netherlands, 18(2), pp. 167–183. doi: 10.1007/s10561-017-9622-9.
- Canny, J. (1986) 'A Computational Approach to Edge Detection', *IEEE Transactions on Pattern Analysis and Machine Intelligence*, PAMI-8(6), pp. 679–698. doi: 10.1109/TPAMI.1986.4767851.
- De Carlo, T. E., Romano, A., Waheed, N. K. and Duker, J. S. (2015) 'A review of optical coherence tomography angiography (OCTA)', *International Journal of Retina and Vitreous*, 1(1), pp. 1–15. doi: 10.1186/s40942-015-0005-8.
- Chen, S., Chew, E. Y. and Chan, C.C. (2015) 'Pathology characteristics of ocular von Hippel-Lindau disease with neovascularization of the iris and cornea: a case report',

- Journal of Medical Case Reports*, 9(1), p. 66. doi: 10.1186/s13256-015-0539-2.
- Chen, X., Graham, J., Dabbah, M. A., Petropoulos, I. N., Ponirakis, G., Asghar, O., Alam, U., Marshall, A., Fadavi, H., Ferdousi, M. and others (2015a) 'Small Nerve Fiber Quantification in the Diagnosis of Diabetic Sensorimotor Polyneuropathy: Comparing Corneal Confocal Microscopy With Intraepidermal Nerve Fiber Density', *Diabetes Care*, (August). doi: 10.2337/dc14-2422.
- Chen, X., Graham, J., Dabbah, M. A., Petropoulos, I. N., Ponirakis, G., Asghar, O., Alam, U., Marshall, A., Fadavi, H., Ferdousi, M. and others (2015b) 'Small Nerve Fiber Quantification in the Diagnosis of Diabetic Sensorimotor Polyneuropathy: Comparing Corneal Confocal Microscopy With Intraepidermal Nerve Fiber Density', *Diabetes Care*, (January 2016). doi: 10.2337/dc14-2422.
- Choo, M., Prakash, K., Samsudin, A., Soong, T., Ramli, N. and Kadir, A. (2010) 'Corneal changes in type II diabetes mellitus in Malaysia.', *International journal of ophthalmology*, 3(3), pp. 234–6. doi: 10.3980/j.issn.2222-3959.2010.03.12.
- Dabbah, M.A., Graham, J., Petropoulos and I. M. Tavakoli, and Malik, R. A. (2010) 'Dual-Model Automatic Detection of Nerve-Fibres in Corneal Confocal Microscopy Images', in *Changes*, pp. 997–1003. doi: 10.1016/j.biotechadv.2011.08.021.Secreted.
- Dabbah, M.A., Graham, J., Tavakoli, M., Petropoulos, Y. and Malik, R. A. (2009) 'Nerve Fibre Extraction in Confocal Corneal Microscopy Images for Human Diabetic Neuropathy Detection using Gabor Filters', in *Medical Image Understanding and Analysis (MIUA)*.
- Dabbah, M.A., Graham, J., Petropoulos, I. N., Tavakoli, M. and Malik, R. A. (2011) 'Automatic analysis of diabetic peripheral neuropathy using multi-scale quantitative morphology of nerve fibres in corneal confocal microscopy imaging.', *Medical image analysis*. Elsevier B.V., 15(5), pp. 738–47. doi: 10.1016/j.media.2011.05.016.
- De, I., Chanda, B. and Chattopadhyay, B. (2006) 'Enhancing effective depth-of-field by image fusion using mathematical morphology', *Image and Vision Computing*, 24(12), pp. 1278–1287. doi: 10.1016/j.imavis.2006.04.005.
- Dehghani, C., Pritchard, N., Edwards, K., Vagenas, D., Russell, A. W., Malik, R. A. and Efron, N. (2014) 'Natural History of Corneal Nerve Morphology in Mild Neuropathy Associated With Type 1 Diabetes: Development of a Potential Measure of Diabetic Peripheral Neuropathy', *Investigative Ophthalmology & Visual Science*, 55(12), pp. 7982–7990. doi: 10.1167/iovs.14-15605.
- DiabetesUK (2012) 'Diabetes in the UK 2012: key statistics on diabetes.', *National Service Framework for Diabetes*, (April), pp. 1–22. doi: <http://www.diabetes.org.uk/Professionals/Publications-reports-and-resources/Reports-statistics-and-case-studies/Reports/Diabetes-prevalence-2010/>. [Accessed 2017].
- Doughty, M. J. and Aakre, B. M. (2008) 'Further analysis of assessments of the coefficient of variation of corneal endothelial cell areas from specular microscopic images', *Clinical and Experimental Optometry*, 91(5), pp. 438–446. doi: 10.1111/j.1444-0938.2008.00281.x.
- Dua, H. S., Faraj, L. A., Said, D. G., Gray, T. and Lowe, J. (2013) 'Human corneal anatomy redefined: A novel pre-descemet's layer (Dua's Layer)', *Ophthalmology*, 120(9), pp. 1778–1785. doi: 10.1016/j.ophtha.2013.01.018.

- Elbita, A., Qahwaji, R., Ipson, S., Sharif, M. S. and Ghanchi, F. (2014) 'Preparation of 2D sequences of corneal images for 3D model building', *Computer Methods and Programs in Biomedicine*. Elsevier Ireland Ltd, 114(2), pp. 194–205. doi: 10.1016/j.cmpb.2014.01.009.
- Fabijańska, A. (2017) 'Corneal Endothelium Image Segmentation Using Feedforward Neural Network', in *Proceedings of the Federated Conference on Computer Science and Information Systems*, pp. 629–637. doi: 10.15439/2017F54.
- Ferreira, A., Morgado, A. M. and Silva, J. S. (2010) 'Corneal nerves segmentation and morphometric parameters quantification for early detection of diabetic neuropathy', *IFMBE Proceedings*, 29, pp. 264–267. doi: 10.1007/978-3-642-13039-7\_66.
- Ferreira, A., Morgado, A. M. and Silva, J. S. (2012) 'A method for corneal nerves automatic segmentation and morphometric analysis.', *Computer methods and programs in biomedicine*. Elsevier Ireland Ltd, 107(1), pp. 53–60. doi: 10.1016/j.cmpb.2011.09.014.
- Foracchia, M. and Ruggeri, A. (2000) 'Cell contour detection in corneal endothelium in-vivo microscopy', *Proceedings of the 22nd Annual International Conference of the IEEE Engineering in Medicine and Biology Society*, 2, pp. 1033–1035. doi: 10.1109/IEMBS.2000.897902.
- Foracchia, M. and Ruggeri, A. (2007) 'Corneal endothelium cell field analysis by means of interacting bayesian shape models', *Annual International Conference of the IEEE Engineering in Medicine and Biology - Proceedings*, pp. 6035–6038. doi: 10.1109/IEMBS.2007.4353724.
- Frangakis, A. S. and Hegerl, R. (2001) 'Noise reduction in electron tomographic reconstructions using nonlinear anisotropic diffusion.', *Journal of structural biology*, 135(3), pp. 239–250. doi: 10.1006/jsbi.2001.4406.
- Fritz, L. (2006) 'Diffusion-based applications for interactive medical image segmentation', *Proceedings of CESC G (Central European Seminar on Computer Graphics)*.
- Gain, P., Thuret, G., Kodjikian, L., Gavet, Y., Turc, P. H., Theillere, C., Acquart, S., Le Petit, J. C., Maugery, J. and Campos, L. (2002) 'Automated tri-image analysis of stored corneal endothelium', *The British journal of ophthalmology*, 86(7), pp. 801–8. doi: 10.1136/bjo.86.7.801.
- Gomes, A. (2009) *Implicit Curves and Surfaces: Mathematics, Data Structures and Algorithms*. Springer-Verlag. doi: 10.1007/978-1-84882-406-5.
- Gonzalez, R. and Woods, R. (2002) *Digital image processing*, Pearson Prentice Hall. doi: 10.1016/0734-189X(90)90171-Q.
- Grisan, E., Paviotti, A., Laurenti, N. and Ruggeri, A. (2005) 'A lattice estimation approach for the automatic evaluation of corneal endothelium density', *Conference proceedings : Annual International Conference of the IEEE Engineering in Medicine and Biology Society. IEEE Engineering in Medicine and Biology Society. Annual Conference*, 2(1), pp. 1700–3. doi: 10.1109/IEMBS.2005.1616771.
- Guimar, P., Wigdahl, J., Poletti, E. and Ruggeri, A. (2014) 'A fully-automatic fast segmentation of the sub-basal layer nerves in corneal images \*', pp. 5422–5425.
- Habrat, K., Habrat, M., Gronkow-Skaserafin, J. and Piórkowski, A. (2015) 'Cell detection in corneal endothelial images using directional filters', *Advances in Intelligent Systems and Computing*, 389, pp. 113–123. doi: 10.1007/978-3-319-23814-2\_14.



- Haddad, R. A. and Akansu, A. N. (1991) 'A class of fast Gaussian binomial filters for speech and image processing', *IEEE Transactions on Signal Processing*, 39(3), pp. 723–727. doi: 10.1109/78.80892.
- Haque, M. N. and Uddin, M. S. (2011) 'Accelerating Fast Fourier Transformation for Image Processing using Graphics Processing Unit', *Journal of Emerging Trends in Computing and*, 2(8), pp. 367–375. Available at: <http://www.doaj.org/doaj?func=abstract&id=868197>.
- Hatipoglu, E., Arici, C., Arslan, O. S., Dikkaya, F., Sultan, P., Kadioglu, P. and Gundogdu, S. (2014) 'Corneal endothelial cell density and morphology in patients with acromegaly', *Growth Horm IGF Res*, 24(6), pp. 260–263. doi: 10.1016/j.ghir.2014.08.003.
- Hill, R. M., A. J. L. (1965) 'Temperature Changes of a Human Cornea and Tears Under a Contact Lens: 1. The Relaxed Open Eye, and the Natural and Forced Closed Eye Conditions', *Am. J. Optometry Arch. Am. Acad. Optometry*, 42, pp. 9–16.
- Hiroyasu, T., Sekiya, S., Nunokawa, S., Koizumi, N., Okumura, N. and Yamamoto, U. (2013) 'Extracting rules for cell segmentation in corneal endothelial cell images using GP', *Proceedings - 2013 IEEE International Conference on Systems, Man, and Cybernetics, SMC 2013*, pp. 1811–1816. doi: 10.1109/SMC.2013.305.
- Ito, K., Aoki, T., Kosuge, E., Kawamata, R. and Kashima, I. (2008) 'Medical image registration using Phase-Only Correlation for distorted dental radiographs', *2008 19th International Conference on Pattern Recognition*, (1), pp. 0–3. doi: 10.1109/ICPR.2008.4761734.
- J.W. Cooley and J.W. Tukey (1965) 'An algorithm for the machine calculation of complex Fourier Series', *Mathematics of computation*, 19(90), p. pp 297-301.
- Jabbur, N. S., Chicani, C. F., Kuo, I. C. and O'Brien, T. P. (2004) 'Risk factors in interface epithelialization after laser in situ keratomileusis.', *Journal of refractive surgery (Thorofare, N.J. : 1995)*, 20(4), pp. 343–348.
- Jalbert, I., Stapleton, F., Papas, E., Sweeney, D. F. and Coroneo, M. (2003a) 'In Vivo confocal microscopy of the human cornea'. *British Journal of Ophthalmology*, 87(2), 225-236.
- Jalbert, I., Stapleton, F., Papas, E., Sweeney, D. F. and Coroneo, M. (2003b) 'In Vivo confocal microscopy of the human cornea.', *British Journal of Ophthalmology*, 87(2), pp. 225–236. doi: 10.1136/bjo.87.2.225.
- Katafuchi, S. and Yoshimura, M. (2017) 'Convolution neural network for contour extraction of corneal endothelial cells', *Katafuchi, S., & Yoshimura, M. (2017). Convolution neural network for contour extraction of corneal endothelial cells. In Thirteenth International Conference on Quality Control by Artificial Vision 2017*, 10338, p. 103380L. doi: 10.1117/12.2264430.
- Kaur, J., Agrawal, S. and Vig, R. (2012) 'Integration of Clustering, Optimization and Partial Differential Equation Method for Improved Image Segmentation', *International Journal of Image, Graphics and Signal Processing*, 4(11), pp. 26–33. doi: 10.5815/ijigsp.2012.11.04.
- Khan, A., Akhtar, N., Kamran, S., Ponirakis, G., Petropoulos, I. N., Tunio, N. A., Dargham, S. R., Imam, Y., Sartaj, F., Parray, A., Bourke, P., Khan, R., Santos, M., Joseph, S., Shuaib, A. and Malik, R. A. (2017) 'Corneal Confocal Microscopy Detects Corneal Nerve Damage in Patients Admitted With Acute Ischemic Stroke', *Stroke*, 48(11), pp. 3012–3018. doi: 10.1161/STROKEAHA.117.018289.

- Kim, Y.Y., Kim, B.M., Park, H.J., Im, K.B., Lee, J.S. and Kim, D.Y. (2006) 'Image Analysis Algorithm for the Corneal Endothelium', *Journal of Biomedical Engineering Research*, 27(3), pp. 125–130.
- Kroon, D., Slump, C. H. and Maal, T. J. J. (2010) 'Optimized Anisotropic Rotational Invariant Diffusion Scheme on Cone-beam CT', in *In International Conference on Medical Image Computing and Computer-Assisted Intervention*. Springer Berlin Heidelberg, pp. 221–228.
- Kruse A., Thomsen R. W., Hundborg H. H., Knudsen L. L., Sørensen H. T., Schønheyder H. C. (2006) 'Diabetes and risk of acute infectious conjunctivitis — a population-based case-control study', pp. 393–397. doi: 10.1111/j.1464-5491.2005.01812.x.
- Kurbanyan, K., Hoesl, L. M., Schrems, W. A. and Hamrah, P. (2012) 'Corneal nerve alterations in acute Acanthamoeba and fungal keratitis: an In Vivo confocal microscopy study.', *Eye (London, England)*. Nature Publishing Group, 26(1), pp. 126–32. doi: 10.1038/eye.2011.270.
- Lee, B. L., Holland, G. N. and Glasgow, B. J. (1996) 'Chiasmal infarction and sudden blindness caused by mucormycosis in AIDS and diabetes mellitus.', *American journal of ophthalmology*. Elsevier Inc., 122(6), pp. 895–896. doi: 10.1016/S0002-9394(14)70392-7.
- Lovblom, L. E., Halpern, E. M., Wu, T., Kelly, D., Ahmed, A., Boulet, G., Orszag, A., Ng, E., Ngo, M., Bril, V. and Perkins, B. A. (2015) 'In Vivo Corneal Confocal Microscopy and Prediction of Future-Incident Neuropathy in Type 1 Diabetes: A Preliminary Longitudinal Analysis.', *Canadian journal of diabetes*, 39, pp. 390–397. doi: 10.1016/j.jcjd.2015.02.006.
- Madhuri, S. G. (2014) 'Classification of Image Registration Techniques and Algorithms in Digital Image Processing – A Research Survey', *International Journal of Computer Trends and Technology (IJCTT)*, 15(2), pp. 78–82.
- Malik, R. A., Kallinikos, P., Abbott, C. A., Van Schie, C. H. M., Morgan, P., Efron, N. and Boulton, A. J. M. (2003) 'Corneal confocal microscopy: a non-invasive surrogate of nerve fibre damage and repair in diabetic patients.', *Diabetologia*, 46(5), pp. 683–688. doi: 10.1007/s00125-003-1086-8.
- Mallikarjuna, K., Satya Prasad, K. and Venkata Subramanyam, M. (2016) 'Image Compression and Reconstruction using Discrete Rajan Transform Based Spectral Sparsing', *International Journal of Image, Graphics and Signal Processing*, 8(1), pp. 59–67. doi: 10.5815/ijigsp.2016.01.07.
- Mapstone, R. (1968) 'DETERMINANTS OF CORNEAL TEMPERATURE', *Brit. J. Ophthal*, 52, pp. 729–741.
- Mapstone, R. (1970) 'Ocular thermography.', *The British journal of ophthalmology*, 54(11), pp. 751–754. doi: 10.1136/bjo.54.11.751.
- Martin, D., Fowlkes, C., Tal, D. and Malik, J. (2001) 'A database of human segmented natural images and its application to evaluating segmentation algorithms and measuring ecological statistics', *Proceedings Eighth IEEE International Conference on Computer Vision. ICCV 2001*, 2(July). doi: 10.1109/ICCV.2001.937655.
- McCarey, B. E., Edelhauser, H. F. and Lynn, and M. J. (2008) 'Review of Corneal Endothelial Specular Microscopy for FDA Clinical Trials of Refractive Procedures, Surgical Devices and New Intraocular Drugs and Solutions', *Cornea*, 27(1), pp. 1–16. doi: 10.1097/ICO.0b013e31815892da.Review.
- Meilă, M. (2007) 'Comparing Clusterings – An Information Based Distance', *Journal of*

- multivariate analysis*, 98(5), pp. 873–895.
- Mendrik, A.M., Vonken, E.J., Rutten, A., Viergever, M. A. and Van Ginneken, B. (2009) 'Noise reduction in computed tomography scans using 3-d anisotropic hybrid diffusion with continuous switch.', *IEEE transactions on medical imaging*, 28(10), pp. 1585–94. doi: 10.1109/TMI.2009.2022368.
- Meyer, F. (2012) 'The watershed concept and its use in segmentation : a brief history', pp. 1–11. Available at: <http://arxiv.org/abs/1202.0216>.
- Moilanen, J.A.O. (2003) 'Long-Term Corneal Morphology after PRK by In Vivo Confocal Microscopy', *Investigative Ophthalmology & Visual Science*, 44(3), pp. 1064–1069. doi: 10.1167/iovs.02-0247.
- Moilanen, J.A.O., Vesaluoma, M.H., Müller, L.J. and Tervo, T.M.T. (2003) 'Long-term corneal morphology after PRK by In Vivo confocal microscopy', *Investigative Ophthalmology and Visual Science*, 44(3), pp. 1064–1069. doi: 10.1167/iovs.02-0247.
- Najafi, L., Malek, M., Valojerdi, A. E., Aghili, R., Khamseh, M. E., Fallah, A. E., Tokhmehchi, M.R.F. and Behrouz, M.J. (2013) 'Dry eye and its correlation to diabetes microvascular complications in people with type 2 diabetes mellitus', *Journal of Diabetes and its Complications*, 27(5), pp. 459–462. doi: 10.1016/j.jdiacomp.2013.04.006.
- Navaratnam, J., Utheim, T.P., Rajasekhar, V.K. and Shahdadfar, A. (2015) 'Substrates for Expansion of Corneal Endothelial Cells towards Bioengineering of Human Corneal Endothelium.', *Journal of functional biomaterials*, 6(3), pp. 917–45. doi: 10.3390/jfb6030917.
- Negi, A. and Vernon, S.A. (2003) 'An overview of the eye in diabetes.', *Journal of the Royal Society of Medicine*, 96(6), pp. 266–272. doi: 10.1258/jrsm.96.6.266.
- Niederer, R. L., Perumal, D., Sherwin, T. and McGhee, C. N. J. (2007) 'Corneal innervation and cellular changes after corneal transplantation: an In Vivo confocal microscopy study.', *Investigative ophthalmology & visual science*, 48(2), pp. 621–6. doi: 10.1167/iovs.06-0538.
- Nishida, T. (2005) 'Neurotrophic Mediators and Corneal Wound Healing', *The Ocular Surface*. Elsevier Inc., 3(4), pp. 194–202. doi: 10.1016/S1542-0124(12)70206-9.
- O'Donnell, C. and Efron, N. (2012) 'Diabetes and contact lens wear.', *Clinical & experimental optometry : journal of the Australian Optometrical Association*, 95(3), pp. 328–37. doi: 10.1111/j.1444-0938.2012.00738.x.
- Oliveira, F.P.M. and Tavares, J.M.R.S. (2014) 'Medical image registration: a review', *Computer Methods in Biomechanics and Biomedical Engineering*. Taylor & Francis, pp. 73–93. doi: 10.1080/10255842.2012.670855.
- Otel, I. (2012) 'Evaluation of corneal nerve morphology for detection and follow-up of Diabetic Peripheral Neuropathy', Master Thesis, Faculdade De Ciências E Tecnologia, Universidade De Coimbra.
- Otel, I., Cardoso, P., Gomes, L., Gouveia, S., Silva, S. F., Domingues, J. P., Silva, J. S., Carvalheiro, M., Quadrado, M. J. and Morgado, A. M. (2013) 'Diabetic Peripheral Neuropathy Assessment Through Corneal Nerve Morphometry', (February), pp. 1–6.
- Pacaud, D., Romanchuk, K. G., Tavakoli, M., Gougeon, C., Virtanen, H., Ferdousi, M., Nettel-Aguirre, A., Mah, J. K. and Malik, R. A. (2015) 'The Reliability and Reproducibility of Corneal Confocal Microscopy in Children', *Investigative*

- Ophthalmology & Visual Science*, 56(9), p. 5636. doi: 10.1167/iovs.15-16995.
- Patel, D. V and McGhee, C. N. J. (2006) 'Mapping the corneal sub-basal nerve plexus in keratoconus by In Vivo laser scanning confocal microscopy.', *Investigative ophthalmology & visual science*, 47(4), pp. 1348–51. doi: 10.1167/iovs.05-1217.
- Patel, S. V, McLaren, J. W., Hodge, D. O. and Bourne, W. M. (2002) 'Confocal Microscopy In Vivo in Corneas of Long-Term Contact Lens Wearers', 43(4), pp. 995–1003.
- Petropoulos, I. N., Alam, U., Fadavi, H., Marshall, A., Asghar, O., Dabbah, M. A., Chen, X., Graham, J., Ponirakis, G., Boulton, A. J. M., Tavakoli, M. and Malik, R. A. (2014) 'Rapid Automated Diagnosis of Diabetic Peripheral Neuropathy With In Vivo Corneal Confocal Microscopy', *Investigative Ophthalmology & Visual Science*, 55(4), p. 2071. doi: 10.1167/iovs.13-13787.
- Petropoulos, I. N., Manzoor, T., Morgan, P., Fadavi, H., Asghar, O., Alam, U., Ponirakis, G., Dabbah, M. A., Chen, X., Graham, J., Tavakoli, M. and Malik, R. A. (2013) 'Repeatability of In Vivo corneal confocal microscopy to quantify corneal nerve morphology.', *Cornea*, 32(5), pp. e83-9. doi: 10.1097/ICO.0b013e3182749419.
- Piorkowski, A., Nurzynska, K., Gronkowska-Serafin, J., Selig, B., Boldak, C. and Reska, D. (2017) 'Influence of applied corneal endothelium image segmentation techniques on the clinical parameters', *Computerized Medical Imaging and Graphics*. Elsevier Ltd, 55, pp. 13–27. doi: 10.1016/j.compmedimag.2016.07.010.
- Poletti, E. and Ruggeri, A. (2013) 'Automatic nerve tracking in confocal images of corneal subbasal epithelium', *Proceedings of the 26th IEEE International Symposium on Computer-Based Medical Systems*. Ieee, pp. 119–124. doi: 10.1109/CBMS.2013.6627775.
- Poletti, E. and Ruggeri, A. (2014) 'Segmentation of Corneal Endothelial Cells Contour through Classification of Individual Component Signatures', *IFMBE Proceedings*, 41, pp. 658–661. doi: 10.1007/978-3-319-00846-2.
- Pritchard, N., Edwards, K., Russell, A. W., Perkins, B. A., Malik, R. A. and Efron, N. (2015) 'Corneal confocal microscopy predicts 4-year incident peripheral neuropathy in type 1 diabetes.', *Diabetes care*, 38(4), pp. 671–5. doi: 10.2337/dc14-2114.
- Pritchard, N., Edwards, K., Shahidi, A. M., Sampson, G. P., Russell, A. W., Malik, R. A. and Efron, N. (2011) 'Corneal markers of diabetic neuropathy.', *The ocular surface*. Elsevier Inc., 9(1), pp. 17–28. doi: 10.1016/S1542-0124(11)70006-4.
- Quattrini, C., Tavakoli, M., Jeziorska, M., Kallinikos, P., Tesfaye, S., Finnigan, J., Marshall, A., Boulton, A. J. M., Efron, N. and Malik, R. A. (2007) 'Surrogate Markers of Small Fiber Damage in Human Diabetic Neuropathy', *Diabetes*, 56(8), pp. 2148–2154. doi: 10.2337/db07-0285.
- Reem, D. (2011) 'The geometric stability of Voronoi diagrams with respect to small changes of the sites', in *In Proceedings of the twenty-seventh annual symposium on Computational geometry, ACM*, pp. 254–263. doi: 10.1145/1998196.1998234.
- Reinhard, T. and Larkin, F. (2013) *Corneal Disease: Recent Developments in Diagnosis and Therapy*, *British medical journal*. In Springer-Verlag Berlin Heidelberg. doi: 10.1136/bmj.2.5710.669.
- Ruggeri, A., Grisan, E. and Jaroszewski, J. (2005) 'A new system for the automatic estimation of endothelial cell density in donor corneas', *The British journal of ophthalmology*, 89(3), pp. 306–11. doi: 10.1136/bjo.2004.051722.

- Ruggeri, A., Scarpa, F. and Grisan, E. (2006) 'Analysis of corneal images for the recognition of nerve structures', *Annual International Conference of the IEEE Engineering in Medicine and Biology - Proceedings*, pp. 4739–4742. doi: 10.1109/IEMBS.2006.259805.
- Scarpa, F., Fiorin, D. and Ruggeri, A. (2007) 'In Vivo three-dimensional reconstruction of the cornea from confocal microscopy images', *Annual International Conference of the IEEE Engineering in Medicine and Biology - Proceedings*, pp. 747–750. doi: 10.1109/IEMBS.2007.4352398.
- Scarpa, F., Grisan, E. and Ruggeri, A. (2008a) 'Automatic recognition of corneal nerve structures in images from confocal microscopy.', *Investigative ophthalmology & visual science*, 49(11), pp. 4801–7. doi: 10.1167/iovs.08-2061.
- Scarpa, F., Grisan, E. and Ruggeri, A. (2008b) 'Automatic recognition of corneal nerve structures in images from confocal microscopy.', *Investigative ophthalmology & visual science*, 49(11), pp. 4801–7. doi: 10.1167/iovs.08-2061.
- Scarpa, F. and Ruggeri, A. (2015) 'Segmentation of Corneal Endothelial Cells Contour by Means of a Genetic Algorithm', in *Proceedings of the Ophthalmic Medical Image Analysis Second International Workshop, OMIA 2015, Held in Conjunction with MICCAI 2015, Munich, Germany*, pp. 25–32.
- Scarpa, F., Zheng, X., Ohashi, Y. and Ruggeri, A. (2011) 'Automatic evaluation of corneal nerve tortuosity in images from In Vivo confocal microscopy.', *Investigative ophthalmology & visual science*, 52(9), pp. 6404–8. doi: 10.1167/iovs.11-7529.
- Selig, B., Vermeer, K. A., Rieger, B., Hillenaar, T. and Luengo Hendriks, C. L. (2015) 'Fully automatic evaluation of the corneal endothelium from In Vivo confocal microscopy.', *BMC medical imaging*, 15(1), p. 13. doi: 10.1186/s12880-015-0054-3.
- Sharif, M. S., Qahwaji, R., Hayajneh, S., Ipson, S., Alzubaidi, R. and Brahma, A. (2014) 'An efficient system for preprocessing confocal corneal images for subsequent analysis', *2014 14th UK Workshop on Computational Intelligence, UKCI 2014 - Proceedings*. doi: 10.1109/UKCI.2014.6930188.
- Sharif, M. S., Qahwaji, R., Shahamatnia, E., Alzubaidi, R., Ipson, S. and Brahma, A. (2015) 'An efficient intelligent analysis system for confocal corneal endothelium images', *Computer Methods and Programs in Biomedicine*. Elsevier Ireland Ltd, 122(3), pp. 421–436. doi: 10.1016/j.cmpb.2015.09.003.
- Simo Mannion, L., Tromans, C. and O'Donnell, C. (2005) 'An evaluation of corneal nerve morphology and function in moderate keratoconus.', *Contact lens & anterior eye: the journal of the British Contact Lens Association*, 28(4), pp. 185–92. doi: 10.1016/j.clae.2005.10.005.
- Skarbez, K., Priestley, Y., Hoepf, M. and Koevary, S. (2010) 'Comprehensive review of the effects of diabetes on ocular health', *Expert Rev Ophthalmology*, 5(4), pp. 557–577. doi: 10.1586/eop.10.44.Comprehensive.
- Smith, S. W. (1999) *Digital signal processing*, California Technical Publishing. doi: 10.1109/79.826412.
- Srinivasa Reddy, B. and Chatterji, B. N. (1996) 'An FFT-based technique for translation, rotation, and scale-invariant image registration', *IEEE Transactions on Image Processing*, 5(8), pp. 1266–1271. doi: 10.1109/83.506761.
- Tang, M. and Chen, F. (2012) 'A qualitative meta analysis review on medical image registration evaluation', *Procedia Engineering*, 29, pp. 499–503. doi: 10.1016/j.proeng.2011.12.750.

- Tavakoli, M. and Malik, R. A. (2011) 'Corneal Confocal Microscopy: A Novel Non-invasive Technique to Quantify Small Fibre Pathology in Peripheral Neuropathies', *Journal of Visualized Experiments*, (47), pp. 1–7. doi: 10.3791/2194.
- Tavakoli, M., Mitu-Pretorian, M., Petropoulos, I. N., Fadavi, H., Asghar, O., Alam, U., Ponirakis, G., Jeziorska, M., Marshall, A., Efron, N., Boulton, A. J., Augustine, T. and Malik, R. A. (2013) 'Corneal Confocal Microscopy Detects Early Nerve Regeneration in Diabetic Neuropathy After Simultaneous Pancreas and Kidney Transplantation', *Diabetes*, 62(1), pp. 254–260. doi: 10.2337/db12-0574.
- Tervo, T. and Moilanen, J. (2003) 'In Vivo confocal microscopy for evaluation of wound healing following corneal refractive surgery', *Progress in Retinal and Eye Research*, 22(3), pp. 339–358. doi: 10.1016/S1350-9462(02)00064-2.
- Vincent, L. M. (1992) 'Morphological image processing and network analysis of cornea endothelial cell images', *Proceedings of SPIE*, 1769(July), pp. 212–226. doi: 10.1117/12.60644.
- Wang, Z., Bovik, A. C., Sheikh, H. R., Member, S., Simoncelli, E. P. and Member, S. (2004) 'Image Quality Assessment: From Error Visibility to Structural Similarity', *IEEE TRANSACTIONS ON IMAGE PROCESSING*, 13(4), pp. 1–14.
- Weickert, J. (1998) 'Anisotropic diffusion in image processing', *Image Rochester NY*, 256(3), p. 170. doi: 10.1.1.11.751.
- Weickert, J. and Schar, H. (2002) 'A Scheme for Coherence-Enhancing Diffusion Filtering with Optimized Rotation Invariance', *Journal of Visual Communication and Image Representation*, 13(1–2), pp. 103–118. doi: 10.1006/jvci.2001.0495.
- Xue, W., Zhang, L., Mou, X. and Bovik, A. C. (2014) 'Gradient magnitude similarity deviation: A highly efficient perceptual image quality index', *IEEE Transactions on Image Processing*, 23(2), pp. 668–695. doi: 10.1109/TIP.2013.2293423.
- Yan, H. and Liu, J. G. (2008) 'Robust Phase Correlation Based Feature Matching for Image Co-Registration and DEM Generation', *The International Archives of the Photogrammetry, Remote Sensing and Spatial Information Sciences*, XXXVII(B7), pp. 1751–1756.
- You, Y., Xu, W., Tannenbaum, A. and Kaveh, M. (1996) *Behavioral Analysis of Anisotropic Diffusion in Image Processing*. *IEEE Transactions on Image Processing*, 5(11), 1539-1553.
- Zheng, T., Le, Q., Hong, J. and Xu, J. (2016) 'Comparison of human corneal cell density by age and corneal location: an In Vivo confocal microscopy study', *BMC Ophthalmology*. *BMC Ophthalmology*, 16(1), p. 109. doi: 10.1186/s12886-016-0290-5.
- Zitová, B. and Flusser, J. (2003) 'Image registration methods: A survey', *Image and Vision Computing*, 21(11), pp. 977–1000. doi: 10.1016/S0262-8856(03)00137-9.
- Zysk, A. M., Nguyen, F. T., Oldenburg, A. L., Marks, D. L. and Boppart, S. a (2007) 'Optical coherence tomography: a review of clinical development from bench to bedside.', *Journal of biomedical optics*, 12(5), p. 51403. doi: 10.1117/1.2793736.

---

# Appendices

## Appendix A: Canny Edge Detection

The motivation behind the optimization of the Canny edge detector was to achieve the following desirable properties: minimizing the probability of multiple responses to a single edge; minimizing the probability of missed edge; minimizing the distance between the detected edge pixels and the actual edge (Canny, 1986). All these criteria play a significant role in addressing the issues of detecting and localizing the corneal nerves correctly.

### Canny Algorithm:

- a) **Smooth Image:** Apply a Gaussian filter to the image to reduce noise and smooth image.
- b) **Compute Gradient:** Calculate the gradient magnitude and direction at each pixel of the smoothed image.
- c) **Non-Maxima Suppression:** non-maximum suppression algorithm is applied to gradient magnitude image.
- d) **Double Thresholding:** To detect and link an edge pixel using a hysteresis threshold algorithm.

More details of these are as follows.

- a) **Smooth Image:** Let  $G(x, y)$  denotes the Gaussian filter as shown in Eq.A.1 (Haddad and Akansu, 1991) and  $I(x, y)$  denotes the image. The convolution result of  $I(x, y)$  with  $G(x, y)$  will give a smoothed image as follows (Gomes, 2009):

$$S(x, y) = G(x, y) \otimes I(x, y) \quad (\text{A.1})$$

**b) Compute Gradient:** Firstly, the gradient of the smoothed image  $S(x, y)$  will be used to find  $x$  and  $y$  partial derivatives  $G_x$  and  $G_y$  respectively as follows:

$$G_x(x, y) \approx [S(x, y + 1) - S(x, y) + S(x + 1, y + 1) - S(x + 1, y)]/2 \quad (\text{A.2})$$

$$G_y(x, y) \approx [S(x, y) - S(x + 1, y) + S(x, y + 1) - S(x + 1, y + 1)]/2 \quad (\text{A.3})$$

From these two standard formulas, the gradient magnitude and direction can be calculated respectively as follows:

$$G(x, y) = \sqrt{G_x^2(x, y) + G_y^2(x, y)} \quad (\text{A.4})$$

$$\theta(x, y) = \tan^{-1} \left( \frac{G_y(x, y)}{G_x(x, y)} \right) \quad (\text{A.5})$$

**c) Non-Maxima Suppression:** The resulting from the gradient normally contain wide ridges around the local maximum and to thin these ridges a non-maxima suppression procedure is used to find thin edges which correspond to the positions of local maxima. For each pixel  $(x, y)$  define four discrete directions  $d_i$  (gradient vector) of the normal edge; horizontal, vertical,  $45^\circ$  and  $-45^\circ$ . From These 4 directions find the closest direction to  $\theta(x, y)$ . If the value of  $G(x, y)$  is lower of its two neighbors values along the direction  $d_i$ , let non-maxima suppressed  $N(x, y) = 0$  (suppression); else, let  $N(x, y) = G(x, y)$ .

**d) Double Thresholding (Hysteresis Thresholding):** It may be noticed that thresholding the image still produces false edge points and to reduce the



number of these the hysteresis method uses both low and high thresholds  $T_L$  and  $T_H$ . It determines non-maxima suppressed  $N_H(x, y)$  after thresholding  $N(x, y)$  with high threshold  $T_H$  and determine non-maxima suppressed  $N_L(x, y)$  after thresholding  $N(x, y)$  with low threshold  $T_L$ . It is clear that  $N_H$  includes the strong edge pixels and  $N_L$  includes weaker edge pixels. Sometimes the edges in  $N_H(x, y)$  have gaps, which are filled in using the lower threshold.

## Appendix B: Cornea Sub-Basal Epithelium System-GUI

When the Epithelium panel is activated/selected there are several options that can be chosen:

- 1. Open Original image button:** When you click the button, a file chooser will appear and you will be able to select stack of images. Once you select the images a panel on the right will display the selected images (shown in Figure B.1).
- 2. Run Analysis button:** When the button is clicked another file chooser appears and the user have to select the appropriate images to be diagnosed. A panel with original and processed images will appear. In order to scroll through the images, slider, popup menu and a Go button are available as shown in Figure B.1. This function asks the user about the type of the microscope used to acquire the original images; it gives the user the choice between ConfoScan 4 and Heidelberg microscopes.
- 3. Clinical Parameters:** After running the analysis on the selected epithelium mage/images, the extract clinical parameters about the detected nerve will

---

automatically appear. These parameters include the following as shown in Figure B.1:

- Nerve Number.
- Nerve tortuosity.
- Nerve Thickness.
- Nerve Length.
- Nerve Density.

In addition, a new figure will show up to display the colour image map with all detected sub-basal nerves are numbered, as shown in Figure B.2.

- 4. Movement Slider:** By clicking on the arrows of the slider, it will display the next image from the group of the epithelium images.
- 5. Popup menu:** The popup menu will also change the image but this time the user will be able to select the image using the image name.
- 6. Go button:** If you insert a number in the edit box and press the button, it will display the image according to that inserted value.

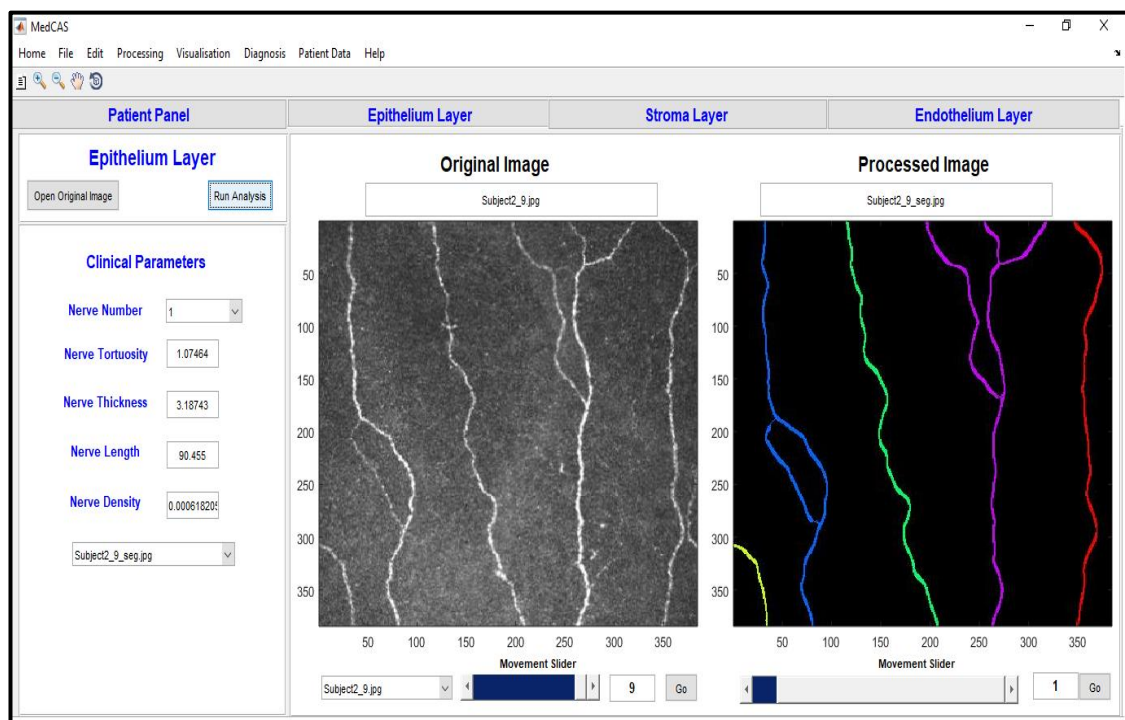


**Figure B.1:** The main interface of cornea sub-basal epithelium analysis.

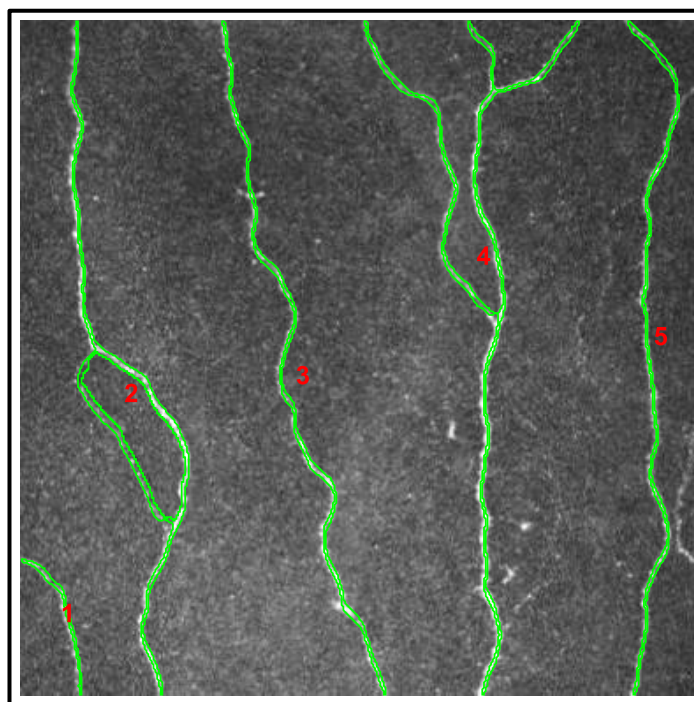


**Figure B.2:** Nerve number on color map image.

## Appendix C: Cornea Endothelium Analysis System (CEAS)-GUI

The proposed CEAS system consists of 3 panels for diagnosis and visualization purposes:

- Clinical Features Panel.
- Image Visualization Panel.
- Pleomorphism Map Panel.

The main Steps to load an image and calculate the clinical features:

1. Every time the user launches the software, he/she needs to press on the **Starting Software button** in order to connect the Matlab with the imageJ software. After that, the window of the imageJ software will show up, as shown in Figure C.1. The user can close it (for more convenience) and start working with the software. (This is only for the first time you are launching the software).



**Figure C.1:** The main interface of ImageJ software.

2. To open an endothelium image press on the **Load Endothelium Image button**, after selecting an image the Image Visualization panel will show up. It contains two figures, one for the selected image (input image) and the other one is its segmented image that will be used to calculate the clinical features, as shown in Figure C.2.

3. These clinical features include:
- Number of Cells in the selected ROI.
  - Cell Density.
  - Cell Pleomorphism.
  - Cell Polymegethism.
  - Cell Average Area.
  - Cell Average Perimeter.

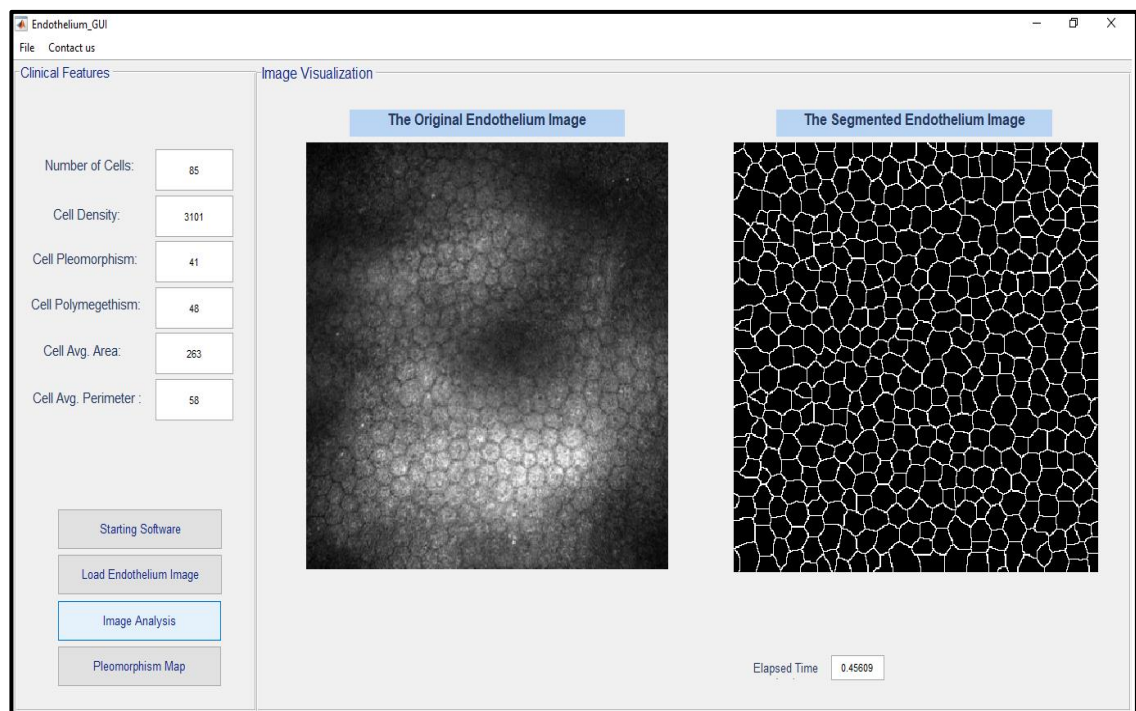


**Figure C.2:** The main interface of CEAS system.

4. In this software, the user can choose where to calculate these features from the segmented image. By clicking on the **Image Analysis button**, a dialog box will ask the user to enter the number of Regions of Interest (ROIs) that he/she wants to analyse. For example, if the user enters No. 3

this means he/she will be able to crop three different ROIs within the segmented image. (Better results could be obtained by selecting from the best segmented part of the input image).

5. Every time the users crop a new ROI, the clinical features of this ROI will be calculated automatically and shown in the Clinical Features panel. In addition, the software will create a new folder entitled (Results\_Of\_ + image's Name) in order to save all the selected ROIs and their clinical features as a text file (.txt).
6. In order to visualize the Pleomorphism map of all the selected ROIs, press on the **Pleomorphism Map button**. A new panel named Pleomorphism Map will show up containing a drop-list showing the names of the selected ROIs. The user can choose to display the Pleomorphism map for the selected ROI. This map will show the number of neighbours; whiter cells have a higher number of neighbours, while the darker cells have less number of neighbours (shown on Figure C.3).
7. The user can do the same operations (2-5) from the File menu.

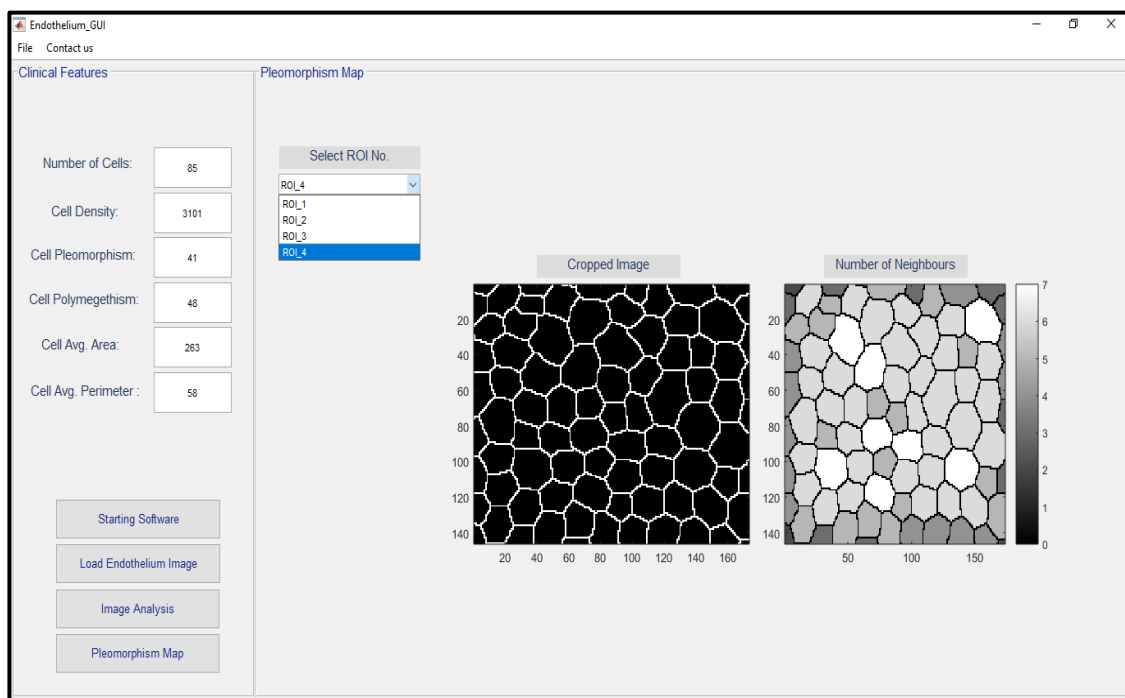


**Figure C.3:** The Pleomorphism map window.